Production, Scaling and Application of Nanostructured Metal Multilayers as Post-Weld Treatment

Vom Promotionsausschuss der
Technischen Universität Hamburg

zur Erlangung des akademischen Grades

Doktor-Ingenieur (Dr.-Ing.)

genehmigte Dissertation

von
Jakob Brunow

aus
Hamburg

2023

Gutachter:
Prof. Dr.-Ing. habil. Marcus Rutner
Prof. DSc. (Tech.) Sören Ehlers

Tag der Prüfung:
01.09.2023

DOI: https://doi.org/10.15480/882.8567

ORCID: https://orcid.org/0000-0002-1160-2344

Abstract

english

Cu/Ni Nanostructured Metal Multilayer coatings are introduced as a new post-weld treatment method.

Steel specimen with a double V-groove butt-weld are coated with a Cu/Ni NMM coating with an overall thickness of 9 μm, consisting of a 1 μm Ni base layer, a nanolaminate structure with a bilayer thickness of 50 nm and Cu and Ni single layer thicknesses of 15 nm and 35 nm respectively. The coating is electroplated onto the steel substrate with a single bath method.

The coated steel specimens are tested in tension-tension fatigue and the corresponding S-N curves are calculated from the fatigue results.

SEM, TEM and EDX investigations provide insights into the material characterization of the nanolaminate structure and the understanding of NMM failure mechanisms.

Abstract

deutsch

Cu/Ni Nanostrukturierte Metall Multilayer werden als neue Schweißnahtnachbehandlungsmethode vorgestellt.

Stahlproben mit einer geschweißten Doppel-V-Stumpfnaht werden mit Cu/Ni 9 μm dicken NMM beschichtet, die aus einer 1 μm Ni Grundbeschichtung, einer Doppelschichtdicke von 50 nm und Cu/Ni Einzelschichtdicken von 15 nm und 35 nm bestehen. Die Beschichtung wird galvanisch mit einem Einzelbadverfahren auf die Stahlgrundlage aufgebracht.

Die beschichteten Stahlproben werden im Zugschwellbereich auf Ermüdung getestet und die dazugehörigen Wöhlerkurven werden aus den Ermüdungsergebnissen berechnet.

REM, TEM und EDX Untersuchungen geben Einblicke in die Materialcharakterisierung der Nanolaminatstrukturen und dem Verständnis von NMM Versagensmechanismen.

Contents

List of Figures

List of Tables

List of Acronyms

AFM Atomic Force Microscopy

ARB Accumulative Roll Bonding

C4T Calls for Transfer

CLS Confined Layer Slip

CVD Chemical Vapor Deposition

DASt Deutscher Ausschuss für Stahlbau

ECCI Electron Channelling Contrast Imaging

EDX Energy-dispersive X-ray Spectroscopy

FEM Finite Element Method

FIB Focused Ion Beam

HAADF High-Angle Annular Dark Field

HAZ Heat Affected Zone

HFMI High Frequency Mechanical Impact

HiFIT High Frequency Impact Treatment

IIW International Institute of Welding

MPD Melting Point Depression

NMM Nanostructured Metal Multilayer

PIT Pneumatic Impact Treatment

PSB Persistent Slip Bands

PVD Physical Vapor Deposition

SEM Scanning Electron Microscopy

TEM Transmission Electron Microscopy

TIG Tungsten Inert Gas

UIT Ultrasonic Impact Treatment

XFEM Extended Finite Element Method

XRD X-Ray Diffraction

Chapter 1

Introduction

This thesis introduces a new post-weld treatment method that is based on the application of Nanostructured Metal Multilayer (NMM) on welded joints.

1.1 Problem Definition

The maintenance of infrastructure consumes considerable amounts of money worldwide and accounts for 1.1 % of the European GDP [1]. Bridges and engineering structures form a good proportion of these costs. Budget deficiencies and maintenance backlog lead to the premature aging of structures [1]. While cutting costs in the present, these maintenance backlogs increase the costs in the future and might pose a risk for the users [2]. A lot of engineering failures in the last decades can be directly linked to inadequate maintenance and surveillance. This is also true for steel bridges [3].

One of the biggest problems for steel structures, next to corrosion, are fatigue damages that occur under cyclic loading. Even so, these cyclic loads are much smaller than the ultimate strength of the structure, these loads will induce small damages and micro cracks that grow with each cycle. This leads to a crack propagation in a way that the structures can only endure a certain number of load cycles before fatigue maintenance becomes necessary or failure occurs [4]. For steel structures, the beginning of fatigue cracks is often found at the welded joints.

An impressive example of a fatigue fracture that developed from a small welding error, is the Hernando de Soto Bridge on the course of the I40 highway in Memphis, Tennessee [5]. The bridge consists of two connected tied-arch spans. The arches carry the vertical loads to the foundations, while tension members carry the horizontal loads

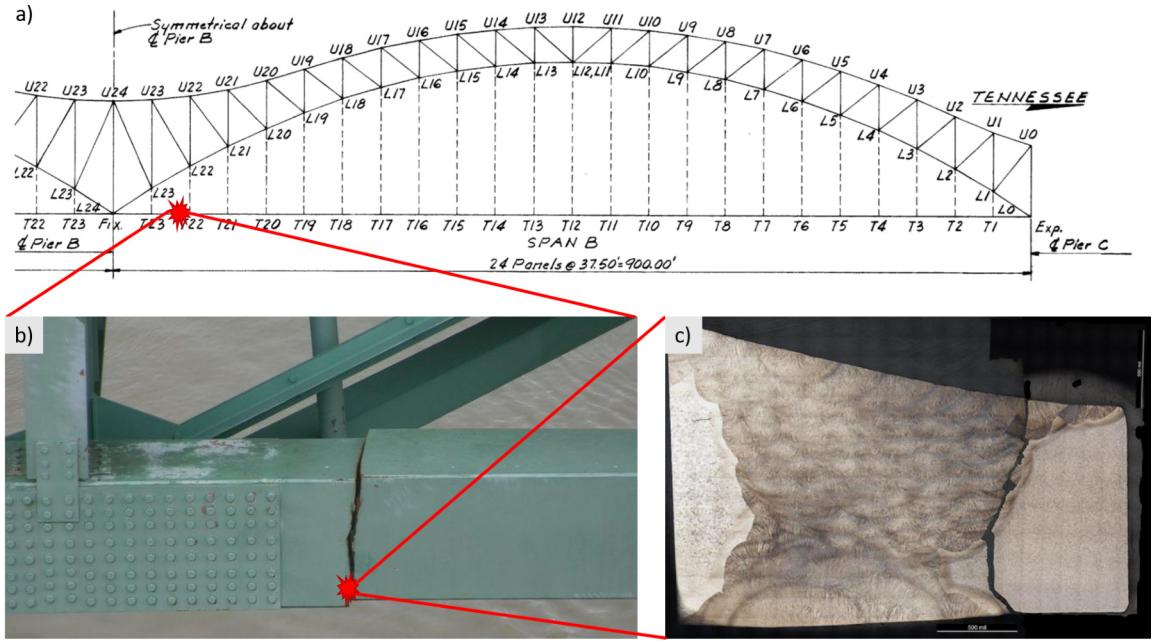

Figure 1.1: Fracture in the tie girder of the Hernando de Soto Bridge showing the fracture from macro to micro scale; a) overview of the Hernando de Soto Bridge east span arch; b) photo of the fracture in the tie girder; c) micrograph of the area where the crack progress started; adapted from [5]

from the arches. One of these tension members fractured due to a fatigue crack. Even so, the crack could be found in hindsight on pictures from 2016 and drone footage of an inspection from 2019, it went undetected for at least four years; all the while the crack was growing larger with every load cycle. The tie girder fracture was finally caught by engineers working on a different part of the bridge. Luckily, the loss of this key tie girder did not lead to a bridge collapse, as loads could be transferred over non-essential trusses. Figure 1.1 shows the fracture in the tie girder in three pictures from macro to micro scale. While the Hernando de Soto Bridge avoided disaster, by good fortune only, the bridge closure still costed the local economy up to 2 million dollars a day.

Bridge failures especially do not only come with a high death toll but also have an influence on the local economy and community, as research about the Morandi Viaduct collapse in 2018 shows [6, 7].

Another example of the importance of fatigue lifetime can be found in on-shore and off-shore wind turbines [8]. One of the limiting factors in the wind energy and offshore market is the fatigue lifetime, with huge economical implications if life extensions can be attained, as costs can be distributed over a longer period and the wind turbine can produce more electricity over its lifetime.

There are two big approaches in the maintenance industry to increase the safety of structures, as well as reducing the costs and increasing the longevity and thereby sustainability of infrastructures [9]. On the one hand, structural health monitoring is looking to enhance structures with sensors that can tell engineers exactly what the status of structural members is and detect damages sooner. On the other hand, the use of new building methods and new materials is looking to make the infrastructure more reliable so that the lifetime of structures can be increased and the structures require less maintenance.

In this thesis, a new post-weld treatment method is introduced, which relies on a high-performance coating that prolongs the crack initiation phase and the lifetime of welded components. The coating on the steel substrate is a nanostructured Cu/Ni metal multilayer.

Nanostructured materials have been known to possess special material properties and have been the focus of material research in many areas [10, 11]. Especially NMM are known for their superior mechanical properties regarding tensile strength and fatigue resistance, among other things [11]. Using these high strength materials as coatings can drastically change the surface properties and overall behavior of coated materials.

With this research, the possibility of Cu/Ni metal multilayers as high-performance coatings for the strengthening of civil infrastructures is explored.

1.2 Research Design and Scope

In order to show the enhanced fatigue properties of Cu/Ni nanolaminate coated structures, tensile test specimen are electroplated with NMM using a single bath technique. The specimens are then tested in tension-tension fatigue and a first S-N curve is created comparing as-welded and NMM coated samples.

Investigations of the failure mechanisms of Cu/Ni metal multilayers with Scanning Electron Microscopy (SEM), Energy-dispersive X-ray Spectroscopy (EDX) as well as Transmission Electron Microscopy (TEM) lead to a more profound understanding of the fatigue increasing properties of Cu/Ni metal multilayers.

The lay-up of the nanolaminate and the electrodeposition process was not optimized as part of this research. The electrodeposition process was adapted from existing papers and basic literature. The lay-up of the coating was chosen arbitrarily and needs to be investigated further in the future.

Numerous investigations and ideas did not fit in the scope of this thesis, some of which are added to this work as possible incipience for future research.

1.3 Structure of the Thesis

The thesis is structured into eight chapters, including the introduction in chapter 1.

Chapter 2 gives a brief introduction to nanostructured materials in section 2.1 and nanolaminate materials specifically in section 2.1.1; the electrodeposition process in section 2.2 and finally on fatigue in section 2.3.

In chapter 3, the methods for the production of tensile specimen, test methods and sample preparation methods are described in detail. Since the electrodeposition process is described at a greater length, this topic is given a separate chapter in chapter 4.

The results for the tension-tension fatigue tests, as described in section 3.2, are shown and discussed in chapter 5.

The investigation results of the SEM, EDX and TEM investigations are presented in chapter 6. In this chapter, the material is characterized and hypotheses on failure mechanisms are derived from the investigations and discussed further.

Chapter 7 gives an outlook on topics that were not elaborated upon in the scope of this work, but are of interest for future research or the optimization of the electrodeposition process.

The final chapter 8 closes this thesis with a short summary.

Chapter 2

Theoretical Background

This chapter can only give a shallow overview of the complex topics that are combined in this thesis. Nonetheless, the most important background information for the understanding of this thesis is summarized herein. Since nanolaminate patches are produced by electrodeposition and used to tackle fatigue problems, this chapter is structured accordingly into three parts. In section 2.1 an overview is given of the history of nanotechnology and the benefits of Nanostructured Metal Multilayer (NMM) with a special focus on Cu/Ni nanostructured multilayers. In section 2.2 the electrodeposition process and its benefits for the synthesizing of metal multilayers is explicated. Section 2.3 gives the basic context for the fatigue subject with an emphasis on welded structures.

2.1 Nanostructured Materials

Material properties often change when their dimensions approach the nanoscale. The term nano, which comes from the Greek *nanos* meaning dwarf, simply describes the scale being on the scale of one billionth (10^{-9}) of a meter. In the context of nanotechnology, this is meant in the sense that the technology is working with particles, pigments, structures, or grains in the range between 1 nm and 100 nm. The production of nanomaterials can be either bottom-up, or top-down.

Top-down fabrication for the production of nanostructured materials has been used for a very long time, i.e. in the production of Roman dichroic glass [12] or ancient Damascus steel [13]; top-down fabrication is still relevant today, esp. for the production of bulk nanostructured materials [14]. Modern fabrication techniques allow the bottom-up production of nanostructured materials, basically fabricating materi-

als intentionally atom by atom and layer by layer to produce a material with clearly controlled material properties [15, 11].

Electrodeposition is the first bottom-up production technique. The production of Nanostructured Metal Multilayer (NMM) and super lattices (German: *Übergitter*) with electrodeposition has been reported as early as 1923 [16] and this production method is still of interest [10]. Especially through the magnetic and superconductive properties and the rise of new calculation methods and the new sputtering methods, supper lattices and NMM have seen a great rise of interest for researchers in the 70s and 80s of the last century [17] that still exists to this day.

In recent years, nanotechnology has been in the focus of both research and industry alike. Current industrial uses of nanotechnology are found in surface technology, pigments, micro electronics, semiconductors and many other fields [15].

Nanostructured materials and NMM in particular have been researched due to their extraordinary material properties regarding corrosion resistance, strength, magnetism, radiation resistance and fatigue resistance, as discussed in the following sections. A good overview paper about nanoscale metallic multilayers has been published in 2020 by Sáenz-Trevizo and Hodge [11].

2.1.1 Nanostructured Metal Multilayers

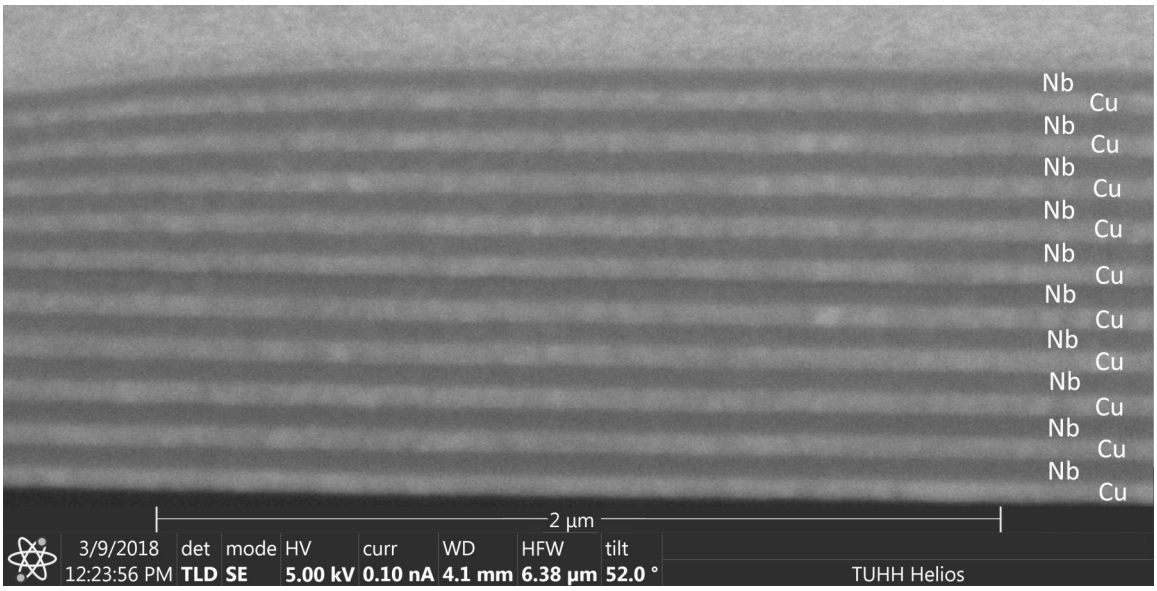

Figure 2.1: Exemplary cross-section SEM image of a Cu/Nb NMM produced by PVD

NMM are known to possess material properties that are vastly different from the bulk materials and can be tailored towards special material requirements [15, 11]. This applies to magnetism [17], conductivity [17], radiation damage tolerance [18, 19], corrosion resistance [20, 21, 22], strength [23, 24, 25] and fatigue resistance [26, 27]. An example of a NMM lay-up can be seen in figure 2.1. Practical implementations are numerous and an overview of possible fields for the application can be taken from recent overview papers [10, 11].

The focus of this thesis lies on the mechanical properties of Cu/Ni NMM, especially on the properties under fatigue loading. Therefore, the mechanical properties of NMM are presented according to literature. The general behavior is presented below and for Cu/Ni nanolaminate in particular in the following section.

The strength and hardness roughly follow the Hall-Petch (and reverse Hall-Petch) relationship, but scale with the sublayer thicknesses a and b and the supper lattice wavelength Λ rather than the grain size [28, 29, 30, 31, 32]. NMM have been reported to reach a maximum strength of $E/50$, with E being the Young's modulus. This is getting close to the theoretical maximum strength σ_{th} of materials [31].

For the Young's modulus and the elasticity, there are no larger deviations from the rule of mixture and Hooke's law [25, 33].

The increase of the mechanical properties is often attributed to the number of interfaces inside a nanolaminate because both coherent and incoherent interfaces will have an impact on crack propagation behavior and therefore the strength and hardness of nanostructured NMM [28, 32]. Since there are a lot of different multilayer systems with a lot of different interface mechanics, a lot of recent research has been focusing on interface mechanisms for different metal-metal, metal-ceramic and ceramic-ceramic systems. For small Λ, the interface mechanisms are getting more important for the strength of the NMM [31, 34]. The research of *Carpenter et al.* shows that not only the wavelength Λ influences the mechanical properties, but also the volume fraction of the two metals [35].

Further strengthening mechanisms seem to apply to the strengthening mechanisms of NMM like the Orowan-model [36, 37], as well as Peach-Köhler strengthening [38]. Confined Layer Slip (CLS) is a theory that describes the build up of Orowan-type loops between the interfaces and stay confined to only one of the metal layers. More complex CLS models can also be fitted to experimental data [39]. But ultimately, the Hall-Petch model seems to hold up best [28], while the other models will explain the deviations for $\Lambda \leq 10^{-7}$ m [37]. A thorough investigation into the different parameters that goes into the strength of nanolaminate structures has been written

down by *Amit Misra* in the book 'Nanostructured Control of Materials' [31, 15]. For different Λ different strengthening mechanisms are prevalent, as shown in figure 2.2. Another (and more recent) overview of high strength nanolaminate has been published in 2020 by *Nasim et al.* [29].

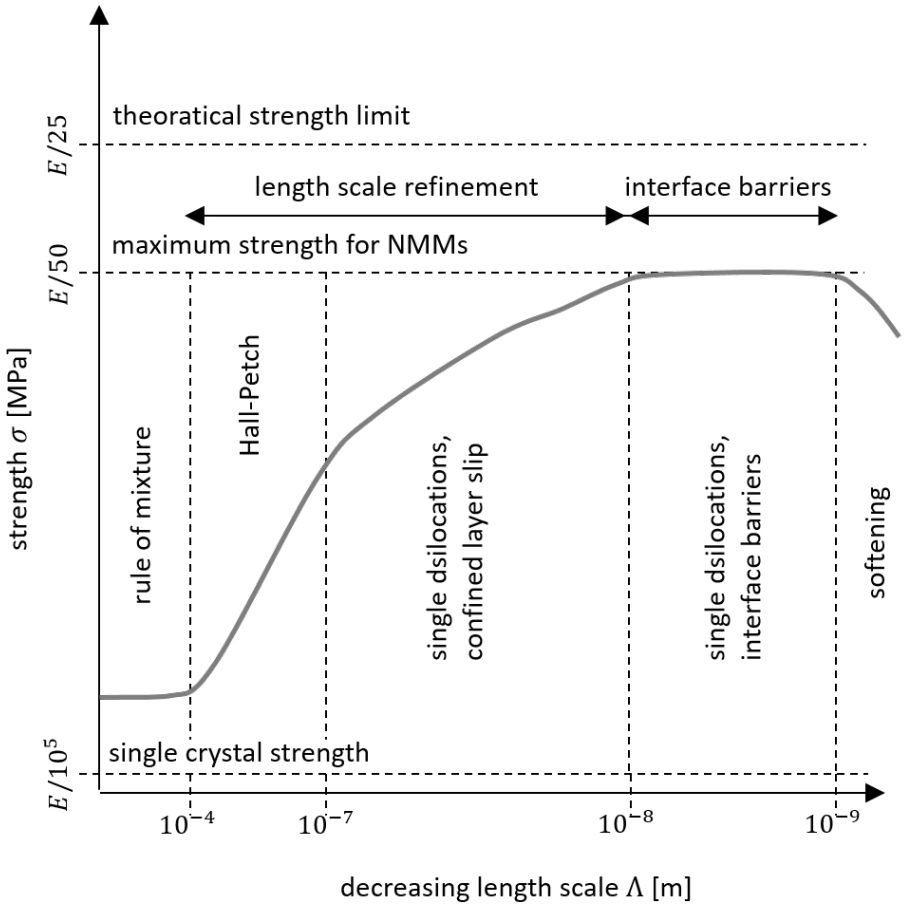

Figure 2.2: Schematic of NMM ultimate strength with the prevalent strengthening mechanisms dependent on the laminate wavelength; adapted from [31]

Molecular dynamic simulations of NMM have been used successfully to estimate a theoretical strength and hardness for NMM and derive failure mechanisms [40, 41, 42, 34, 43]. Since there are complex failure mechanisms at work, these simulations are hard to validate and the results hard to verify. Especially the calculated yield stresses should be questioned because test results on real samples do not always reflect the simulated results, as shown for example in [42], where the simulated yield strength is getting close to the measured hardness of the specimen and then drops rapidly into a regime that corresponds to a more probable strength of approximately 1/3 of the reported hardness values.

One of the problems of NMM structures is the thermal stability. NMM are metastable and will lose their lay-up under high temperatures, as shown impressively by [44]. This might be a result of Melting Point Depression (MPD) [45], solid state diffusion [46] and might also occur way below the melting point of the base materials. The MPD is a function of layer thickness [47]. For some NMM with well-ordered bi-material interfaces, thermal stability was reported up to 500 degrees centigrade [48].

2.1.2 Testing Methods for Nanolaminate Structures

In the following, different testing methods for nanolaminate structures are presented exemplarily. The cited material is arbitrary.

Different testing methods are standard practice for the testing of NMM thin films and coatings. The most popular method by far is nanoindentation [29]. The hardness of the material is tested by indenting the surface with a diamond Berkovich tip and measuring the load and indentation depth. Since the geometry and hardness of the tip is known, hardness, strength, and Young's modulus can be derived from the measurement [49, 50]. Most research is also supported by Scanning Electron Microscopy (SEM) and Transmission Electron Microscopy (TEM) investigations. In some cases, in situ TEM [51, 52] and in situ SEM [53] investigations are used to assess failure mechanisms.

More direct approaches for measuring the mechanical properties of NMM are micro-pillar [54], micro-beam [55] and micro-tensile [56] testing of specimen.

There is also sparse research on fatigue testing, for example of freestanding beams with the resonant frequency method [26] or by nano-impact testing for dynamic impact fatigue [57].

Another testing method that is viable for thin films is bulge testing, where the free standing thin film is displaced by a pressure perpendicular to the surface and a stress strain relationship can be derived from the bulge displacement and the applied pressure [58].

Annealing tests will show the thermal stability of metal nanolaminate structures [44, 46, 47].

X-Ray Diffraction (XRD) measurements provide insight into the lay-up, the residual stresses of NMM [59], while in situ XRD straining tests [53] can provide insight into the load distribution between the layers under load; in situ XRD annealing tests [59] show changes in microstructure under high temperatures.

2.1.3 Cu/Ni Nanolaminate Structures

Cu/Ni NMM are of particular interest because they are easily producible (cf. chapter 2.2).

The mechanical failure and strengthening mechanisms are highly dependent on the nanolaminate lay-up and the interface, as described above. Cu/Ni multilayers have semi-coherent interfaces, which do have a lattice mismatch that will create both misfit-dislocations and small coherency strains, which will in turn influence the plastic behavior and the behavior at small Λ [30, 60]. The Cu/Ni multilayers will also experience CLS as deformations travel through the material [30]. Research into multiscale Cu/Ni multilayers with nano-scale Cu layers and micro-scale Ni layers, shows that in this area the normal rules of mixture for composite materials apply again [61].

The ultimate strength of electrodeposited Cu/Ni NMM has been reported as $1,300$ MPa for Cu/Ni layers with a layer thickness of 10 nm and 90 nm respectively [56, 62] peaking at $1,900$ MPa for Cu/Ni with a layer thickness of 2 nm and 18 nm respectively [63]. While these results show the possibilities of Cu/Ni layers, they do not seem to reflect the highest possible strength of Cu/Ni NMM, which makes sense considering that the Cu layers are in the 1 nm-range and are in the softening area of single dislocations. For Cu/Ni NMM with a layer thickness of 50 nm for the Cu and Ni layers produced by Accumulative Roll Bonding (ARB) fracture is reported in delamination mode at a tensile strength of 950 MPa [64].

Unfortunately, there is not a lot of tension test data for Cu/Ni NMM because most research focused on hardness and nanoindentation testing [35]. Micro-pillar compression testing yielded flow strengths of 1900 MPa for Cu/Ni with a layer thickness of 21 nm for the Cu and Ni layers [54] and is in good accordance with the theory [35].

The concept of 'smaller is better' for nanomaterials does not necessarily hold up for Cu/Ni NMM [35]. Nanoindentation tests show, for example, that the relative bi-layer thickness also has an influence on the hardness of Cu/Ni NMM [49] and theoretical calculations backed by nanoindentation tests indicate that the high hardness of Cu/Ni NMM can also be reached with a bigger Λ, relying more on the semi-coherent interfaces than other strengthening mechanisms [35]. With the bigger Λ, an increase in ductility is available, which will make applications possible that require both high hardness and high ductility. This is, for example, interesting for materials under cyclic loading; fatigue results indicate that a higher Λ might indeed result in higher lifetimes, at least for lower stress amplitudes [65].

Different practical areas for the use of Cu/Ni nanolaminate have been proposed:

- Coating to increase wear resistance [49, 66]
- Coating against fretting [67]
- Coating unnotched specimen to increase fatigue resistance [27]
- Coating joints as post-weld treatment [68]

While the wear and fretting resistance are not of interest for this work, the fatigue resistance is and the corresponding research will be presented in the following.

Stoudt et al. used Cu/Ni nanolaminate coatings to coat unnotched cylindrical copper fatigue samples [27]. Figure 2.3 shows the fatigue results in a Weibull scale probability life diagram, which clearly shows that the Cu/Ni NMM increases the lifetime more than tenfold and that the effect can be attributed to the NMM coating, since both pure Ni and pure Cu coatings did not influence the fatigue resistance.

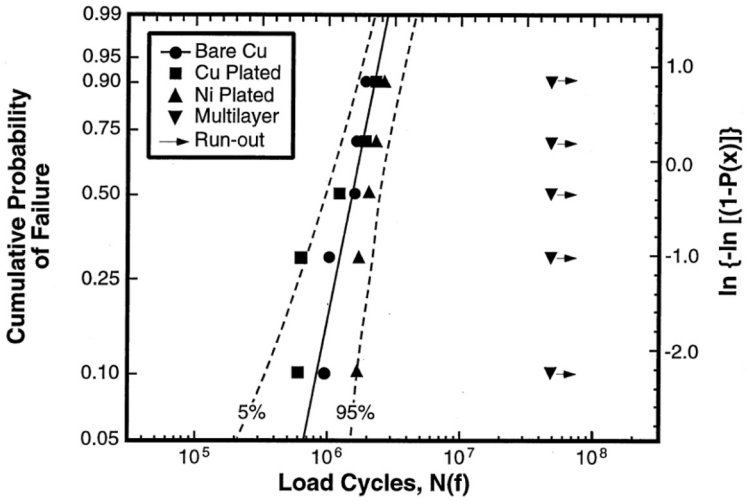

Figure 2.3: Weibull probability life diagram for Cu samples bare, coated with Cu, coated with Ni and coated with a Cu/Ni NMM [27]

Kaneko et al. repeated the experiments by *Stoudt et al.* confirming the results [65]. Additionally, this study shows, with Electron Channelling Contrast Imaging (ECCI) measurements, that the Ni and the Cu/Ni coatings inhibit dislocations near the surface. While the Ni also contains the dislocations near the surface, the Ni layer

does not enhance the lifetime of the samples. A possible explanation for this behavior will be given in chapter 6.

In this work, the coating is applied to a notched sample as a post-weld treatment and even so the results are not as unequivocal, the Cu/Ni NMM coating still prolongs the lifetime of the fatigue samples as discussed later in chapter 8.

2.2 Electrodeposition of Nanolaminate Structures

One of the cheapest ways to produce nanolaminate structures is electrodeposition [10]. There are two ways to produce nanolaminate structures by electrodeposition, namely the dual bath method described in 2.2.1 and the single bath method described in 2.2.2. In this work, steel specimen are coated with the single bath method as described in chapter 4. Alternative methods for the synthetization of NMM that do not rely on electrodeposition are described in section 2.2.3.

The electrodeposition process is a well known and well documented process [69, 70, 71, 72]. In contrast to the alternatives, it is cheap and easy to establish [69, 10]. The NMM metal combinations are limited by the available and stable electrolytes for the electrodeposition process [29]. Especially, the integration of ceramic phases into the nanostructure is not possible with electrodeposition.

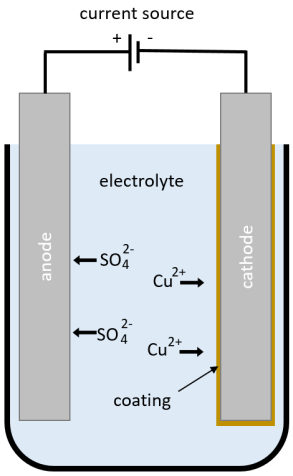

Figure 2.4: Example for a Cu electrodeposition process from a sulfate bath

Electrodeposition is based on the deposition of metals with a galvanic cell to the surface of a conductive substrate. The galvanic cell consists of an electrolyte, an anode, a cathode, and a power source, as figure 2.4 shows exemplarily for Cu deposition from a Cu-sulfate bath. By applying a current to the galvanic cell, the metal salts in the electrolyte split up into positively charged cations (i.e. Cu^{2+} or Ni^{2+}) and negatively charged anions (i.e. SO_4^{2-}). The anions will travel against the current flow with the electron flow towards the anode, while the cations travel with the current flow and against the electron flow. At the anode, the anions give up the surplus electrons to the anode, taking out a piece of the anode to recombine to a soluble salt and dissolve back into the electrolyte. At the cathode, the cations take up the missing electrons, thereby depositing on the surface of the cathode forming a metal bond with the substrate. This process is shown schematically in figure 2.5.

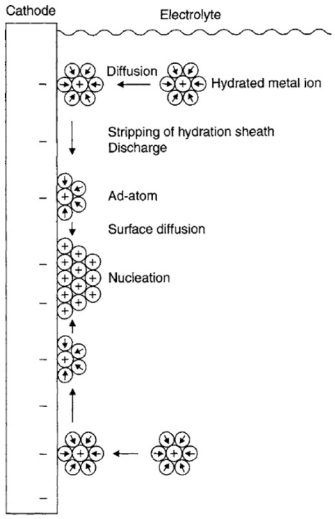

Figure 2.5: Deposition process of metal ions to the surface of the cathode, showing migration, surface diffusion and nucleation [73]

This makes the cathode the substrate on which a metal film is deposited. The anode replenishes the bath with metal ions and is slowly dissolved into the electrolyte.

The deposition thickness d is determined by equation 2.1.

$$d = \frac{\ddot{A}_e \cdot I \cdot t}{A \cdot \rho} \cdot \Theta_k \tag{2.1}$$

The electrochemical equivalent $\ddot{A}_e$ and the density ρ are material constants, the cathodic current efficiency Θ_k is an electrolyte and bath related constant, and the cathode surface area A is a constant related to the specimen. This makes the depo-

sition dependable on the applied current I and deposition time t or vice versa the applied electric charge $Q = I \cdot t$.

2.2.1 Dual Bath Method

The dual bath method was the first method for the production of NMM; the method was first described in 1930 [16].

Two different electrolytes are used to deposit two different metals onto a substrate, as depicted in figure 2.6. After the cleansing and surface activation, the substrate is lowered into the electrolyte and plated with the first metal. By applying a current to the galvanic circuit, the first metal is deposited to the surface of the cathode. The sample is then taken out of the first electrolyte, cleansed, and then lowered into the second electrolyte with the dissolved second metal. After the second metal is deposited, the process can be repeated, until the desired nanolaminate lay-up is attained. The individual layer-thicknesses can be controlled by the current density and deposition time. The length of the process is highly dependent on the transfer process, while the quality of the process is highly dependent on the cleansing during the transfer process. The time in the electrolytes and the deposition times are relatively short.

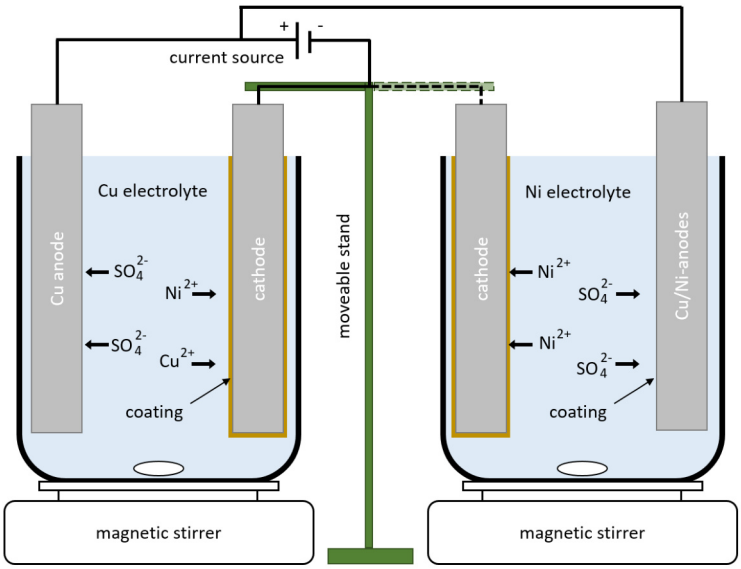

Figure 2.6: Example for a dual bath electrodeposition process with a Cu and Ni sulfate bath

The advantages of this process are that two (or more) electrolytes can be used for electroplating basically all metals that can be electroplated onto a substrate as a NMM,

the short deposition times and the use of simple electrolytes. The disadvantage is that the sample has to be taken from the electrolytes and cleansed regularly and the NMM is thereby exposed to air at every interface. This can lead to problems with oxides at the interface. Additionally, the regular transfer and cleansing makes the NMM production labor intensive and automatizing the process complicated. Nonetheless, there is research into automated dual bath methods with multiple jet electrodeposition [74].

Recently, the dual bath method has also been used for the production of multiscale multilayers [61].

2.2.2 Single Bath Method

The single bath method relies on the different standard reduction potentials of the two metals dissolved in the electrolyte. By applying a low current to the galvanic cell, which is below the activation voltage for the deposition reaction of the less noble metal, only the more noble metal with the higher standard reduction potential will be deposited to the surface of the cathode. By applying a high current to the single bath, both metals will be deposited to the sample according to the mass percentage in the electrolyte. With a low mass percentage of the more noble metal in the electrolyte, the two metals in the electrolyte can be deposited individually.

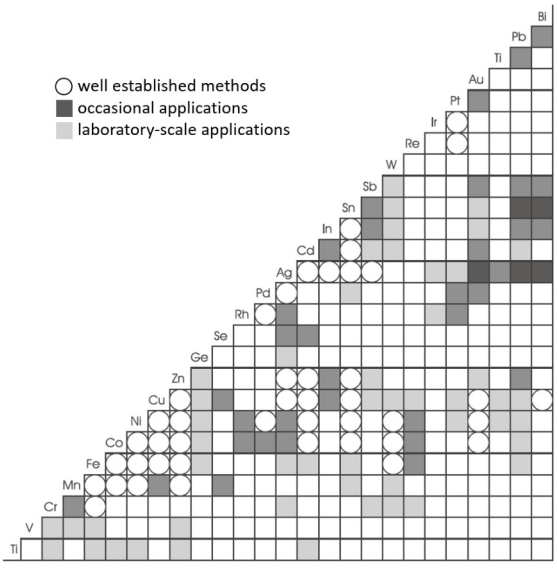

Figure 2.7: Metal combinations that have been used successfully for the deposition from a single electrolyte [69]

The deposition of different metals is limited by the electrolytes, which need to be stable and need a potential difference for the deposition that is large enough to deposit both metals individually. Figure 2.7 shows a grid with the metal combinations that have been electroplated as NMM or as an alloy from the same bath [69].

Figure 2.8 shows an example for a single bath electrodeposition process. The process will need two different anodes or an alternative way of keeping the composition of the electrolyte stable (i.e. [10]).

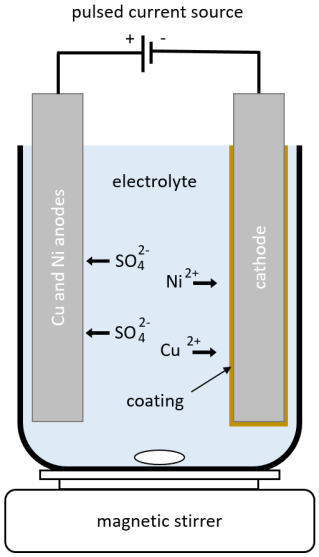

Figure 2.8: Example for a single bath electrodeposition process with a Cu/Ni sulfate bath

With a programmable pulsed current source, the deposition process can easily be automated. But the deposition process is a lot slower than the deposition of metals from an electrolyte with only one metal. As an advantage, no transfers between different electrolytes are necessary. The complex electrolyte inhibits a restriction on the combination of metals that can be combined to produce NMM. Some researchers even suggest that the single bath is the only viable method for practical applications [56] and there is research into brush plated multilayers from single bath electrolytes [66].

2.2.3 Alternate Production Methods for Nanolaminate Structures

Since most other processes rely on vacuum to function, these methods are not scalable and therefore not applicable for the coating of larger parts. Accumulative Roll Bonding (ARB) on the other hand, is scalable but restricted in the metals that can be used to create nanolaminate structures. Nonetheless, the alternatives are presented in the following.

Vapor Deposition

Vapor deposition is a vast category of deposition techniques that rely on the deposition of metals, alloys or ceramics from a vaporized source. The two main vapor deposition techniques are Physical Vapor Deposition (PVD) and Chemical Vapor Deposition (CVD) and are shown in figure 2.9. The process is well known and established both for thin film material manufacturing [75] and microelectronics [76].

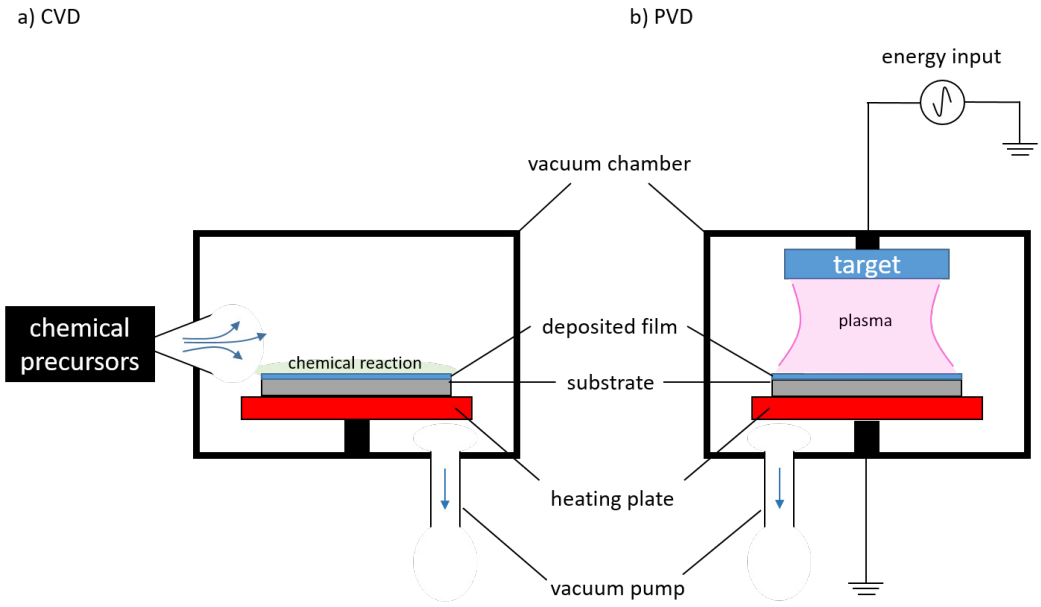

Figure 2.9: Schematic depiction of a) the CVD process and b) the PVD process

CVD uses chemical precursors, which will be broken down by an energy input, releasing the metal ions that will be deposited to a substrate [75]. For NMM deposition, different metals can be deposited by flooding the chamber with different precursors in rapid succession.

PVD uses metal targets that are evaporated by a high-energy impact, which can be generated by a high voltage discharge, an electron beam, a plasma, or a laser. The evaporated metal ion gas will then sublimate onto surfaces within the sputtering chamber [75]. With multiple targets in an evaporation or sputtering chamber, different metals can be deposited onto the substrate to create NMM.

The vapor deposition processes allow a good control over the microstructure, which makes PVD sputtering, for example, convenient for research processes [77] and most of the research cited in section 2.1.1 uses vapor deposition techniques. One of the disadvantages of vapor deposition is that the process is only working in a vacuum, making the scalability to larger parts a problem. Additionally, the vapor deposition process produces high residual stresses in multilayer coatings, which will lead to micro-cracking for small Λ [78]. This also limits the thickness of vapor deposited NMM to a few micrometers.

Accumulative Roll Bonding

The ARB process does not require a vacuum and relies on the plastic deformation of two (or more) different metal sheets that are rolled out on top of each other. This process can be repeated to create NMM [79]. Figure 2.10 shows the process. This process only works for metals with a high formability, and nanolaminate can only be created if the sheets are thin enough to roll them out to layers with a thickness below 100 nm.

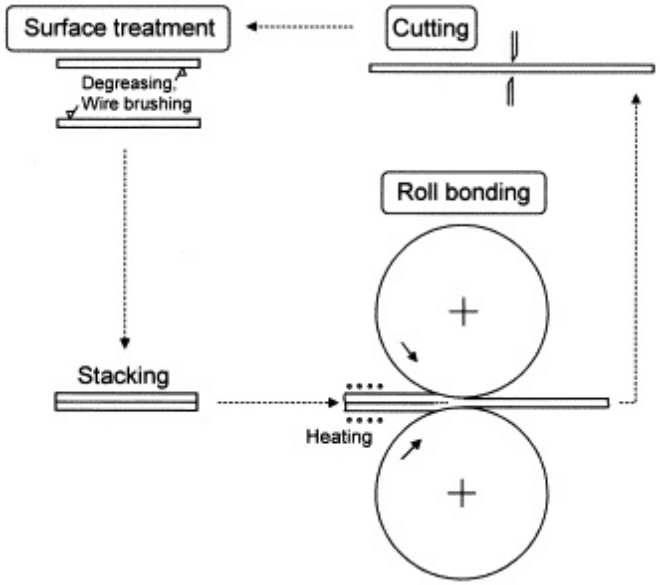

Figure 2.10: Schematic depiction of the ARB process [79]

The process is scalable and easily industrialized because roll bonding is a well-known process. It is possible to produce high strength nanolaminate structures with a sub-layer thickness of < 100 nm as sheets with a thickness of 1 mm for certain cubic metal combinations [80, 81]. Alas, these plates are not applicable as thin films or coatings. The interfaces of ARB NMM are not as good as the interfaces of electroplated or sputtered NMM, since delamination is the predominant failure mechanism [64].

2.3 Fatigue

Fatigue of structural components is one of the factors that makes structures age and limits their lifetime. The fatigue of structures is based on the formation and continual growth of cracks under cyclic loading. The crack formation is usually separated into a crack initiation phase, a crack propagation phase, and an unstable crack propagation that leads to failure as shown in figure 2.11. A good overview of the fatigue of metals is given by *Schijve* in the book 'Fatigue of Structures and Materials' [4].

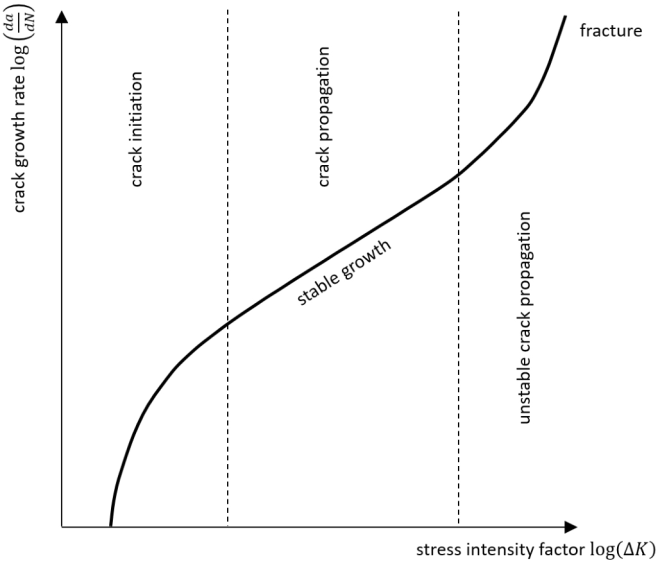

Figure 2.11: Generalized fatigue growth rate as a function of stress intensity

Crack propagation, especially in the stable regime, is well understood and can be calculated, for example, with the Paris-Erdogan law [82]. While the crack initiation is well understood qualitatively with cyclic slip, followed by a crack nucleation and micro crack growth, these mechanisms are hard to ascertain quantitatively [4, 83]. Since the lifetime is predominantly influenced by the crack initiation phase, reliable calculation methods for the prediction of the lifetime of structures is not available.

For engineering purposes, design recommendations and S-N curves that rely on a huge probabilistic data set have been the main focus in fatigue design and are included in almost all engineering standards [83], i.e. the Eurocode 3 for steel design [84] or International Institute of Welding (IIW) recommendations [85]. Even though there are numerous factors that go into the fatigue failure of notched specimen, like stress concentration, loading type, cyclic stress ratio, notch size, surface roughness and type of material [83, 4, 85], the nominal stress approach, as used in most design codes, does not take those factors into account directly. Instead, the nominal stress approach categorizes different notches according to their notch geometry and supplies S-N curves for the design (cf. section 2.3.1). Only areas with high demands on fatigue life and weight like automotive, aeronautics or unconventional applications will use more concise methods, like the structural stress approach [83]. More local approaches exist and take more parameters into account as compiled by *Radaj* in the book 'Fatigue Assessment of Welded Joints' [83], but those models are hard to validate due to the high scatter in input parameters and high scatter of fatigue test results [4, 83].

Crack initiation is different for notched and unnotched samples. But it is well known, that fatigue cracks in high cycle fatigue will almost always start at the surface of materials. For specimen with large internal notches, like welding errors or inclusions, this does not hold true. One of the best explanations for surface crack initiation is that cyclic loading will create Persistent Slip Bands (PSB) that travel through the material to relief areas of high stress and strain, as a cyclic plasticity response [86]. If the redistribution of stress and strain reduces the internal stress strain state below a certain threshold, the formation of PSB will stop; otherwise, the PSB will wander to the surface of metals and create intrusions and extrusions that will grow with repeated stress cycles [87, 88]. Fatigue crack growth then occurs from the intrusions, following normal crack growth rules [88].

2.3.1 Weld Notches

For static loads, welds are seldom the weakest link of a structure and, with the right filler material, have a higher strength and hardness than the base material. For cyclic loading, welded joints are almost always a problem for the fatigue strength and introduce a notch from which a crack might form [83, 85]. The notch effect can be separated in a geometrical part and a technological part [89].

The geometrical influence is due to the reinforcement height of the weld and the root penetration, with a sharp geometrical change at the toe with parameters like the weld toe radius, the flank angle, secondary notch depth and weld reinforcement height [90].

These geometrical changes create a heightened multi-axial stress state, which will be the nucleation point for crack initiation as described above.

The technological part is due to the change in material composition, hardness changes and residual stresses introduced by the welding process. The material in the Heat Affected Zone (HAZ) is undergoing an unplanned heat treatment, which will change the material properties dependent on the cooling rate and the distance to the weld. Since the temperature gradually decreases from the weld outward, the material will undergo different kinds of heat treatments, creating areas that are prone to crack propagation [83, 89].

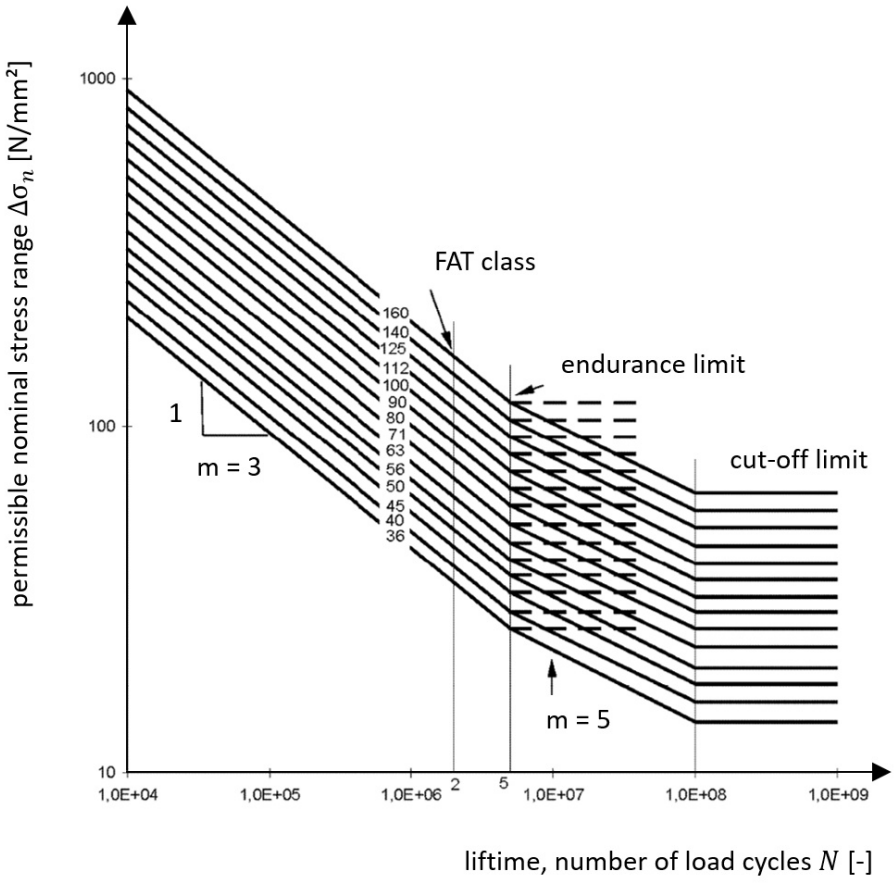

Figure 2.12: S-N curves for different fatigue classes according to EC 3 [84]

As mentioned above, standards like Eurocode 3 [84] for the design of steel structures use a nominal stress approach and sort different welds into fatigue classes, notch cases, or FAT classes [84, 85] based on the geometry and the kind of weld detail. Each fatigue class corresponds to an S-N curve, as depicted in figure 2.12, which can be used to design steel structures against fatigue damage. Since this categorization is based on fatigue tests of real specimen, important influences like base material, filler material, surface finish, weld quality, cross-section, or loading type [83] are only

accounted for indirectly in this model. Figure 2.13 shows the main parameters and relations of the nominal stress approach for welded joints. Post-weld treatments are not included into the code, and the notch cases apply for untreated welds. For the influence of post-weld treatments, section 2.3.2 provides further information.

As an example, the categorization of double sided butt-welds is shown in figure 2.14 according to EC 3. Depending on the geometry of the weld height, butt-welds are either fatigue class 80 or 90. Or if the weld is flush, by flattening the weld height, the geometric influence of the weld is even lower and the fatigue class 112 applies. For welds with a thickness bigger than 25 mm, the fatigue class is lowered.

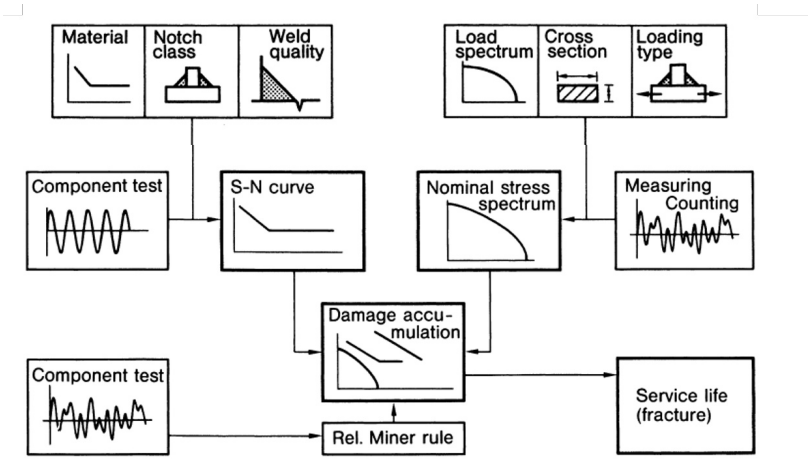

Figure 2.13: Main parameters and concept of the nominal stress approach [83]

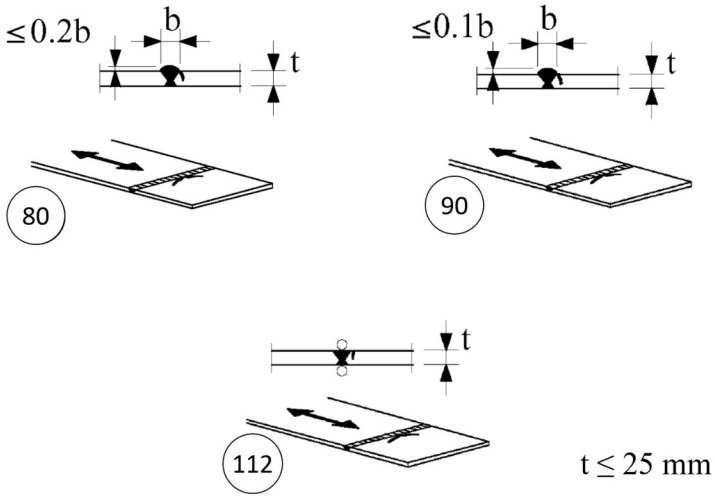

Figure 2.14: Fatigue classes for butt-welds with different weld heights according to EC 3 [84]

2.3.2 Post-Weld Treatments

In order to reduce the influence of the notch on the lifetime of welded specimen described in section 2.3.1, different post weld treatment methods have been developed. An overview of existing post-weld treatment methods can be seen in figure 2.15.

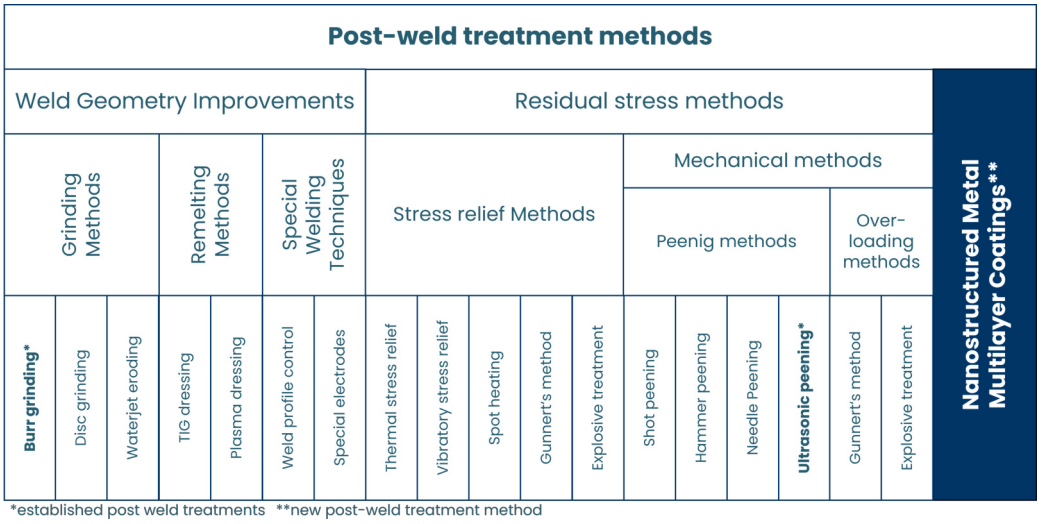

Figure 2.15: Overview of post-weld treatment methods (adapted from [91])

Even though there are a lot of different post-weld treatment methods, these methods can be grouped in two categories according to how the post weld-treatment method affects the welded area [91].

The first category includes methods that improve the weld geometry. Improvement of the geometry will reduce the stresses at the notch and thereby the lifetime of welded structures.

The second category focuses on the change of residual stresses close to the surface of the joints. By relieving residual tension stresses or introducing compression stresses, the fatigue stress ratio will be decreased near the surface and at the crack tip, which in turn increases the lifetime.

Figure 2.16 shows schematically how the different post-weld treatments change the welded joint.

Even though there are plenty of different methods, for the improvement of welded joints, burr grinding, Tungsten Inert Gas (TIG) dressing, and hammer/needle peening are the methods that have been considered for widespread practical application [92, 85]. Furthermore, only the High Frequency Mechanical Impact (HFMI) methods (Pneumatic Impact Treatment (PIT), High Frequency Impact Treatment (HiFIT), Ultrasonic Impact Treatment (UIT)) have been met with International Institute of

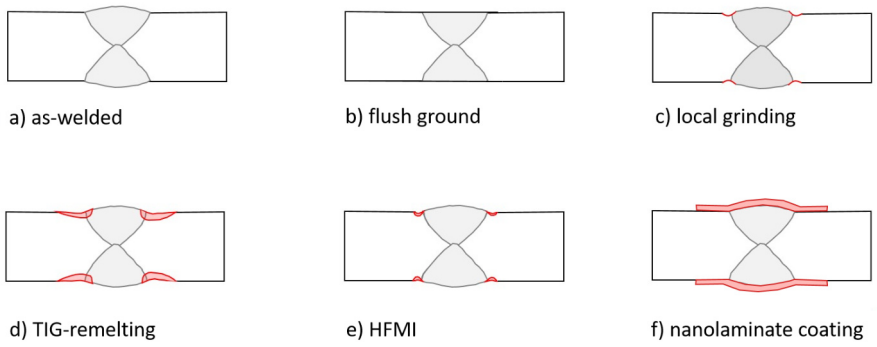

Figure 2.16: Schematic depiction of post-weld treatment methods for butt-welds; a) as-welded cross-section of a butt-weld; b) flush ground surface; c) local grinding of the weld toe; d) TIG-remelted weld toes; e) HFMI treated weld toes; f) weld coated with NMM

Welding (IIW) and Deutscher Ausschuss für Stahlbau (DASt) recommendations for the improvement of the fatigue classes [93, 92, 94] and are currently in discussion for the next generation of the Eurocode [95, 96]. HFMI are also the methods that have seen economical and reliable applications [96, 97]. While there are slight differences in the HFMI devices and methods, they all rely on the introduction of residual compressive stresses at the weld toe [98]. This is why the impact of HFMI-improvements reduces for stress ratios larger than $R = -0,125$ [85]. Moreover, there is a region in the S-N curve for high stresses and below an expected lifetime of 72,000 cycles, where HFMI has no effect [96] or even a negative effect [92] on the lifetime of welded joints. The S-N curve for HFMI treated butt-welds is shown in figure 2.17.

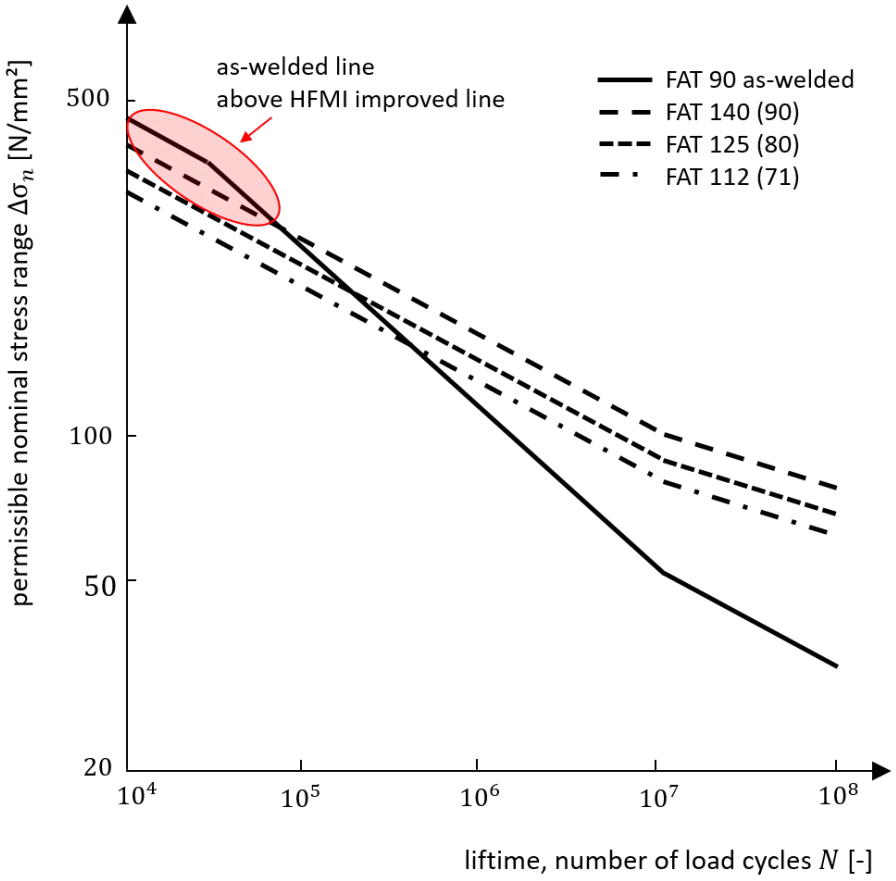

Figure 2.17: S-N curves for butt-welded samples as-welded and HFMI treated [92]

The recommendations for the design of welded structures that are treated with HFMI methods rely on the adjustment of the fatigue class. The fatigue class for a detail will be multiplied by a factor to calculate the higher fatigue class, and is limited by a maximum fatigue class that can be reached by the post-weld treatment. Table 2.1 shows the benefits of different post-weld treatment methods according to IIW [93] and DASt [94] recommendations. On the one hand, it should be noted that these improvements are also dependable on the stress ratio and wall thickness and might meet limitations. Needle and hammer peening, for example, will not have any benefits for a stress ratio $R > 0.4$ [85], and the FAT class is reduced between one and three classes for HFMI treated welds with a stress ratio $R > 0.15$ [92]. On the other hand, it should be noted, that HFMI treatments show especially high lifetime increases for high strength steels [92], potentially even shifting the FAT class to the FAT class of the base material.

As part of this thesis and two papers from 2021 [47] and 2022 [99] an additional post-weld treatment method with Cu/Ni NMM coatings is proposed. Since this method does neither change the geometry, nor change the residual stress in the welded zone,

this post-weld treatment method has to be sorted into a new category of post-weld treatments through high strength coatings, as depicted in figure 2.16 f. The increased lifetime of welded samples that were coated with nanolaminate patches are discussed in chapter 5. Hypotheses on how the mechanisms of the Cu/Ni coating change the fatigue resistance are presented in chapter 6.

Table 2.1: Improvement of FAT classes for nominal stress method of butt-welded joints by different post-weld treatments

Method	FAT improvement factor	Slope of S-N curve m	Max FAT class
Local burr grinding	1.3	3	112
TIG-remelting	1.3	3	112
Hammer and needle peening (mild steel $f_y < 355$MPa)	1.3	3*	112
Hammer and needle peening (steel $f_y \geq 355$MPa)	1.5	3*	125
HFMI treatment (steel $f_y \leq 355$MPa)	1.6	5	140
HFMI treatment (steel $f_y > 355$MPa)	> 1.6**	5	> 160**

$*$ research suggests that $m = 5$ would actually be a better fit for test data [100]
$**$ strongly dependent on the steel strength [92, 100]

Chapter 3

Methods

This chapter contains detailed descriptions of the specimen and specimen preparation (section 3.1), the fatigue testing (section 3.2) as well as the metallurgy preparations for microscopic investigations (section 3.3). The electrodeposition setup and the coating process are described in chapter 4. Further investigation methods, like Atomic Force Microscopy (AFM), are described in chapter 6 as they arise.

3.1 Tensile Test Specimen

Four different kinds of fatigue test specimen are produced and coated with Cu/Ni Nanostructured Metal Multilayer (NMM), as listed in table 3.1.

Table 3.1: Fatigue and tensile test specimens

Specimen	Type	Material	Cross-Section [mm^2]	Length [mm]
Main study	DIN 50125 [101] Type E $t = 8$ mm	Steel S355-J2	200	280
Preliminary study	Comparative [102]	Steel S235	80	135
Small 3D-printed samples	ASTM E466 [103] $r = 2$ mm	Steel 316L (1.4404)	12.57	63
Large 3D-printed samples	ASTM E606 [104] $r = 3$ mm	Steel 316L (1.4404)	28.27	103

For the preliminary study, specimen were cut with a circular saw in parallel stripes from steel plates welded with a double V-grooved butt-weld, akin to the description in section 3.1.1. The study with these samples was published [68] and is presented

in short in chapter 5.1, where the sample geometry is presented in detail (cf. figure 5.1).

Figure 5.19 shows the additive manufactured specimen. The specimens were produced by the *Chair of Metal Structures* of the *Technical University of Munich* and coated at the *Hamburg University of Technology*. As of yet, the larger specimens have not been tested in fatigue and will therefore not be discussed further. The study with the smaller specimen is presented in chapter 5.3.

The dogbone specimen for the main study are cut with a water jet from a steel plate that has a butt-weld in the middle. Figure 3.1 shows the dimensions of the dogbone specimen. The welding process and the quality control for the welds is described in the following sections.

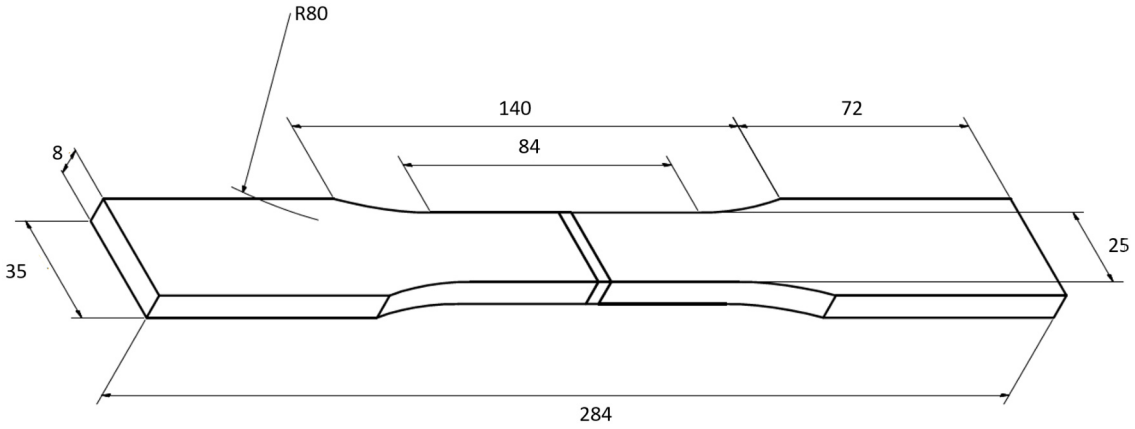

Figure 3.1: Dimensions for a dogbone specimen according to DIN 50125 Type E

Each specimen is marked with an alphanumerical label, containing a letter and a number. The letter gives the steel plate from which the specimen is taken and the number gives the position on the steel plate. The fatigue specimen F10 for example is from the steel plate F and is the 10th specimen cut from the plate.

The actual cross-section area of the dogbone specimen deviates from the nominal $A = 200$ mm^2 by 2.5% to 5%, because of a plate thickness that lies in the range of 7.85 ± 0.1 mm, an actual width of 24.67 ± 0.05 mm and a negligible deviation for the rounded corners. For the remainder of this thesis, the nominal cross-section area is used for all purposes.

3.1.1 Welding

A collaborative welding robot (*Lorch Cobot S5 RoboMIG XT*) is used to join two S355 J2 (EN 10025: 1.0577) steel plates with a double V-goove butt-weld. The steel plates have a dimension of 1000 x 140 x 8 [mm]. Using a welding robot has the advantage of creating reproducible welds with a constant quality. Since a welding robot is used some parameters, like the welding speed, can be defined precisely, while other parameters like the voltage will be determined by internal characteristics of the chosen welding mode.

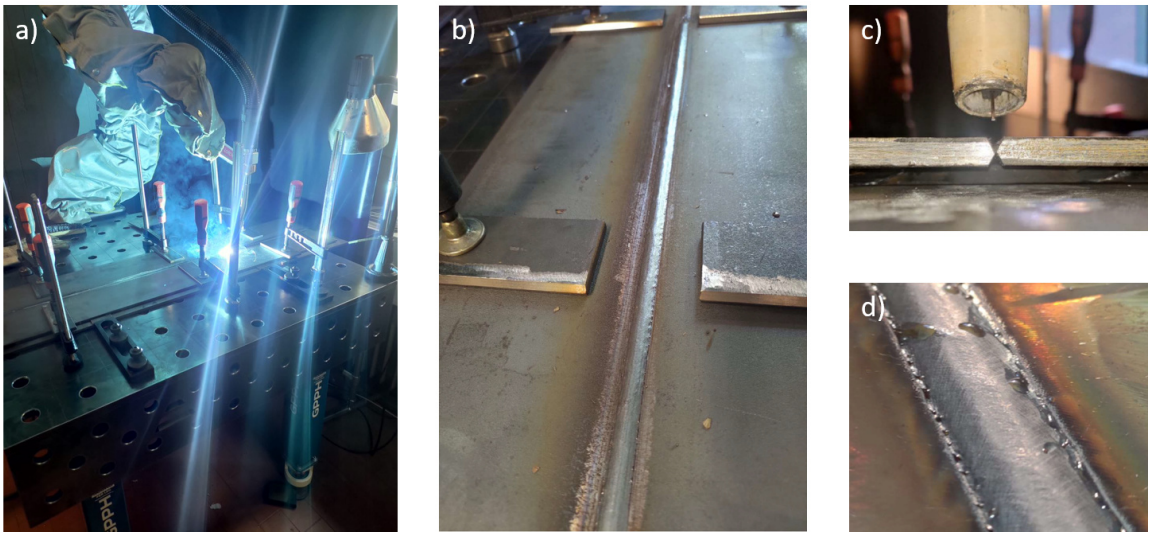

Figure 3.2: Images from the welding process; a) Lorch Cobot welding robot in action; b) finished weld; c) double V-groove before tacking; d) fine scaled weld face

Table 3.2 lists the chemical composition of the steel S355 J2 and the filler material G3Si1 (EN ISO 14341: G42 4 M G3Si1).

Table 3.2: Chemical composition of the steel S355 and the filler material G3Si1

material	C [wt%]	Mn [wt%]	Si [wt%]	P [wt%]	S [wt%]	Cu [wt%]
S355 J2	0.2	1.60	0.55	≤ 0.025	≤ 0.025	0.55
G3Si1	0.1	1.45	0.85	0	0	0

The bevels of the weld are prepared according to DIN EN ISO 9692-1 with an opening angle of 50°. The grooves can be seen in figure 3.2 c).

The two plates are placed with a 2 mm gap and are fastened to the working table and fixated with tack points. The tack points get welded over and are later cut out and discarded. After welding the face side, the back gouge is done with an angle grinder. The root side is then welded from the other side.

The welding parameters are shown in table 3.3.

Table 3.3: Welding parameters

parameter	value	parameter	value
plate		face side weld	
thickness t	8 mm	amps	165 A
material	S355 J2	mode	Speedpulse XT
groove	double V-groove	stick out	9 – 13 mm
filler material		welding speed	7 mm/s
material	G3Si1	root side weld	
diameter	1 mm	amps	210 A
shielding gas	82% Ar	mode	Speedpulse XT
	18% CO_2	stick out	9 – 13 mm
	12 l/min	welding speed	11 mm/s

3.1.2 Quality Control for Welds

The height of the excess weld metal is 1.3 ± 0.1 mm. The width of the weld face is ~ 13 mm. Therefore, most of the welds are categorized into the FAT class 80 and for a few specimens, with the excess weld heights ≤ 1.3 mm, could also be sorted in the FAT class 90 according to DIN EN 1993-1-9 [84]. The weld is inspected visually and no major impairments are visible.

Figure 3.3: Etched micrograph of the weld

The pieces left over from the water cutting are taken for the creation of cross-sections, that are ground and polished, as well as swab etched to make the internal structure of

the welds visible. Figure 3.3 shows an etched micrograph of the weld. The different areas of the weld can be clearly distinguished. The black diamonds on the bottom of the weld are imprints left from hardness testing. The hardness values are as to be expected between $\sim$ 180 HV10 in the base material and $\sim$ 250 HV10 in the Heat Affected Zone (HAZ).

The first welds produced had some problems with lack of root fusion (Reference No. 4013 according to DIN EN ISO 6520-1 [105]) that could be seen clearly from the cross-sections, and this problem could be addressed before the first batches of fatigue specimen were welded. The batches A to F have an internal error that could not be seen from the outside and did not show on the polished and etched cross-sections. A linear oxide inclusion (Reference No. 3031 according to DIN EN ISO 6520-1 [105]) can be found in the corresponding welds. For batch G, the welding parameters for the root side weld have been adjusted to eradicate this error and a destructive fracture tests has been added to the quality control.

Except for the internal error, the welds have the desired quality and a uniform and smooth weld face, as can be seen from figure 3.2 b) and d).

3.2 Fatigue and Tensile Testing

Both fatigue and tensile testing are performed with a servo-hydraulic uni-axial testing machine (Schenck 250 PSB). Fatigue tests are performed and evaluated according to DIN 50100 [102] and recommendations of DVS notice 2403 [106]. Tensile tests are performed according to DIN EN ISO 6892-1 [107]. The results of the tensile and fatigue testing are presented in chapter 5.

Monotone Testing

Monotone tensile tests are performed at a constant strain rate of 0.1 mm/s until fracture. Force and displacement curves are saved digitally. The yield strength F_y is measured at the kink of the force displacement curve, and the ultimate strength F_u is measured at the highest point of the curve. Stress strain curves are calculated with the nominal cross-section area A and the gauge length L_0. The final elongation of the samples is taken by measuring the length of the sample before and after fracture. An extensometer is not used.

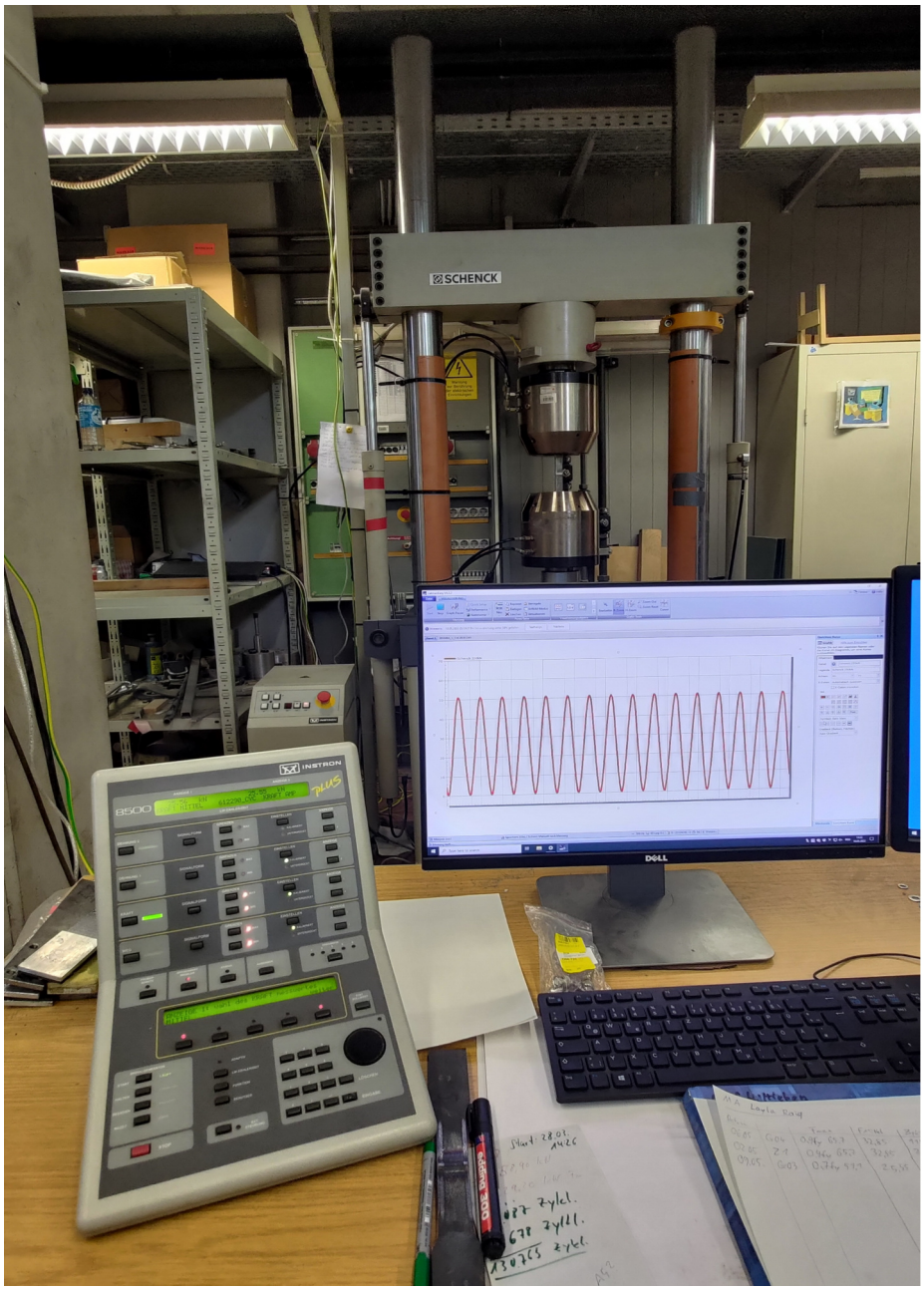

Figure 3.4: Servo-hydraulic test machine

Fatigue Testing

The sinusoidal fatigue load is entered with a static mean force F_m and the amplitude F_a. All tests in the main study of this thesis are run with a fatigue stress ratio $R = 0$, meaning that $F_{min} = 0$ and $F_{max} = 2 \cdot F_a$. Peak control is used to avoid overshooting the desired maximum and minimum force F_{max} and F_{min}. All fatigue tests are run at 8 Hz, to avoid natural frequencies in the test setup, which have been observed somewhere around 10 Hz. The samples are tested until fracture or until a limit of

$N = 2.5 \cdot 10^6$ cycles is reached, at which point the sample is considered a run-out. The force and displacement curves are tracked with a computer setup, but for the fatigue testing only the number of fatigue cycles is recorded to conserve memory space.

Fatigue Data Evaluation

The calculation of S-N curves is based on a linear regression model (German: *Perlenschnurverfahren*) from the DIN 50100 [102].

The S-N curve is described by fitting the constants of the double logarithmic line, as described by the Basquin equation 3.1, with C and k being constants that can be calculated from equations 3.2 and 3.3. The stress range $\Delta\sigma_i$ and the number of cycles N_i are the results from fatigue testing, n is the number of samples.

$$\log N = \log C - k \cdot \log \Delta\sigma \tag{3.1}$$

$$k = -\frac{n \cdot \sum (\log \Delta\sigma_i \cdot \log N_i) - \sum(\log \Delta\sigma_i) \cdot \sum(\log N_i)}{n \cdot \sum(\log \Delta\sigma_i)^2 - (\sum(\log \Delta\sigma_i))^2} \tag{3.2}$$

$$C = \frac{1}{n} \cdot \left(\sum \log(N_i) + k \cdot \sum(\log \Delta\sigma_i) \right) \tag{3.3}$$

The highest and lowest point of the SN-curve is given by inserting $\Delta\sigma_{min}$ and $\Delta\sigma_{max}$ of the data set into equation 3.1, with the corresponding k and C.

For statistical analysis of the data, like the calculation of the 95th percentile, all data points are shifted to a fictional load horizon according to equation 3.4. The fictional load horizon is set at 300 MPa.

$$\log N_{i,fictional} = N_i \cdot \left(\frac{\Delta\sigma_f}{\Delta\sigma_i} \right)^{-k} \tag{3.4}$$

The fictional mean and standard deviation are calculated with equations 3.5 and 3.6.

$$\log \overline{N_f} = \frac{1}{n} \sum \log N_{i,f} \tag{3.5}$$

$$s_{fictional} = \sqrt{\frac{1}{n-2} \cdot \sum (\log N_{i,f} - \log \overline{N_f})^2} \tag{3.6}$$

A correctional factor for the standard deviation is used for small sample sizes $n < 10$ because the standard deviation will be underestimated due to asymptotic unbiasedness. The corrected standard deviation is calculated with equation 3.7.

$$s_{f,corr} = s_f \cdot \frac{n - 1.74}{n - 2} \tag{3.7}$$

A benchmark for scatter (German: *Streuspanne*) T_N is calculated with equation 3.8

$$T_N = 10^{2.564 \cdot s_{f,corr}} \tag{3.8}$$

The 10th percentile and 90th percentile are calculated by equation 3.9. The SN-curves for different percentiles are shifted parallel to the mean curve with the given upper and lower bounds for the load level, as described above.

$$N_{10\%,90\%} = 10^{\log \overline{N_f} \pm 1.282 \cdot s_{f,corr}} \tag{3.9}$$

Additionally, the 5th percentile is calculated with equation 3.10 for comparison with the SN-curves from Eurocode 3, which gives the FAT classes as 5th percentiles with a replication level of at least 75% [84].

$$N_{5\%} = 10^{\log \overline{N_f} - 1.96 \cdot s_{f,corr}} \tag{3.10}$$

For this method, the estimation of k is strongly dependent on the difference between the upper load level σ_1 and the lower load level σ_2, as well as the number of samples

n [102]. Especially for the data sets with a low amount of load specimens, taking the estimated k the best fit line will not necessarily yield better results in comparison to the population. Therefore, the calculations are repeated with fixed values of k taken from literature.

3.3 Metallurgy and Sample Preparation

To characterize the used metals, different methods of metallurgy were used to look at the different scale magnitudes. Cross-sections of the welded fatigue samples as well as the nanolaminate structure were produced, ground down and polished by conventional metallurgical sample preparation for microscopy and Scanning Electron Microscopy (SEM) investigations, as described in the following paragraphs. Furthermore, cross-sections for SEM and Transmission Electron Microscopy (TEM) were produced using Focused Ion Beam (FIB) milling and FIB serial cross sectioning methods as described in section 3.4.2.

Sample preparation methods have been developed based on experience and recommendations from [108].

Sectioning

Metallurgical cross-sections of the welded specimen are cut from the sample with a circular saw or band saw from the welded metal plate. A lubrication system cools down both the saw and the sample to protect the sample from any heat influences, which might occur during cutting.

Alternatively, wire electrical discharge machining is used for cutting smaller samples coated with a NMM to reduce the influence from cutting on the material.

Sample Mounting

A 30 mm silicone mold is used to embed the cut samples for grinding and polishing. Different cold mounting materials have been tested and used with different results. Table 3.4 lists the different mounting materials, including advantages and disadvantages.

Using the methacrylate mounting system for hard materials yielded the best results, especially for examinations at the edge of the sample, due to the similar hardness and the low shrinkage. The methylmethacrylate had the worst performance for edge

examinations, because of gaps that formed while hardening and during the grinding and polishing process.

A hot mounting process was not used in this work to avoid temperature influences on the samples from the mounting process.

Table 3.4: Cold mounting materials

mounting material	product name	advantages	disadvantages
methacrylate	KEM 15 plus	short hardening time high hardness low shrinkage	short processing time non-transparent non-conductive
methylmethacrylate	Technovit 5000	short hardening time conductive	short processing time non-transparent high shrinkage pores poor processability
epoxy resin	KEM 92	long processing time high hardness transparent good processability	long hardening time small pores non-conductive

Grinding and Polishing

An automated grinding and polishing machine (*QATM Qpol 250 A1-Eco*), as depicted in figure 3.5, is used to produce repeatable sample preparation results. The machine is outfitted with a liquid dosing unit (*QATM Qdoser Eco*) for automatically adding polishing lubricants and diamond suspensions. For low deformation fine polishing, a vibration polishing machine (*QATM Saphir Vibro*) is used as the last polishing step.

Samples are rinsed with water between polishing steps. After the last polishing step, the sample is rinsed with ethanol and dried with an air dryer. The samples are inspected visually for scratches, first with the bare eye, later with the microscope. If necessary, grinding and polishing steps are repeated.

For the samples that contain a NMM coating, the polishing process is more difficult since the different materials at the edge of the sample behave differently and the grinding and polishing might damage the edges of the sample. Additionally, copper will be smeared across the surface by the grinding and polishing processes, which obscures the nanolaminate structure. Therefore, the process is ended with a low deformation polishing step as described in table 3.6 and an etching step to get rid of the thin copper layer.

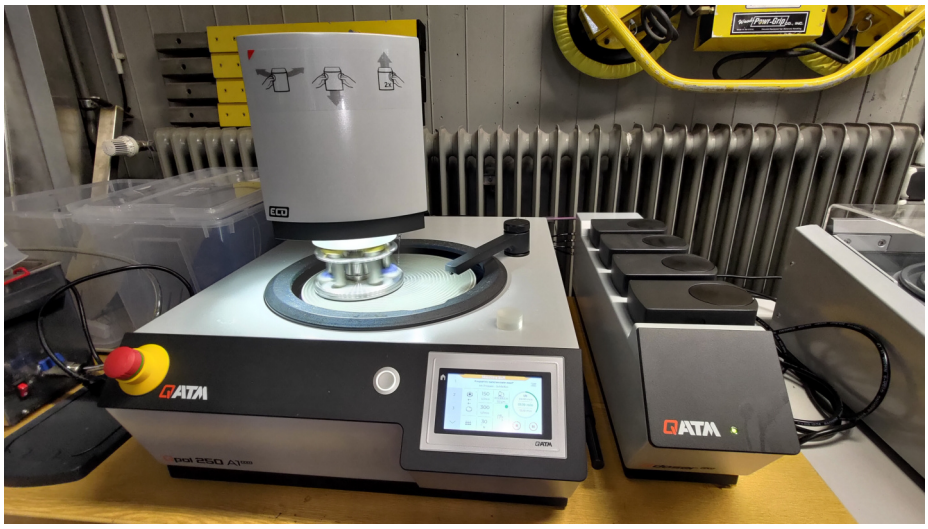

Figure 3.5: Grinding and polishing machine used for metallurgical sample preparation

Table 3.5: Grinding and polishing steps

grinding disc/ polishing cloth	lubricant	wheel speed [rpm]	head speed [rpm]	head rotation*	pressure [N]	time [min]
Polaris H 125 μm	water	300	150	cc.	30	2 : 00
Polaris H 60 μm	water	300	150	cc.	25	1 : 00
Polaris M 15 μm	water	300	150	c.	25	3 : 00
Polaris M 3 μm	water	300	150	c.	15	6 : 00
Galaxy Zeta dia pol 3 μm	blue**	300	150	cc.	15	6 : 00
Galaxy Zeta dia pol 1 μm	blue**	300	150	c.	15	6 : 00

*c. – clockwise, cc. – counter-clockwise; **alcohol-based lubricant

Table 3.6: Additional vibro polishing step

polishing cloth	polishing suspension	frequency [Hz]	time [h]
Galaxy Omega	Eposil M 0.06 μm	$\sim$ 90	4:00

Etching

The welded steel samples have been immersion-etched for 20 s to a few minutes using the etching reagent according to Adler. This produces good macroscopic images of the welded area. Alternatively, Nital (95% ethanol 5% nitric acid) is used for swab etching to produce the macrostructure of the welded specimen. Both etching processes yield good results for microscopy. A finished weld sample can be seen in figure 3.6 b).

As described above, a thin copper layer will be smeared across the surface by the

grinding and polishing steps for the coated samples. The samples with Cu/Ni nanolaminate are etched with a 10% ferric nitrate solution for a few seconds to a few minutes. Since the copper etching process yields results of vastly different quality, FIB-milling (see section 3.4.2) is the preferred process for SEM investigations of the NMM-coating.

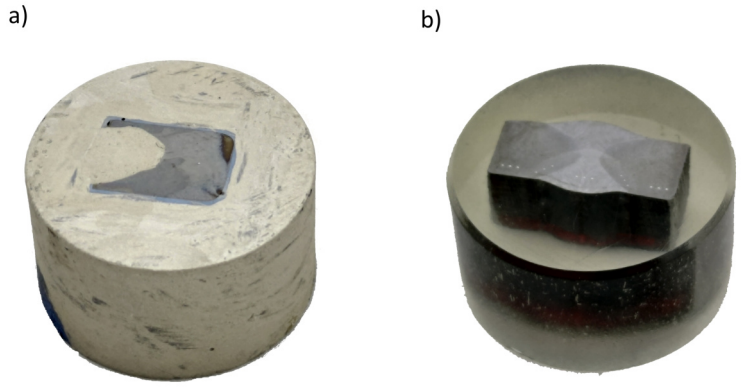

Figure 3.6: Cold mounted metallurgical steel specimens; a) SEM cross-section examination; b) hardness testing and microscopy

SEM Preparation

For SEM samples, additional steps have to be taken to ensure the conductivity of the samples. Even the samples that were embedded in the conductive methylmethacrylate need this step to produce good SEM image quality, especially at the edges. The samples are coated with a thin layer of silver conductive paint and cured over a 12 – 24-hour period. A finished sample for SEM-investigations can be seen in figure 3.6 a). Further information on SEM preparation and imaging is given in the following sections.

3.4 SEM, TEM and EDX Imaging

Scanning Electron Microscopy images are created with a *Leo Gemini 1530*. Alternatively, SEM images are created with a FIB cross-sectioning method (using the *FEI Helios NanoLAB G3*) in cooperation with the *electron microscopy unit* (*BEEM*) by cutting into the coating with an ion beam and looking from an angle at the exposed cross-section. For very high-resolution images, which resolve the layers and grains in

the nanolaminate, scans are taken with a TEM *FEI Talos F200x* by the *BEEM* unit. Figure 3.7 shows one of the tension-tension fatigue samples mounted to the xyz-stage of the FEI Helios.

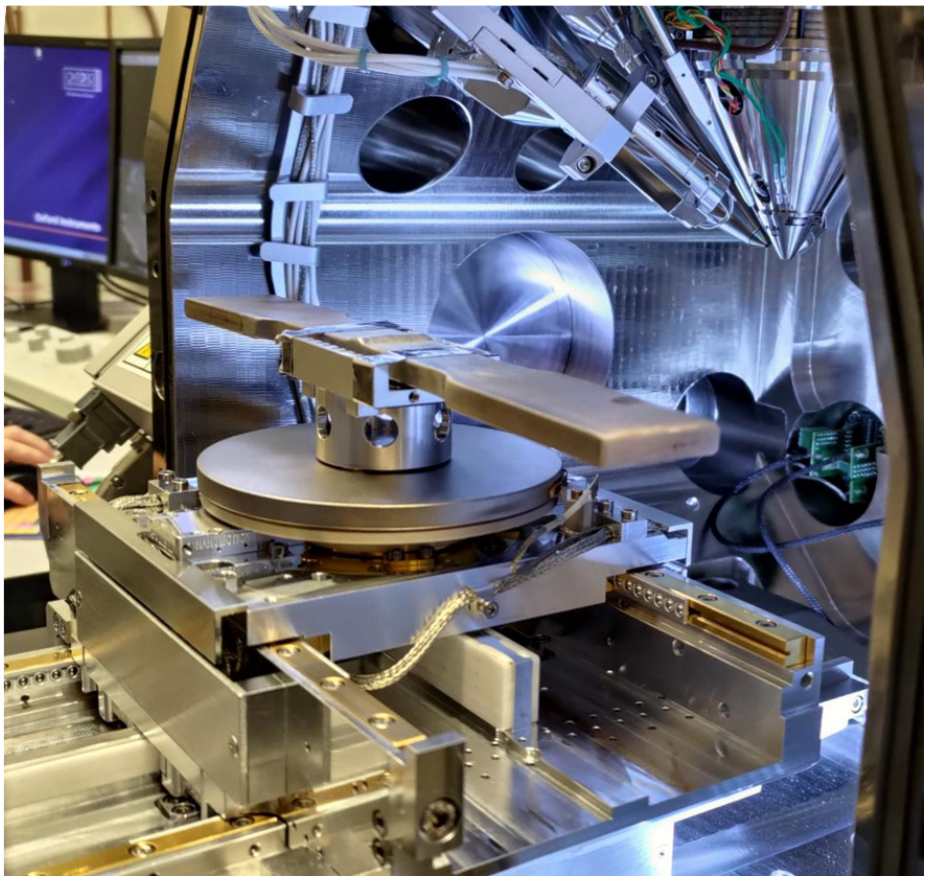

Figure 3.7: Full tension-tension fatigue sample mounted in a FEI Helios NanoLab G3 (DualBeam) FIB

3.4.1 SEM Images

As described above, the SEM sample preparation leaves a thin copper layer on top of the cross-section. To make the underlying structure visible, a high acceleration voltage of 15 kV is used to look through the copper layer. Unfortunately, high acceleration voltages will decrease the focus of the beam, making small details blurry. Since the coating is on the edges of the specimen, the mounting material will be charged up, which comes with additional focus problems for SEM imaging. Therefore, the more time consuming and costly variant of FIB cross-section preparation is used preferably in this work. SEM images with the Focused Ion Beam microscope are taken with the TLD/SE sensor at 2 kV and 50 pA.

3.4.2 FIB Milling, Serial Cross-Sectioning and TEM Lamella Preparation

Preparing for investigations of cracks in the coating surface, a polymer is diffused into the cracks in order to make FIB cutting possible.

For FIB cross sectioning, the surface is coated with a 2 μm Pt layer. A milling trench pattern is used to cut $\sim$ 25 μm into the surface with an 9.3 nA ion beam and expose the cross-section of the coating. The cross-section is polished with an 0.79 nA ion beam. This process is automated to create a serial cross-sectioning of one of the cracks that stemmed from fatigue testing. A TEM lamella is taken from the crack tip to investigate the failure mechanisms (cf. chapter 6). Figure 3.8 shows the crack from above with a trench that shows the cross-section and selected images from serial cross-sectioning.

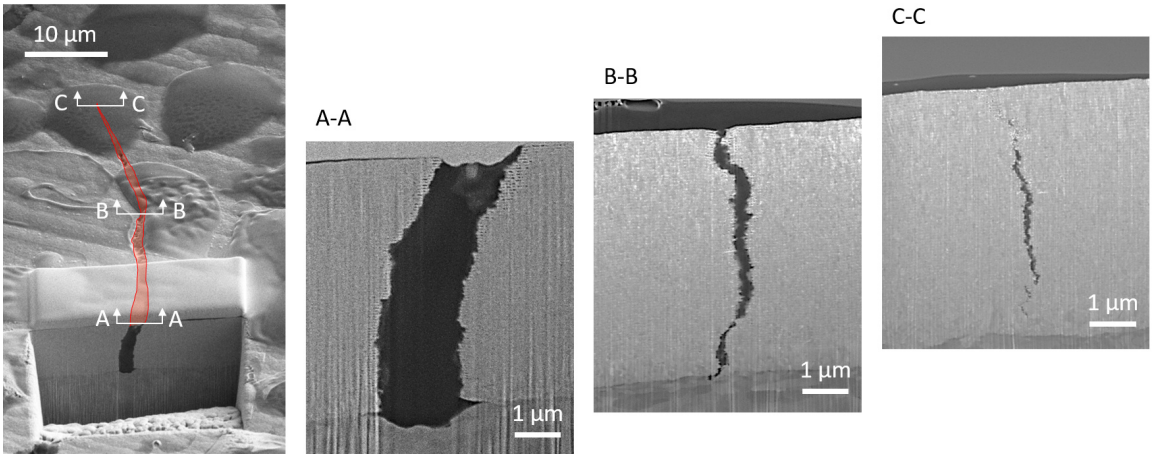

Figure 3.8: FIB serial cross-sectioning along a crack in the NMM coating, with the crack highlighted in red on the surface

The TEM lamella is produced by cutting into the surface, as described above. The trenches are dug and polished from both sides, leaving a 2 μm thick lamella standing. For the pre-thinning of the lamella, an 0.79 nA ion beam is used and the lamella is tilted by $\pm$ 2°. The lamella is then joined by redeposition milling to the lift-out needle, and a U-cut is used to cut the lamella from the rest of the material. The lamella is lifted out and placed on a TEM grid holder and joined to the holder by depositing a 3x3x1 μm platinum patch on both sides. Afterward, the lamella is cut free from the needle. The lift out process and a TEM lamella can be seen in figure 3.9 To make the lamella electron-translucent, the lamella is thinned to $\sim$ 100 nm and polished with an 80 pA ion beam.

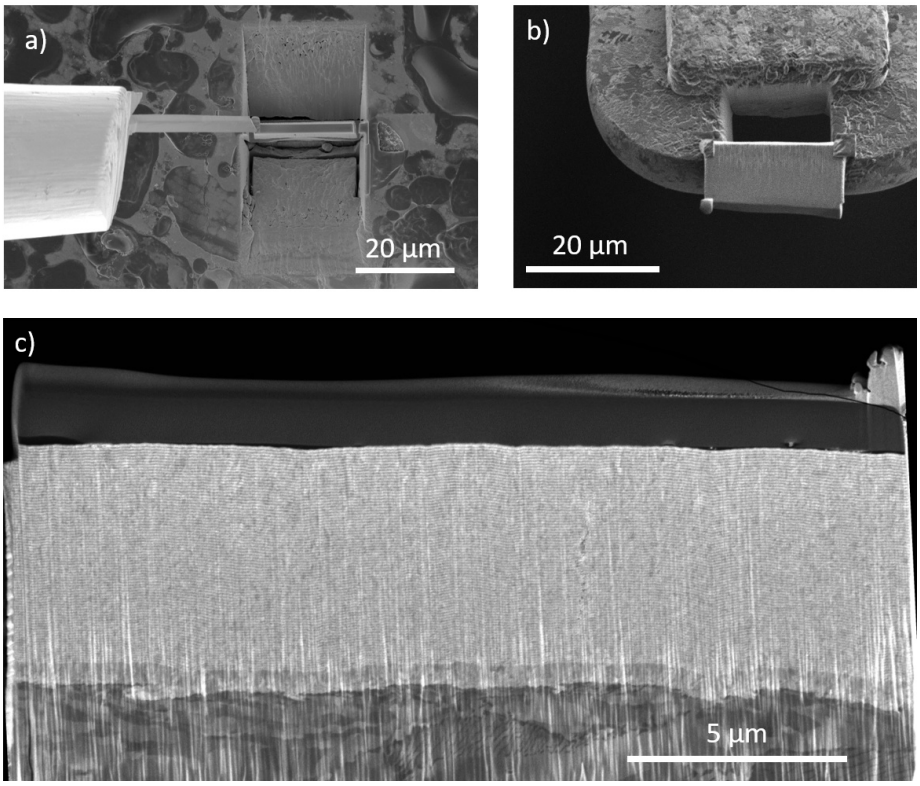

Figure 3.9: Lift-out process of a TEM lamella; a) freestanding lamella from above with the lift-out needle coming in from the left; b) TEM lamella transferred to the grid; c) SEM image of pre-thinned lamella

Because of strong curtaining effects, the protective layer height should be increased and, if necessary, an additional carbon protective layer added below the Pt layer.

TEM images are taken with the High-Angle Annular Dark Field (HAADF) up to a magnification of $125,000$x. Energy-dispersive X-ray Spectroscopy analysis has been performed simultaneously, with the same detector, to clearly distinguish between the Cu and Ni layers at the interfaces.

The preparation of the TEM lamella is described in section 3.4.2. The TEM images are substantial for material characterization and in the understanding of the failure mechanisms as described in chapter 6.

Chapter 4

Electrodeposition of Nanolaminate Patches on Steel Specimen

This chapter presents the electrodeposition setup in section 4.1 and the electrodeposition process with the affiliated process parameters in section 4.2. Section 4.3 evaluates and discusses the coating quality for the specimen.

4.1 Electrodeposition Setup

For the coating of specimens with a Nanostructured Metal Multilayer (NMM), a single bath technique is used. Figure 4.1 shows the electrodeposition setup from two different angles.

A bath with the dimensions of 30 cm x 15 cm x 10 cm is used. The cathode is placed on an additive manufactured PP holder in the middle of the bath. Eight anodes, four Cu anodes and four Ni anodes, are placed in a checkerboard pattern around the cathode at the wall of the bath with a distance of $4 - 5$ cm. The anodes are placed inside PP filter bags to increase the coating quality. The electrolyte is filled into the bath to a height that the cathode has the same amount of wetted anodes above and below the cathode. This is important for the uniform current density distribution. The bath is covered with foil or a lid to avoid evaporation of the bath. A magnet stirrer agitates the bath with a magnet fish.

The anodes and cathodes are connected to the pulsed power supply (*Plating Electronics pe86CB-20-5-25-SGD*) with banana contact cables and the power supply is connected to a computer via a RS485 link and can be controlled with the plating electronics software.

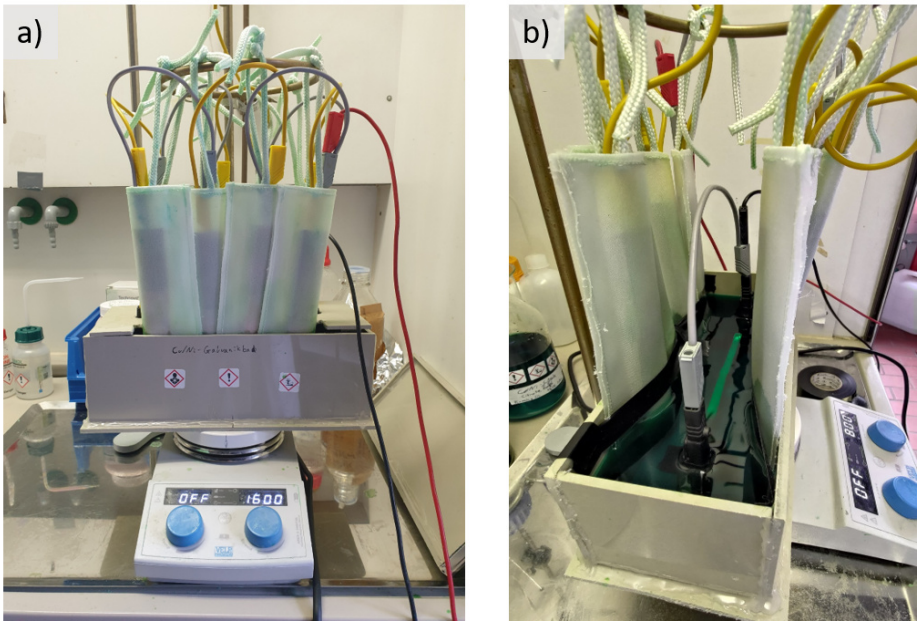

Figure 4.1: Electrodeposition setup; a) from the front; b) looking into the bath

Single Bath Electrolyte

The electrolyte is a citrate Cu/Ni sulfate bath according to the recipe of *Bonhôte and Landolt* [109]. According to the paper, the deposition of Cu/Ni NMM from a citrate bath instead of a sulfamate or cyanide bath yields fine grained and smooth laminates.

The polarization curve in figure 4.2 shows the current density over the potential applied to the electrodeposition reaction. The current densities used for deposition are marked. The zoomed in curve shows the start of the Cu deposition at low current densities.

The electrolyte has been prepared by the *Hamburg University of Technology Central Research Labs*.

The bath is monitored by measuring the pH value and taking samples that are analyzed by the *Hamburg University of Technology Central Research Labs*. The measurements show that the electrolyte is stable, but after ~ 50 h of use the bath deteriorates and needs to be replaced. The coating quality is getting worse at that point. Unfortunately, the reasons for the deterioration could not be determined and is not visible in the easily available pH values. Chapter 7 presents possibilities to follow up on this.

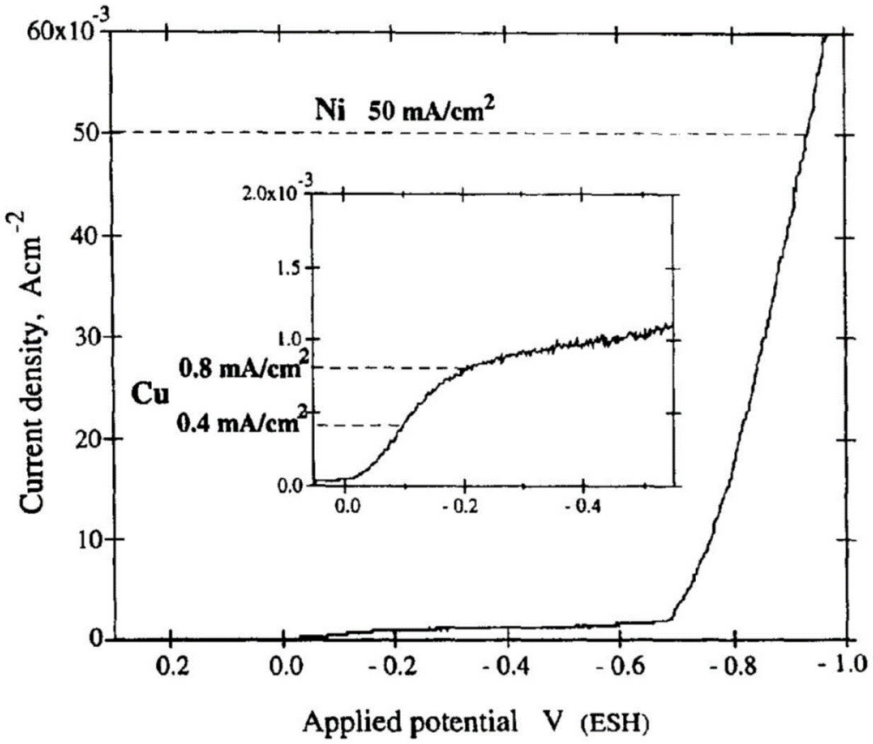

Figure 4.2: Polarization curve for a citrate Cu/Ni sulfate bath with the current densities for the electrodeposition of Cu and Ni [109]

4.2 Coating Process

The electrodeposition process is quite complex and especially the bath quality, the local current density and the surface preparation have a considerable influence on the final coating quality [69].

A multi-physics simulation is used to determine the local current density along the surface of the specimen. Hull cell tests are used to determine the ranges in which a good coating quality is obtained.

The coating process is iteratively improved, based on literature recommendations [71, 69, 72] and results from coatings and simulations. While the exact process will not be discussed herein, the iterative increase in surface quality can be seen in figure 4.3.

From these investigations, the cathodic current efficiency could be calculated by matching the deposited layer thickness to the theoretical deposition thickness calculated by equation 2.1.

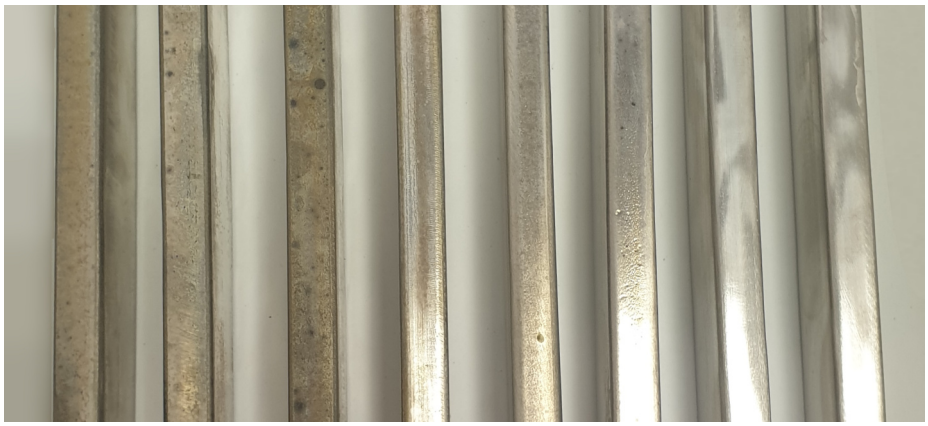

Figure 4.3: Improvement in coating quality over the iterative optimization

Current Density

The electrodeposition process is tested with hull cell tests according to DIN 50957-1 [110] to gain the upper and lower bounds for the current density i for both the copper and nickel deposition process. Figure 4.4 exemplarily shows a hull cell plate with a nickel deposition, showing the upper limit for current density. The results of the current density limits can be seen in table 4.1.

The resulting current density limits are in well accordance with the specifications by *Bonhôte et al.*, who use a current density between 0.40 mA/cm^2 and 0.80 mA/cm^2 for Cu deposition and a current density of 50 mA/cm^2 for Ni deposition [109].

Table 4.1: Current density limits for the deposition of Cu and Ni from the single bath electrolyte

deposited metal	i_{min} [mA/cm^2]	i_{max} [mA/cm^2]
Cu	0.20	0.84
Ni	N/A	50.00

From these results and perfunctory current density simulation results, the maximum current density for Ni is reduced to 40 mA/cm^2.

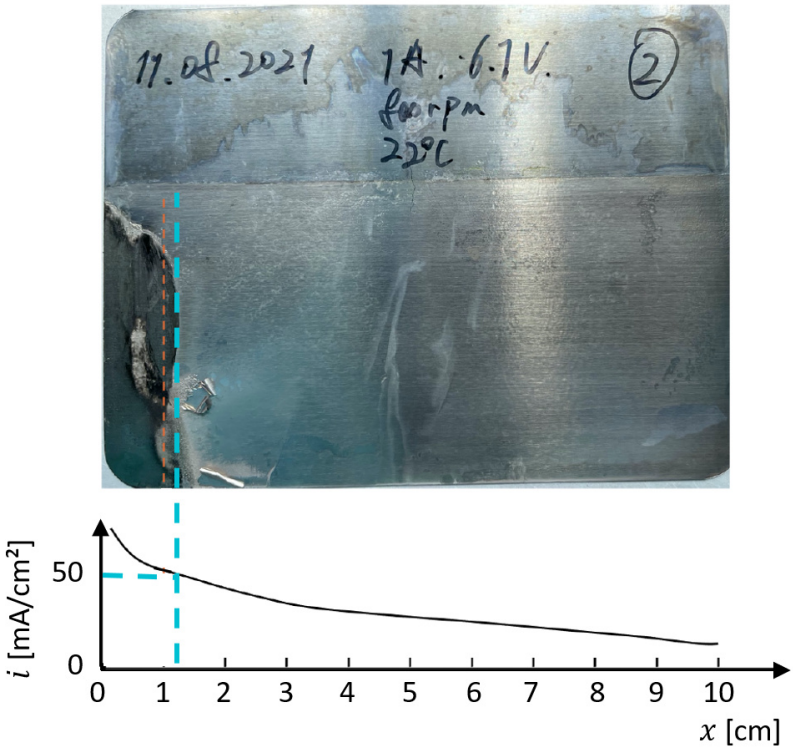

Figure 4.4: Steel hull cell plate coated with a Ni layer at room temperature with the current density diagram and the marked upper deposition limit

Specimen Preparation and Cleaning

Good electrodeposition practice needs a clean surface and no sharp edges [69]. Since the fatigue samples also need rounded edges [106], this does not need an alteration of the specimen. The mill and welding scale needs to be removed and the surface needs to be cleaned from grease and oxides.

The process has been tweaked over time, and the following process description presents the parameters that are used for all dogbone specimen that are coated with Cu/Ni NMM and are classified as satisfactory. Since the quality of coatings is still varying, the process might need further refinement in the future.

Scale Removal

The as-welded specimens are freed from the mill scale by grinding the surface with an angle grinder in the flat areas and a fan grinder around the weld to keep the geometry of the original weld. A burr grinder is used to get rid of any remaining weld scale at the weld toe.

The difference between the as-welded specimen and the specimens that are machined at the surface can be seen in chapter 5 in figure 5.3.

These specimens are also tested in fatigue to rule out that any improvement in lifetime is coming from the preparation process, as will be discussed in chapter 5.2.

For practical purposes, this process should be replaced with a sand blasting process in the future (cf. chapter 7).

Degreasing and Deoxidation

For deoxidation and degreasing, an ultrasonic cleaner (*EMAG Emmi-H120*) is used.

Preparing for the electrodeposition process, the specimens with the machined surface are cleaned for 10 min in a 2.5% EMAG EM-600 solution. The specimens are then rinsed with distilled water, and the specimens should be handled with care to avoid further surface contamination. This is followed by a deoxidation step for 4 min in a 5% EMAG EM-202 solution. The EM-202 cleaner is a phosphate acid-based intensive cleaner for the removal of metal oxides and silicates. If this step is too short, oxides remain on the surface, which will lead to adhesion problems with the coated nanolaminate. If this step is too long, the surface will become over-etched and dull, which in turn will lead to problems with surface activation in the electrodeposition process. The specimens are then rinsed with distilled water and the electrodeposition process should be started shortly after to keep the specimen from oxidation and new surface contamination. A continuing activation step is not applied.

NMM Lay-Up

The chosen NMM lay-up consists of an overall thickness of $9,000$ nm, a Ni base layer of $1,000$ nm, a bilayer thickness of $\Lambda = 50$ nm, and Cu and Ni single layer thicknesses of 15 nm and 35 nm respectively.

This lay-up is arbitrary and was chosen because of good experiences from the preliminary study and the study with additive manufactured specimens as discussed in chapter 5.

Deposition Parameters

From the limits given above and the specimen surface area $A = 223$ cm^2, the current for the calculation process is determined. Because of restrictions from the power sup-

ply, the Cu current density is slightly increased from the recommended 0.4 mA/cm^2 to $\sim$ 0.45 mA/cm^2 and the Ni current density is reduced from 40 mA/cm^2 to $\sim$ 22 mA/cm^2. The deposition times are then calculated from equation 2.1. Between the deposition phases, a 1 s break is added. From this, the deposition parameters in table 4.2 are derived.

Table 4.2: Electrodeposition parameters for the deposition of a 9,000 nm Cu/Ni NMM from a citrate bath

parameter			value	
specimen surface		A		223 cm^2
current density Ni deposition		i_{Ni}		22 mA/cm^2
current density Cu deposition		i_{Cu}		0.45 mA/cm^2
Ni base layer deposition	$I_{Ni,base}$	$t_{Ni,base}$	5,000 mA	150 s
Cu layer deposition	I_{Cu}	t_{Cu}	100 mA	107 s
Ni layer deposition	I_{Ni}	t_{Ni}	5,000 mA	5 s
pause		t_{pause}		1 s
total deposition time		t_{tot}		5 : 07 h
temperature		T		$20 - 25$ ° C
agitation		f_{rot}		1,500 rpm

Electrodeposition Waveforms

The waveforms for the Ni base layer deposition and the Cu and Ni layer depositions are generated according to table 4.2 with the *Electroplating Waveform Generator* and the *Electroplating Batch Generator*. A text editor is used to expand the created batch to include the full five-hour deposition process.

4.3 Discussion of the Electrodeposition Process

This section shortly summarizes the methods for quality control used to categorize the coatings, gives common problems and solutions that occur during the plating process, lists common coating quality impairments and finally summarizes the quality of all coated dogbone specimens.

4.3.1 Methods for Quality Control

The following methods are used to measure the quality of the coated dogbone specimen:

Visual Inspection

All specimens are evaluated by visually inspecting the surface. Delamination, Ni burns, discoloration, and surface roughness are marked down. Almost all samples experience some kind of quality restraint. Especially, the Ni burns and following delamination are often at the edges of specimens and do not impair the weld area. The different problems that occur are discussed further below.

Adhesion Testing

Adhesion is tested by cutting a 9 by 9 grid into the surface [69]. This is a simple qualitative test. Specimen with good adhesion quality experience almost no damage from cutting into the surface, partly attributed to the high wear resistance of Cu/Ni NMM. For specimens with a mediocre adhesion, the coating can be scratched more easily and can be loosened in small flakes. For specimens with bad adhesion, which is not already obvious from visual testing, the coating can be scratched and then breaks off in large flakes.

For some specimens, delamination occurred after plastic deformations of the base material without the adhesion testing showing any signs of flaking.

SEM Cross-Section Evaluation

Because the NMM lay-up cannot be seen from the outside, some coatings are evaluated by Scanning Electron Microscopy (SEM) cross-section analysis, as described in chapter 3.3. Only a limited number of specimens have been evaluated this way.

Especially at the beginning, coatings are tested to validate the Cu/Ni nanolaminate lay-up. Additional Transmission Electron Microscopy (TEM) lamella were produced from fatigue tested specimens to assess the damage mechanisms in the NMM coatings.

4.3.2 Problems with Electroplating

Different problems occur during the electrodeposition process. Some of these problems are presented and discussed here.

Figure 4.5 shows the edge of four different specimens with different coating qualities and quality impairments.

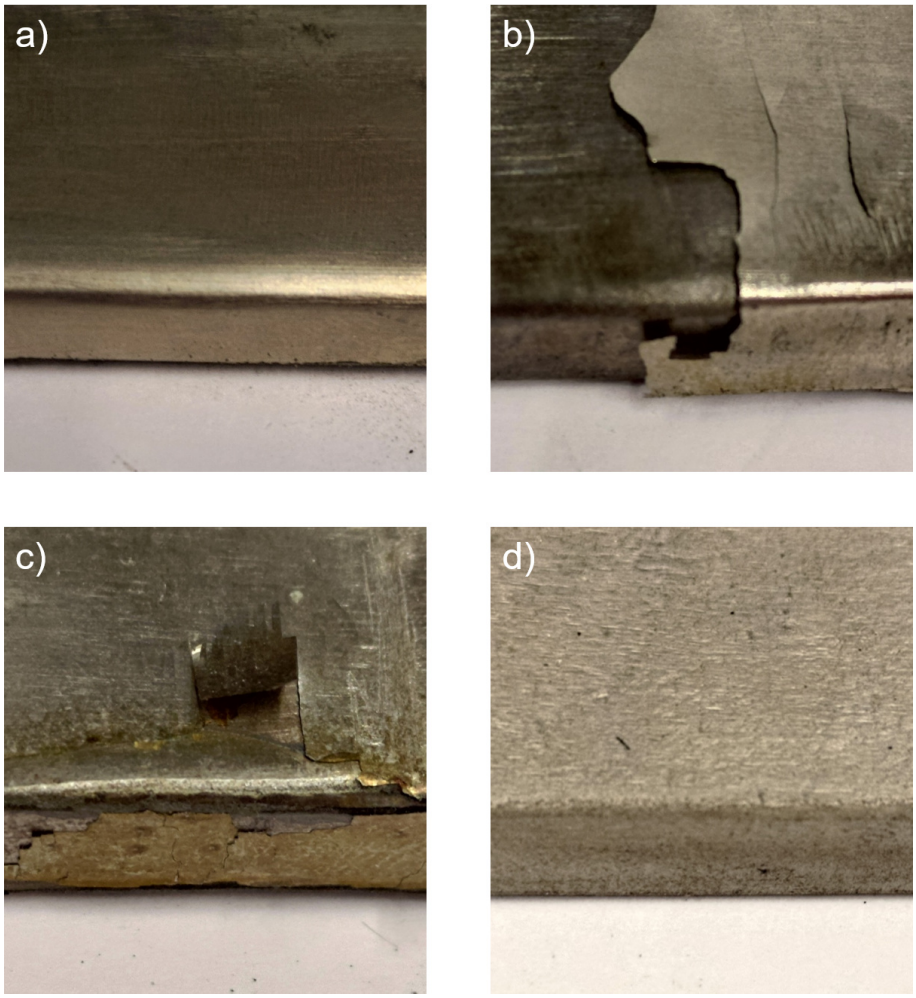

Figure 4.5: Coating quality examples: a) good coating of specimen G17; b) large-scale delamination of specimen G33; c) Ni burns and subsequent delamination of specimen B11; d) rough coating of specimen E11

Software Instability

In two cases, the software showed an instability and the coating process got stuck on a Cu deposition waveform. The problem was not reproducible. While the exact reason for the instability is unknown, it appears that the communication between the software and the pulsed power supply is at fault.

Delamination

Delamination, as seen in figure 4.5 b), often occurs in areas, where the surface preparation was insufficient. Thin oxide layers or organic films between the substrate and the Ni base layer will reduce the adhesion because no metal bond is formed between the Ni layer and the steel substrate.

Another reason for delamination could be residual stress differences between the substrate and the coating that surpasses the adhesion strength.

Furthermore, delamination occurs in areas with Ni burns, or in areas where a thin Cu layer has deposited by copper iron surface exchange or electroless deposition, as described in the following sections.

Copper Iron Surface Exchange

The electronegativity of Cu will start an exchange process on the steel surface as soon as a specimen is submerged into the electrolyte. Cu atoms are swapped with Fe atoms according to the simplified reaction equation 4.1 [111].

$$\mathrm{Cu}^{2+}_{(aq)} + \mathrm{Fe}_{(s)} \longrightarrow \mathrm{Cu}_{(s)} + \mathrm{Fe}^{2+}_{(aq)} \tag{4.1}$$

It is well known that this process will lead to adhesion problems that can be stopped with Ni base layers. A Ni base layer thickness of a few micrometers is recommended for the Cu plating of steel substrates. Because of the low Cu content in the single bath electrolyte, starting the Ni base layer deposition process within the first minute of submersion of the specimen shows a good adhesion quality in the end.

This problem can be avoided entirely, if the Ni base layer is deposited from a pure Ni electrolyte before submerging the sample into the single bath electrolyte.

Electroless deposition of Cu is also happening on the Ni layers. Therefore, the speci-

mens have to be removed relatively fast from the electrolyte after the last Ni layer is deposited.

Ni Burning

Areas with current densities above the deposition limit will produce a darkened and flaky coating. This is most often described as *burned* areas in the literature.

The solution to this was rounding the corners, reducing the current for the deposition process and increasing the agitation rate. Since the PP-container is not suitable to be heated on the heating plate of the magnetic stirrer, this has not been tried.

As shown in figure 4.5 c), Ni burns still occur with some specimens.

Rough or Dull Surfaces

A rough surface can most likely be traced back to inclusions of sulfate particles into the coating. Dependent on severity, this might be a visual problem only or a problem that disrupts the nanolaminate lay-up. Figure 4.5 d) shows an example of a rough surface. Keeping the anode bags clean and filtering the electrolyte occasionally, will keep the electrolyte free from contamination.

A second mechanism for roughening is the creation of small pits on the surface from areas where hydrogen gas is forming on the surface. Hydrogen embrittlement of the substrate does not seem to be a problem, since this effect has not been observed and the Ni and Cu layers act as barriers for the hydrogen absorption [112].

4.3.3 Quality of the Coated Specimens

The quality of the coated samples is listed in table 4.3. All specimens that have been coated are controlled visually.

For the overall quality, coatings are qualified as *good*, *okay*, or *bad*. Specimens that are rated *good* do not have any of the described visual impairments. Specimens rated *ok* do have at least one of the described electroplating problems only locally and not around the expected crack initiation site at the weld toe. Specimens rated *bad* do either have large area quality issues or problems at the weld toe.

For the specimens G42 and B11, the deposition process was interrupted by a software instability, as described above. This changes the coating lay-up for the two specimens,

as the predefined electrodeposition process was altered by the interruptions. The coating process was resumed in both cases and while there is a different number of total layers and one copper layer within these specimens that is thicker, the coating quality has been rated as *okay*. The coating process of specimen A11 has been interrupted by a power outage. The coating quality of specimen A11 was rated *bad* and the specimen was disregarded for any further testing. Specimen B4 was produced with a lower number of total layers and has been given away as a trial copy.

Overall, the quality of the coated specimens is not good, but apt for the fatigue testing. The coating process can and should be optimized further, as elaborated upon in chapter 7.

Table 4.3: Quality overview of NMM coated specimens

Specimen	deviant lay-up	delaminations	Ni burns	rough surface	overall quality	remarks
A4		x		x	*bad*	
A5					*good*	
A11	x				*bad*	untested
B4	x				*good*	trial copy
B11	x	x	x	x	*okay*	
C3					*bad*	
E11		x		x	*bad*	
F4		x	x	x	*bad*	
G3					*good*	
G4		x			*okay*	delamination occurred after clamping
G5				x	*okay*	
G17					*good*	
G18		x	x	x	*okay*	
G33		x	x		*okay*	delamination occurred after clamping
G37					*good*	
G38		x	x		*okay*	
G41		x	x		*okay*	
G42	x	x	x		*okay*	
G43					*good*	

Chapter 5

Results of Mechanical Testing

Three different studies are presented and then discussed in this chapter. A preliminary study is presented in section 5.1, which was published in [68], and was the incentive for the main study. The main fatigue study and core part of this work, with the methods and specimen as described in the previous chapters, is presented in section 5.2. An additional study in cooperation with the *Technical University of Munich (TUM)* with additive manufactured specimens that were coated with Cu/Ni Nanostructured Metal Multilayer (NMM) and tested in fatigue, is presented in section 5.3.

5.1 Preliminary Study on Welded Specimen

The preliminary study is only based on a few samples and is rather extemporary. The study was published in [68] and will be presented in short in this section.

The specimens are cut from welded steel plates that are produced alike to the welding process described in section 3.1.1. The specimens have a length of 135 mm, a width of 10 mm, and a thickness of 8 mm. These samples do not meet the standards for tensile test samples, but are in accordance with DIN 50100:2016-12 [102] for comparative fatigue testing.

Fatigue tests are performed at 10 Hz at $R = 0.015$ and $\Delta\sigma = 0.94 f_y$. As-welded specimens are compared to specimens coated with Cu/Ni NMM patches with a Ni base layer of 1 μm and an overall thickness of 9.56 μm and a Cu/Ni lay-up with layer thickness of 40 nm and 67 nm respectively. The results of the fatigue tests are given in figure 5.2.

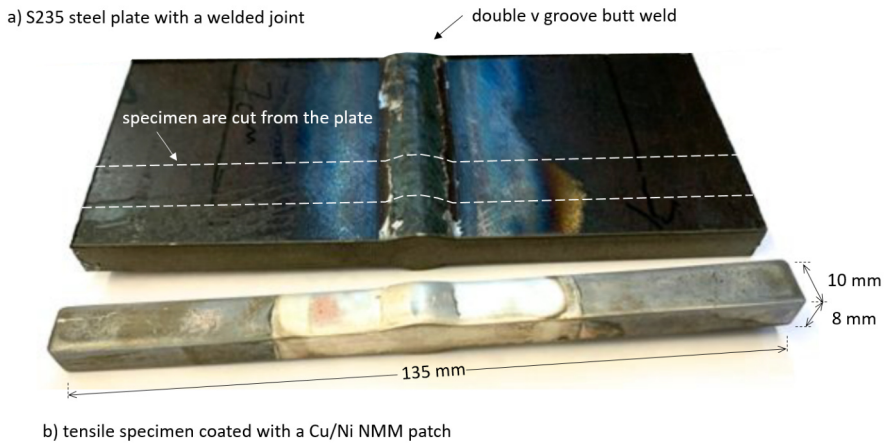

Figure 5.1: Production process of the preliminary specimens; a) the welded plate; b) the coated tensile specimen [68]

A mismatch between the mild steel (S235 measured $f_y = 271$ MPa) and the filler material (SG3 G4Si1 $f_y = 460$ MPa) and the straight form of the samples makes fatigue failures outside the weld area likely and reduces the number of obtainable fatigue results.

The lifetime of the coated specimen increases by a factor of 3 or 4.5 if the run-out is included, due to the low number of results. Even though the number of specimens was low, the fatigue results show a significant increase in lifetime. These results sparked the interest in the following main study (section 5.2) with a proper fatigue sample and enough specimens to create an S-N curves.

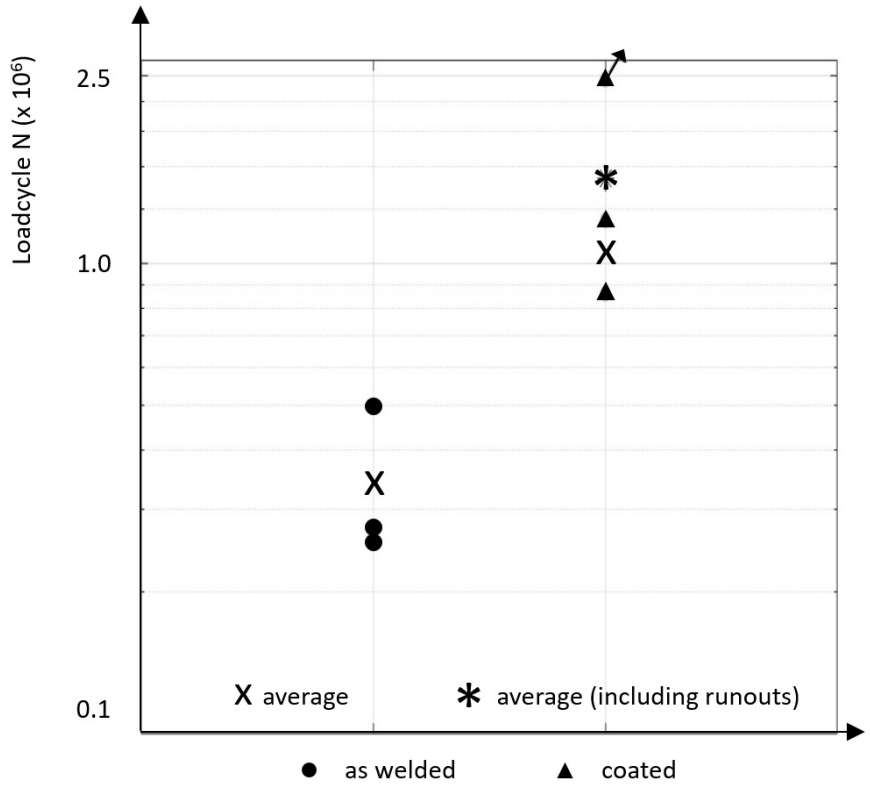

Figure 5.2: Fatigue test results from the preliminary study comparing as-welded with coated specimens for $R = 0.015$ and $\Delta\sigma = 0.94 f_y$ [68]

5.2 Main Study on Welded Dogbone Specimen

Building on the preliminary study, a main study is designed with butt-welded dogbone specimens. The specimens are fabricated and prepared for fatigue testing as described in chapter 3 and coated with Cu/Ni nanolaminate structures as described in chapter 4. Both Cu/Ni nanolaminate coated and conventional post-weld treated specimens are tested in tension-tension fatigue with $R = 0$. As a reference, as-welded specimens and specimens with a machined surface are tested in the same manner. As-welded specimens, specimens with a machined surface, and NMM coated specimens are shown in figure 5.3. Four as-welded specimens are tested in monotone tension tests to determine the yield strength of all samples.

An overview of the samples can be seen in the S-N diagram in figure 5.5. The complete list of all 115 dogbone specimens and the corresponding fatigue test data can be found in appendix A.

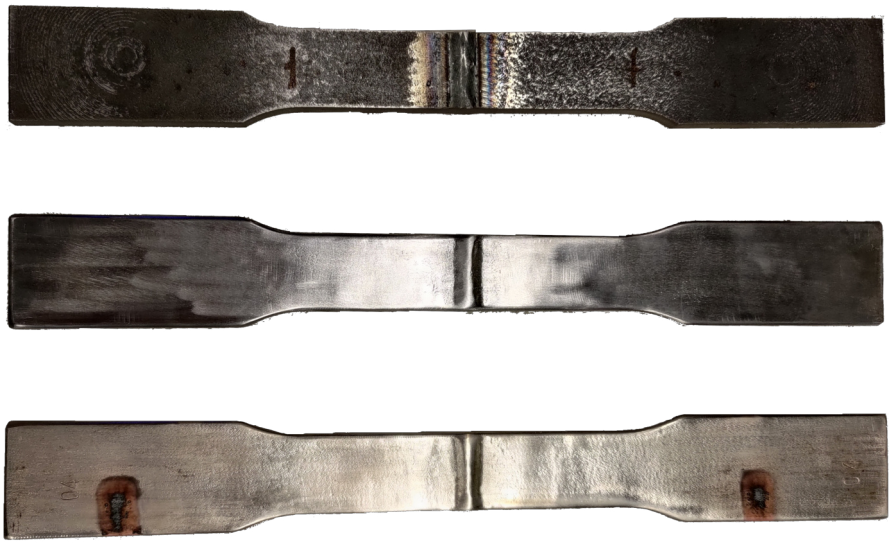

Figure 5.3: Dogbone specimen as-welded, machined and coated with Cu/Ni NMM

5.2.1 Monotone Test Data

Monotone tensile tests were performed to assess the yield strength and the ultimate strength of the dogbone specimens. The stress-strain curve from the monotone specimens can be seen in figure 5.4.

The yield strength of the specimen is 74.36 ± 0.77 kN and the ultimate strength 105.74 ± 1.03 kN. This corresponds with a yield stress of 371.82 ± 3.81 MPa and an ultimate stress of 528.70 ± 5.15 MPa. These values are fairly close to each other and are in good accordance with expected values for a S355 steel. As expected, fracture occurs in the base material. The elongation is $29.5 \pm 0.2\%$ and shows some scatter, especially for sample G31. This can be explained with the sample geometry that does have two areas that experience plastic deformation, one above and one below the weld, instead of just one. For the purpose of simplicity, the yield strength of the samples is taken at the lower bound as 73 kN for the calculation of fatigue loads and the corresponding yield stress of 365 MPa.

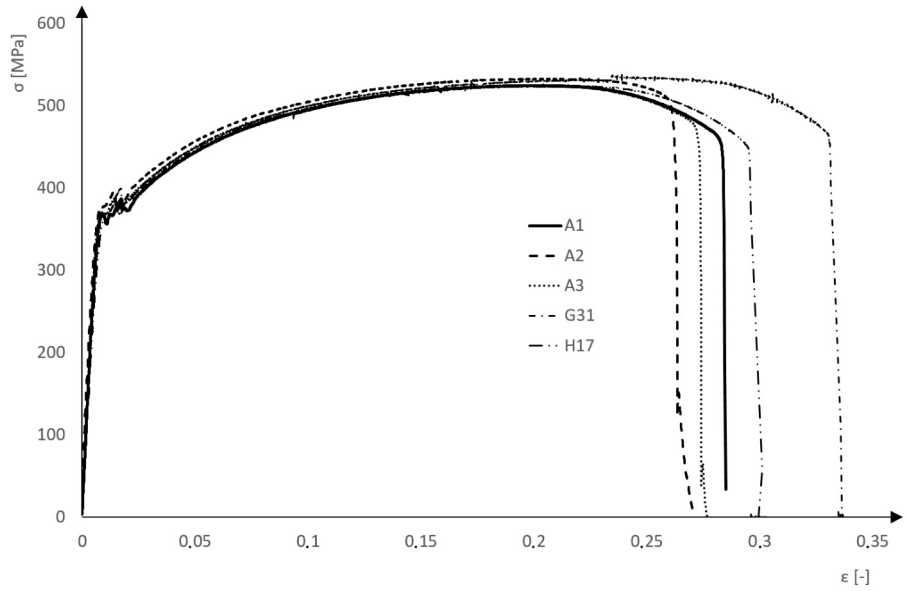

Figure 5.4: Stress-strain diagram for the monotone tested tensile specimens

5.2.2 Fatigue Test Data

Figure 5.5 shows the fatigue test data for all samples on a double logarithmic S-N plot. The FAT classes 80 and 90 are added to the plot as a reference for the test data. The samples that are not included in the evaluation are marked accordingly. This includes specimens that failed at the clamp or in the base material, but also specimens that failed due to the internal welding error discussed in chapter 3.1.1. One specimen with the a surface is taken out of the calculation as an outlier, as will be discussed later. Run-outs with a lifetime of $N > 2.5 \cdot 10^6$ will also be excluded from the calculation of the S-N curves, and are marked with an arrow in figure 5.5. From this plot, it can already be seen that the data scatters a lot and that the FAT class 80 is a good lower bound for the data.

Post-weld treatments are only expected to help the fatigue resistance when the crack is growing from the weld toe. A welding error at the weld root, for example, is not influenced by post-weld treatments (cf. e.g. [96]). Therefore, specimen that failed due to the systematic welding error described in chapter 3.1.1, are not considered for the fatigue evaluation. The same goes for specimen that failed in the base material, run-outs, and failures at the clamp, which are not considered in the S-N curve calculations [102]. These specimens are marked accordingly in the S-N diagrams.

In the following sections, the S-N curves are calculated from the fatigue data for the different sample groups. The results are then evaluated and discussed.

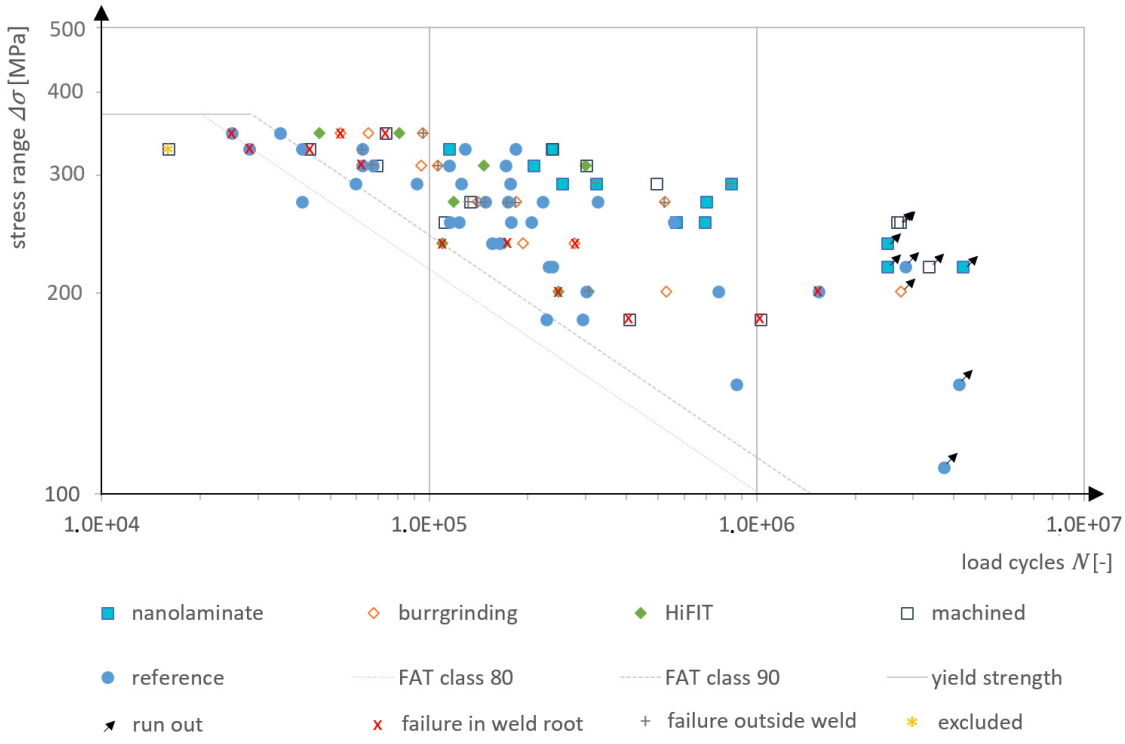

Figure 5.5: Overview over all tested fatigue specimen in a S-N diagram

5.2.3 Reference S-N Curve

A total number of 39 as-welded specimens are prepared and tested as described in chapter 3.2. Three failed from the internal welding error, four failed in the base material, and another three specimen are run-outs. This leaves a sample size of 29 for the calculation of the S-N curves. The resulting S-N curve parameters are listed in table 5.1. Figure 5.6 shows the scatter plot of all reference specimen with the corresponding S-N curves. The 5%-, 10%-, 90%-quantiles are also shown in figure 5.6, while the 10%- and the 90%-quantile shows the range in which 80% of data is included. The 5%-quantile gives the S-N curve that can be used for design purposes [84].

The batch G has slightly different welding parameters than the batches A to F. Therefore, a t-test is calculated to validate that both data sets are from the same population and the different welding parameters do not influence the fatigue results. Comparing batch G with the batches A to F does show a 2% change in the slope, which is negligible, and an increase of the fictional mean. The data is neither showing a significant difference in mean values ($p = 0.301$) nor a difference in standard deviations ($p = 0.3941$) so that the reference samples A to G are considered to be from the same population.

As discussed in chapter 3.2, estimating the slope of S-N curves needs a far larger sample size than tested in this study. Therefore, the slope is taken from the Eurocode 3 as $k = 3$ [84], which includes the calculated slope $k = 2.57$ in the expected estimation range of $2.4 < k < 3.762$ for the sample size of 29 according to DIN 50100 Appendix A [102]. The parameters for the adjusted S-N curve are listed in table 5.1.

Table 5.1: Reference S-N curve parameters for as-welded specimen

specimen	slope k	constant C	fictional mean N_f	standard deviation	variability T_N
as-welded	2.58	11.43	111671	0.252	4.43
as-welded (adjusted to $k = 3$)	3.00	12.45	105115	0.255	4.51

Figure 5.7 shows the adjusted S-N curve with the fixed slope of $k = 3$. Additionally, the S-N curves for FAT 80 and FAT 90 are added to the diagram. It can be seen that the data is a good fit for the FAT class 80 as the 5%-quantile is almost congruent with the FAT class.

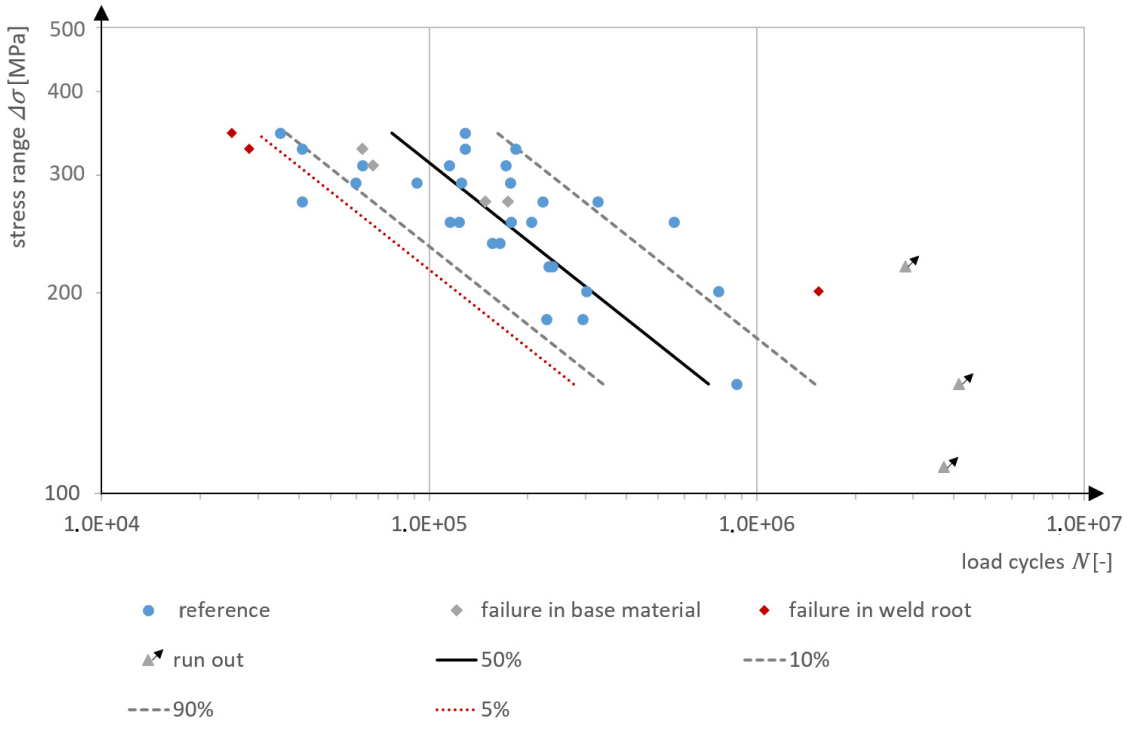

Figure 5.6: Reference S-N curve for as-welded specimen at $R = 0$

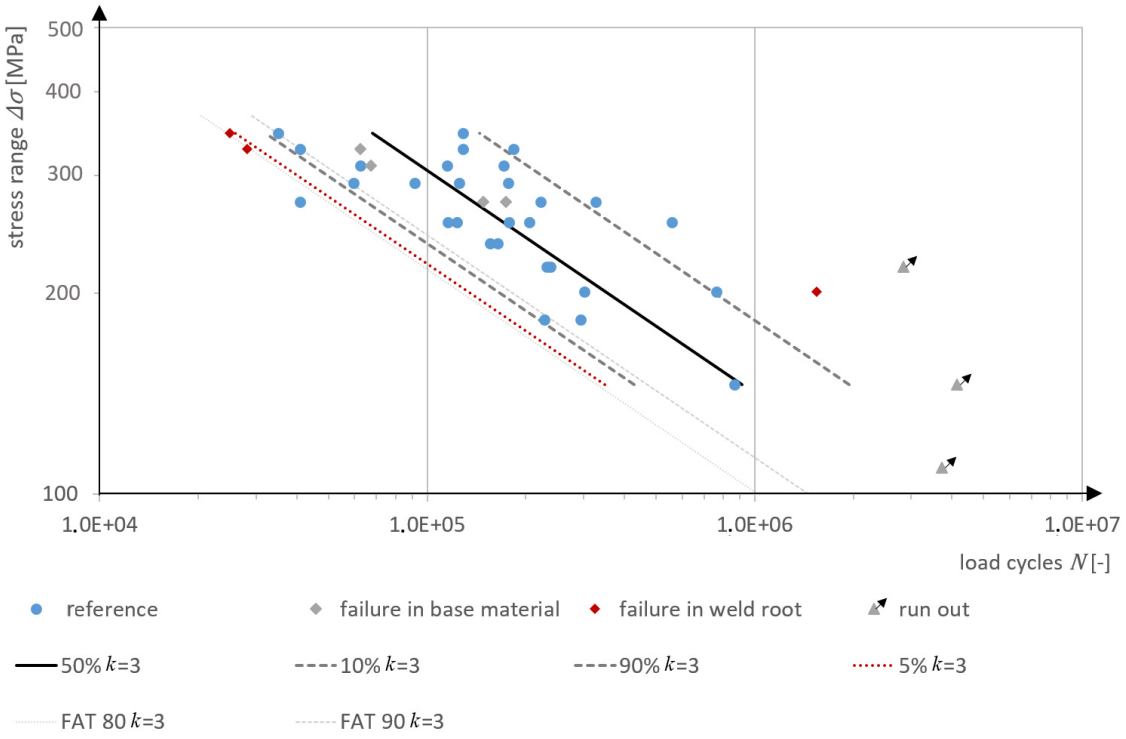

Figure 5.7: Adjusted reference S-N curves for as-welded specimen at $R = 0$

5.2.4 Conventional Post-Weld Treatments

A total of 23 specimens have been treated with conventional post-weld treatments and subsequently tested in tension-tension fatigue. Unfortunately, a large proportion of specimens failed outside the weld area, or at the root. Figure 5.8 shows the lifetime of the sample as well as the S-N curves that have been calculated with the linear regression model.

Ten specimens have been treated with High Frequency Impact Treatment (HiFIT) by the *HiFIT Vertriebs GmbH*. A 3 mm pin was used at 8 bar, 2.5 mm/s pin movement speed and a penetration depth of 0.15 mm to 0.25 mm. Sharp extrusions at the edges were machined down with a fan grinder. During the fatigue testing, one specimen failed in the base material, three specimens failed at the weld root, and six specimens are evaluated for the calculation of an S-N curve. The parameters for the S-N curve are listed in table 5.2. The scatter is relatively high, but as expected for the low sample size. The slope is higher than the reference curve, which is to be expected, and inside the range for a small sample size with an estimated slope of $k = 5$ according to literature [92, 96]. Problematic for the estimation of the slope from the fatigue data is that the upper and lower stress σ_1 and σ_2 are close together.

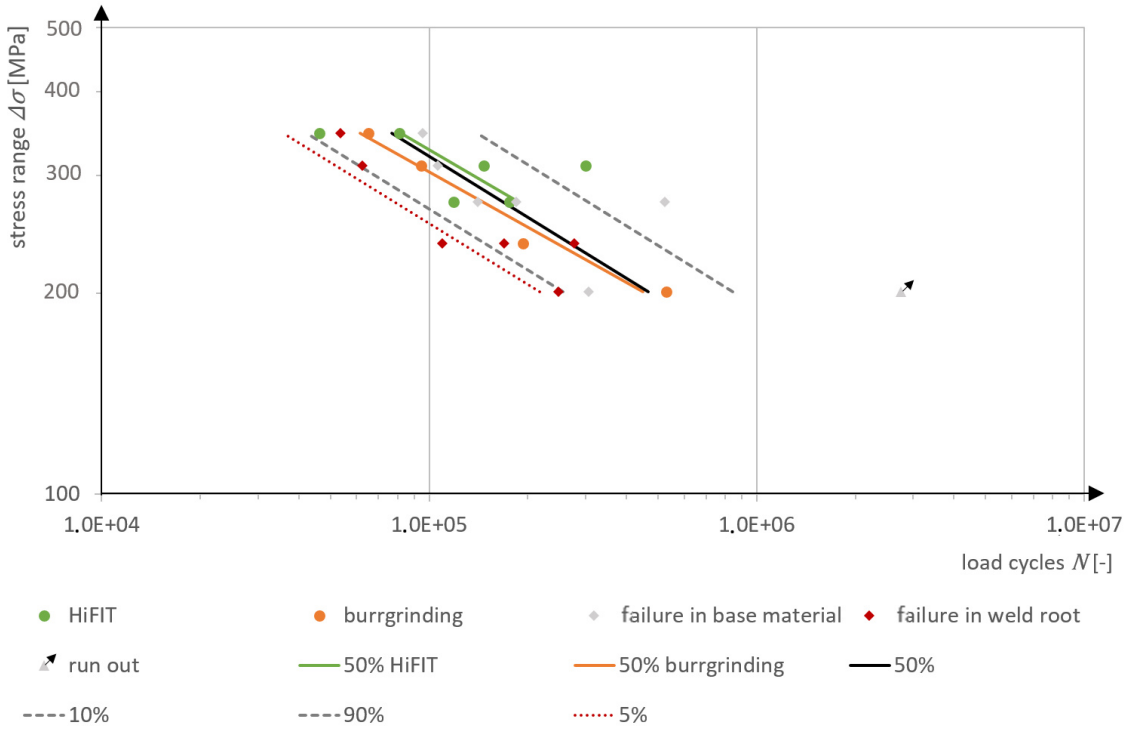

Figure 5.8: S-N curves for HiFIT and burr ground specimen at $R = 0$

Thirteen specimens have been burr ground by the *Institute for Ship Structural Design and Analysis* of the *Hamburg University of Technology*. The burr grinding process is using a 6 mm BSF burr grinder at 27,000 rpm. The die grinder is hand-guided and the weld toe is ground to a depth of ~ 0.5 mm. Five specimens failed in the base material, three specimens failed at the weld root and one specimen is a run-out, which only leaves a sample size of $n = 4$ that failed at the weld toe, and can be evaluated herein. The parameters for the S-N curve are listed in table 5.2. The slope is similar to the HiFIT slope, but the scatter of the data is much smaller than expected for an extremely low sample size of $n = 4$. The results should therefore be evaluated with caution. A recent overview paper proposes a slope of $k = 4$ for burr ground specimen [113], which would be a good match for our data. But the International Institute of Welding (IIW) code is proposing a slope of $k = 5$ for burr grinding [93], which also is a good fit and inside the range of possible S-N curve slopes for the data.

Since both S-N curves from the conventional post-weld treatment methods are close together, as can be seen from the S-N curves in figure 5.8, and the literature sorts both methods into the same FAT class with the same slope [93], a third S-N curve is calculated from both data sets, which yields a more stable calculation for the S-N curve with a larger sample size of $n = 10$. The parameters for the S-N curve are also listed in table 5.2. Figure 5.8 additionally shows the 5%-, 10%-, and 90%-quantiles

for failure of the combined S-N curve.

Table 5.2: S-N curve parameters for conventional post-weld treatment methods

specimen	slope k	constant C	fictional mean N_f	standard deviation	variability T_N
HiFIT	3.50	13.80	136,113	0.274	5.03
burr grinding	3.64	14.04	104,408	0.101	1.82
combined post-weld treatments	3.30	13.26	123,920	0.202	3.30

While the sample size for the estimation of the fictional mean is now adequate, the sample size is still pretty low for the estimation of the slope. Therefore, the slope is set to $k = 5$ according to literature. This S-N curve is no longer the best fit for the measured data, but still a good fit and in better accordance with the literature. The standard deviation is increased by 20% and the standard error for the data is increased by 23%. But the scatter of the data is now actually closer to the expected values for such a low sample size according to the statistics simulations from DIN 50100 [102]. The adjusted S-N curves are shown in figure 5.9. The parameters for the adjusted and combined S-N curves with the estimated slope $k = 5$ are listed in table 5.3.

Table 5.3: S-N curve parameters for conventional post-weld treatment methods adjusted to $k = 5$

specimen	slope k	constant C	fictional mean N_f	standard deviation	variability T_N
HiFIT	5.00	17.54	142,190	0.285	5.40
burr grinding	5.00	17.34	89,387	0.227	3.83
combined post-weld treatments	5.00	17.46	118,095	0.241	4.36

With the adjusted data evaluation of the combined fatigue data for the conventional post-weld treatment methods, the 5%-quantile is now lining-up perfectly with the

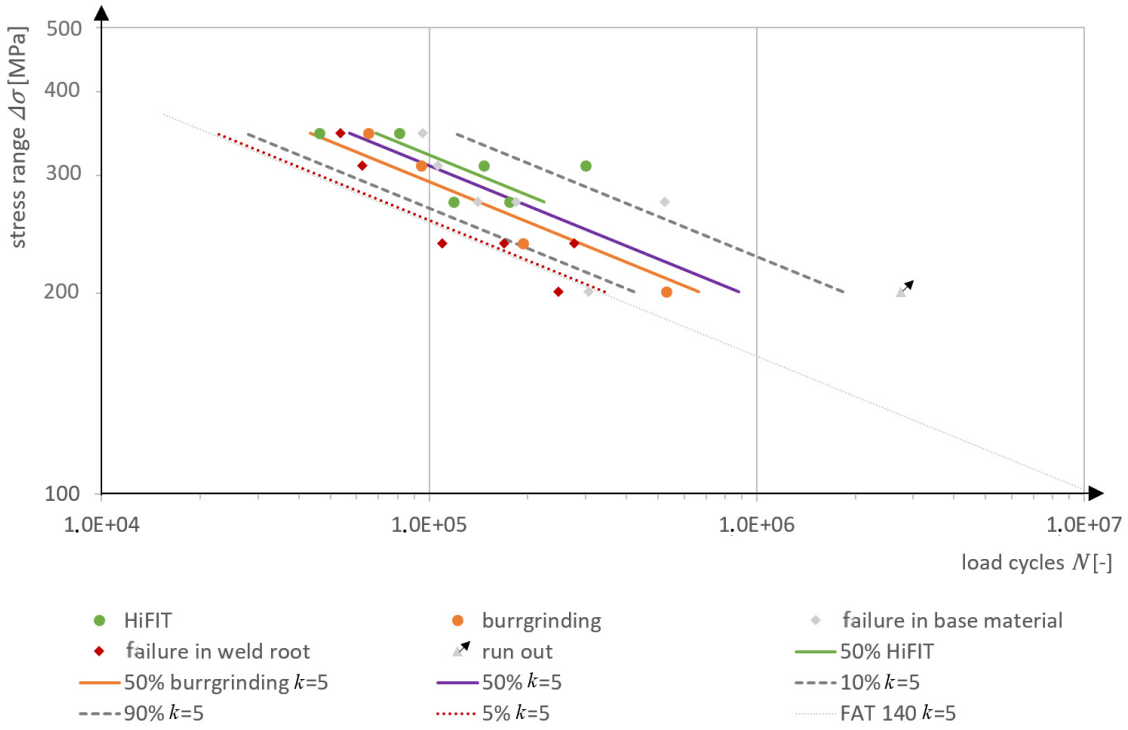

Figure 5.9: Adjusted S-N curves for HiFIT and burr ground specimen at $R = 0$

FAT class 140 with a slope of $k = 5$, which is the fatigue class for burr grinding [93] and HiFIT [92, 96].

5.2.5 S-N Curve for Specimen with Machined Surfaces

As a way to exclude the surface preparation for electroplating as a factor for the lifetime improvement, the surface of 14 specimens is treated the same way as described in chapter 4.2. Of these specimens, only six could be used for the calculation of the S-N curve. One specimen failed in the base material, four failed from the weld root, and three specimens are run-outs. Two of the run-outs (specimen G10 and G32) had been pre-stressed to $\sim f_y$, which might explain the lifetime increase compared to the rest of the samples.

The S-N curve for the specimen with machined surfaces is shown in figure 5.10 including the 5%, 10% and 90%-quantiles. The corresponding parameters for the S-N curve are listed in table 5.4. The scatter of the data is much higher than expected for the sample size. The scatter range should be in the range $T_N = 3 - 4$.

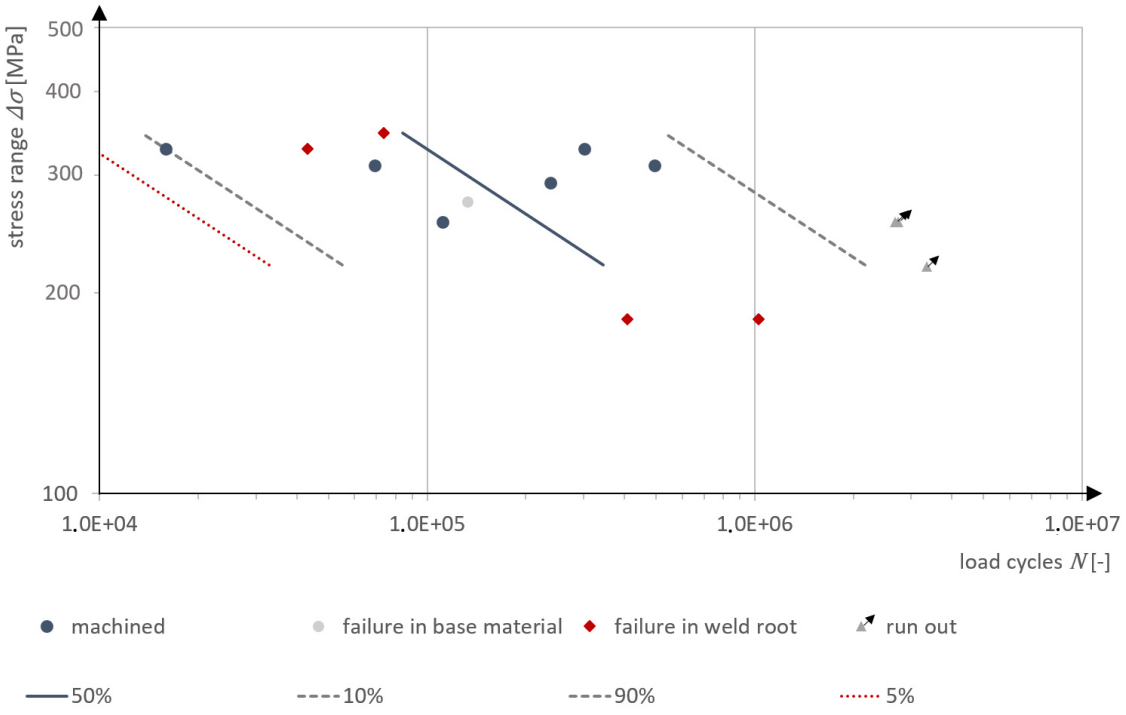

Figure 5.10: S-N curves for specimen with machined surfaces at $R = 0$

To reduce the scatter, specimen C4 is excluded from the calculation as an outlier and the slope of the S-N curve is rounded down to $k = 3$. The new parameters for the adjusted S-N curve are listed in table 5.4.

The fatigue data for the specimen with machined surface scatters a lot and makes the evaluation of the data challenging. The data does not show a significant increase

Table 5.4: S-N curve parameters for specimen with machined surfaces

specimen	slope k	constant C	fictional mean N_f	standard deviation	variability T_N
machined surfaces	3.10	12.81	131,984	0.622	39.38
machined surfaces (adjusted to $k = 3$)	3.00	12.71	190,393	0.487	17.68

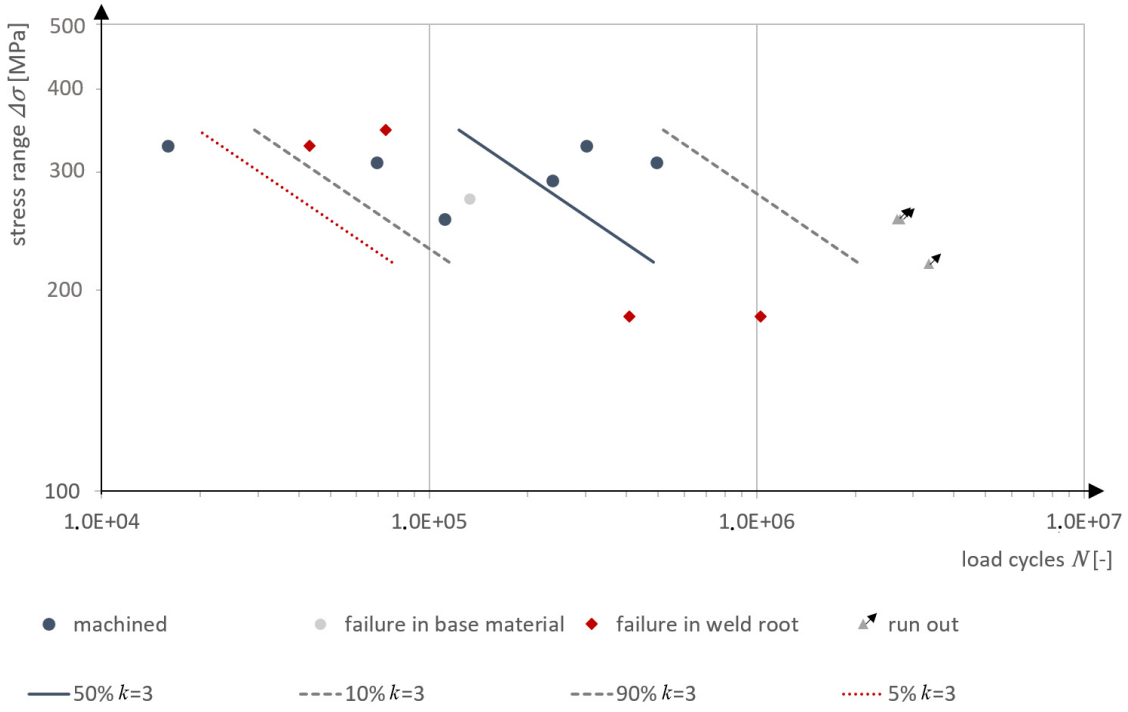

Figure 5.11: Adjusted S-N curves for specimen with machined surfaces at $R = 0$

from the reference. Nonetheless, an increase of the fatigue limit or a lifetime increase by machining the surface is not out of the question and it is well known that surface roughness and surface condition do have an influence on the fatigue life [4].

5.2.6 S-N Curve for Specimens Coated with Cu/Ni NMM

A sample size of 18 specimens have been coated with a nanolaminate coating as a post-weld treatment method. The surface of the specimens are freed from scale by grinding the surface down with angle grinders and fan grinders, as described in chapter 4.2 and thereafter coated with a Cu/Ni NMM structure, as presented in chapter 4. Seven of the specimens do not fulfill the quality standards described in chapter 4.3.3, five of which were tested in fatigue anyway, with one specimen failing at the root. Those specimens are excluded from the sample, but an additional S-N curve is calculated that includes the bad coatings. From the remaining twelve specimens, one failed in the base material, one failed at the clamp, and three were run-outs, leaving a sample of seven for the calculation of the SN-curve, or 11 for the S-N curve including the bad coatings, respectively. The parameters for the S-N curves are listed in table 5.5.

Table 5.5: S-N curve parameters for the nanolaminate coated specimen

specimen	slope k	constant C	fictional mean N_f	standard deviation	variability T_N
nanolaminate	5.80	19.81	271,390	0.148	2.40
nanolaminate including bad coatings	6.35	21.04	208,145	0.246	4.27

The specimens B11, G04, G33 and G42 are highlighted in figure 5.12 and deviate from the rest of the eight samples with good coatings.

Specimens B11 and Sample G42 have a deviant lay-up, because of technical problems with the electrodeposition setup (cf. chapter 4). The lay-up consists of a lower number of bi-layers and has a larger copper layer towards the surface. The performance of both samples is still good and at the upper range of the scatter band. Sample G42 broke at the clamp though and is therefore not used for the calculation of the S-N curve.

The specimens G04 and G33 showed local delamination that showed up during the first load cycle. Compared to the reference curve, they still experience an improvement in lifetime, but are at the lower end of the Cu/Ni nanolaminate coated samples.

The slope of the S-N curve $k = 5.80$ for the Cu/Ni coated specimen cannot be compared to values from the literature. The norm gives an upper and lower error de-

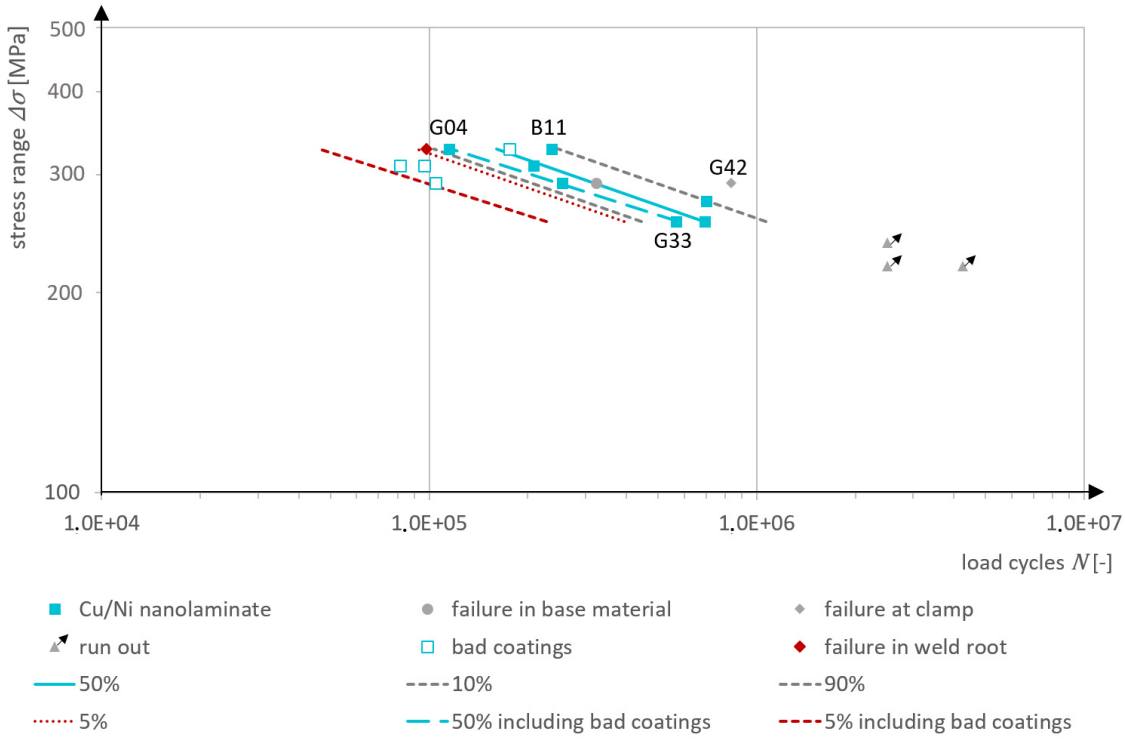

Figure 5.12: S-N curve for nanolaminate coated specimen at $R = 0$

pendent on the standard deviation, the difference between σ_1 and σ_2 and the number of samples n. This gives an upper bound for the slope of $k = 8.6$ and a lower bound of $k = 4.2$. To get a precise ($\pm$ 10%) estimation for k, the number of samples would need to be increased to $n = 100$. The estimation of $k = 5.8$ is rounded up to $k = 6$, which is still a good fit for the measured data. And for the curve that includes the bad specimens, the slope is rounded down from $k = 6.35$ to $k = 6$. The adjusted S-N curves are shown in figure 5.13 and the parameters are listed in table 5.6.

The fatigue class FAT 190 with a slope of $k = 6$ is a good fit to the measured data. For the data including the bad coatings, the fatigue class FAT 175 and $k = 6$ is slightly below the 5%-quantile.

Even the sample with coatings that are evaluated as insufficient and clearly reduce the mean lifetime by $\sim 5\%$, compared to the good NMM coated sample, is still showing a clear lifetime increase in comparison to the reference sample. While this might be by chance, it could also mean that the effect of nanolaminate coatings is more resilient than expected.

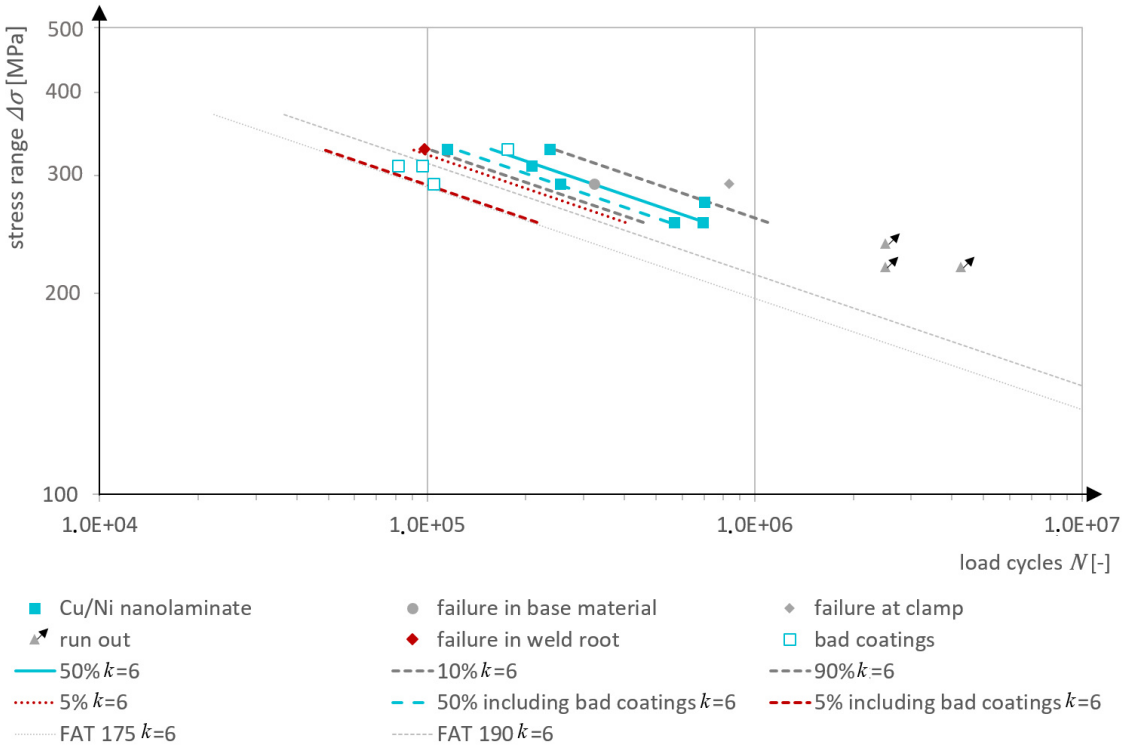

Figure 5.13: Adjusted S-N curve for nanolaminate coated specimen at $R = 0$

Table 5.6: S-N curve parameters for the nanolaminate coated specimen adjusted to $k = 6$

specimen	slope k	constant C	fictional mean N_f	standard deviation	variability T_N
nanolaminate	6	20.23	269,675	0.149	2.41
nanolaminate including bad coatings	6	20.18	208,754	0.246	4.28

5.2.7 Comparison of S-N curves

Figure 5.14 shows all measured data points just as figure 5.5 does, but with added areas that show the calculated 80%-ranges of the different data sets. This 80%-range is the area between the 10th percentile and 90th percentile of the corresponding data. This already shows that there is quite some overlap between the samples, as well as the scatter of the data. It can also be seen that the Cu/Ni coated specimens have a clear influence on the fatigue data and are vastly different from the reference sample, as will also be discussed later.

For the comparison of the different S-N curves, the adjusted curves with the fixed slopes are used. This makes the comparison easier, especially to the FAT classes. The lifetime increase of the conventional post-weld treatment methods is slightly higher through the slope adjustment, the lifetime increase of the coated specimen slightly lower.

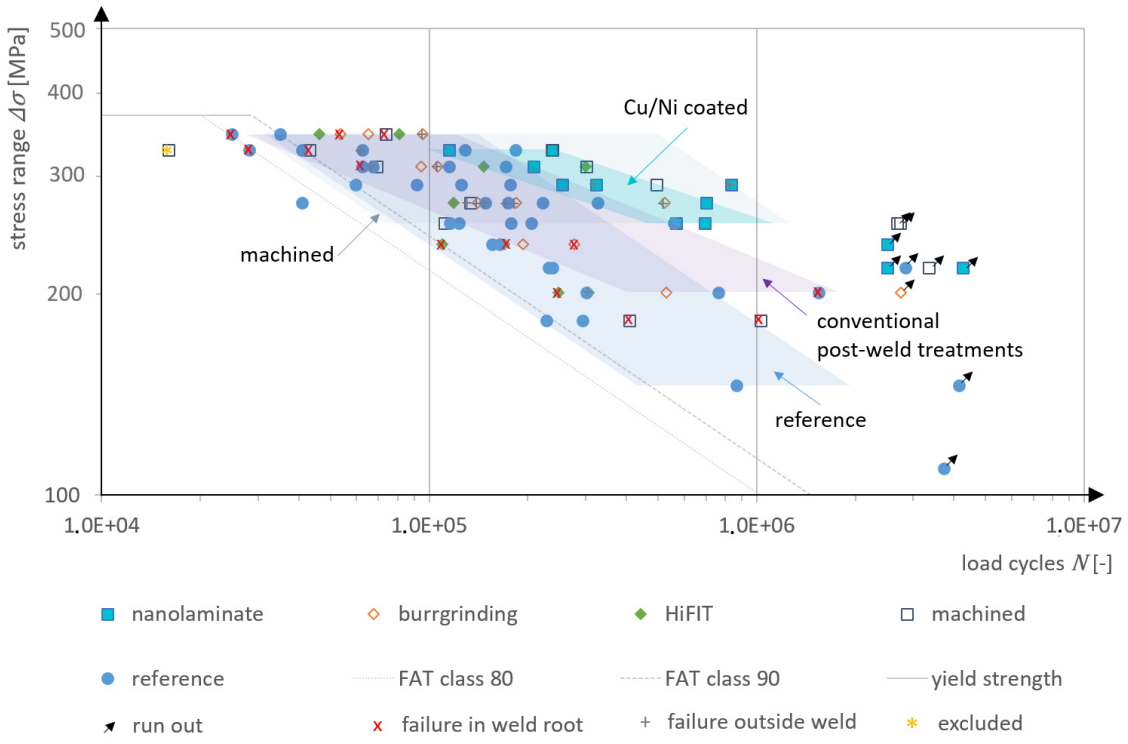

Figure 5.14: Scatter plot of fatigue specimen with colored areas showing the 80%-range

As the fatigue design of structures is not calculated from the mean, but from the failure probability given by the 5th percentile, overlap between the samples is not necessarily relevant. For engineering purposes, the 5%-quantiles are shown in figure 5.15, including the corresponding FAT curves that are fitting to the test data from the literature. This shows the utilizable lifetime increase much cleaner than the scatter plot above. A comparison between the reference curve, the curve with the conventional post-weld treatment methods and figure 2.17 shows that the data is in good accordance with the literature, with an increase from FAT 80 to FAT 140 including the overlap at the higher stress ranges, where HiFIT and burr grinding is not improving the lifetime of welded joints. The increase to FAT 140 is one FAT class higher than by the IIW [93]. The S-N curves for Cu/Ni NMM coated specimens are not crossing the reference curve and therefore show a lifetime improvement for all stress ranges. The slope of the S-N curve is even higher than the slope for the

conventional post-weld treatment methods. This indicates a comparatively higher lifetime increase with decreasing stress level. This in turn also indicates a fatigue limit increase. For the S-N curves of the as-welded specimens, the NMM coated specimens, and the specimens treated with conventional post-weld treatments, the lowest point of the S-N curve corresponds to the stress range below which only run-outs occurred. This is only an indicator of where the fatigue limit is, as the fatigue limit has not been determined properly. The sample with the machined specimens is showing a lifetime decrease, which can mostly be attributed to the high scatter and high standard deviations of the data, rather than a measured lifetime decrease for these specimens.

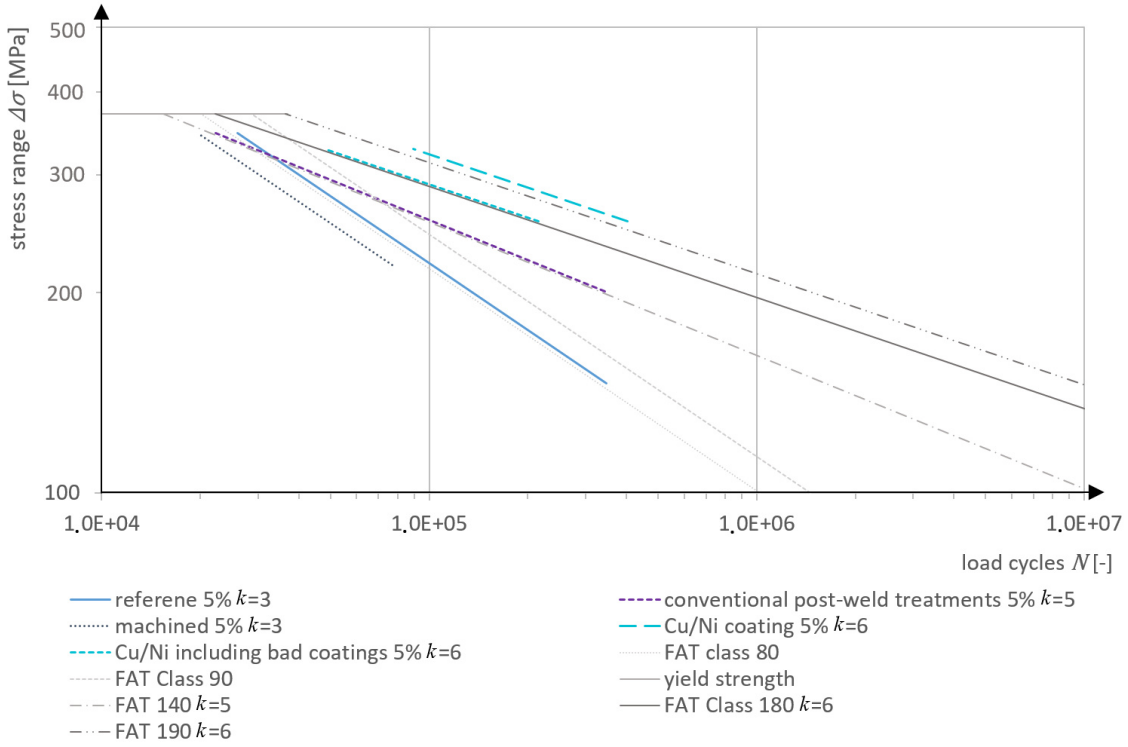

Figure 5.15: Design S-N curves derived from the 5%-quantiles compared to the corresponding FAT classes

The lifetime increase of specimens treated with conventional post-weld treatments, the Cu/Ni coated specimens and the specimens with a machined surface are shown for three different stress ranges in figures 5.16 for the mean increase and 5.17 for the increase at the 5%-quantile. This shows the clear potential of the Cu/Ni nanolaminate coatings for the use as a post-weld treatment and also the advantage of the NMM coating compared to conventional post-weld treatment methods. The increase is calculated from the adjusted S-N curves, which explains the constant increase/decrease in the specimens with the machined surface, since the S-N curve for the reference

sample has the same slope. The lifetime increase at the different stress levels for the conventional post-weld treatment methods is more effective for lower stress ranges and ineffective or even harmful at stress ranges close to the yield strength, which is in good accordance with the literature (cf. chapter 2 figure 2.17). The NMM coating is already effective close to the yield strength and with a lifetime increase factor between 300% and 600% much higher than the lifetime increase between 20% and 60% for the conventional post-weld treatment methods.

To assess the statistical significance of the fatigue data, paired t-tests and f-tests are used, with a significance of $p \leq 0.05$. The resulting p-value gives the probability, that the data sets actually come from the same population and the measured increase is only by chance; a significance of $p \leq 0.05$ is necessary to rule out that the increase is random. The significance of the data is dependent on the sample size, the scatter, and the difference in mean values. Figure 5.18 shows the mean fatigue values including error bars for the fictional load level of 300 MPa. The error bars represent the calculated standard error for the respective sample size. Even though only 4 burr ground specimen were evaluated, the data points are lined up very close, as discussed above, and therefore the mean value is calculated with a higher certainty and smaller error bars than is to be expected from such a small sample size. Additionally, the mean value for this sample is lower than expected. The confidence intervals for the HiFIT data shows both the expected increase in lifetime and a scatter that can be expected from the low sample size. The combination of HiFIT data and burr grinding data increases the sample size and reduces the uncertainty for the mean value. Because of the high overlap between the reference and the post-weld treated sample (cf. figure 5.14) and the low amount of data points that could be evaluated for the post-weld treated sample, no statistically significant increase could be obtained. Nonetheless, the evaluated data is in good accordance with the expected lifetime increases taken from the literature.

As already discussed, the machined samples experience a high amount of scatter and the mean value is determined with a high uncertainty. The data is not statistically significant because of the relatively small lifetime increase, the relatively high scatter of the reference sample and the low sample size. The samples that were coated with Cu/Ni nanolaminate have a low scatter and a mean value that is a lot higher than both the reference data and the machined data. For the comparison between the as-welded sample and the nanolaminate coated sample, the result is statistically significant ($p = 0.0005$). The high standard deviation of the machined sample does not allow a statistically significant distinction of the mean values between the machined and the nanolaminate coated sample ($p = 0.0535$). However, the variance comparison

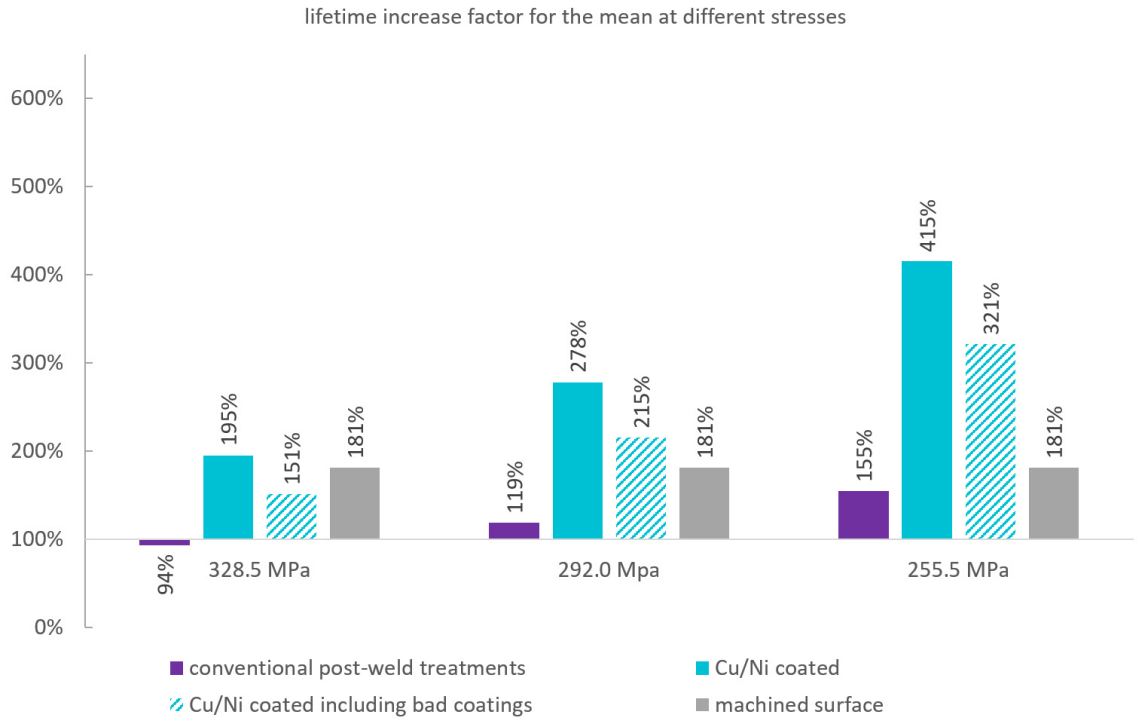

Figure 5.16: Mean lifetime increase factor for different stress levels

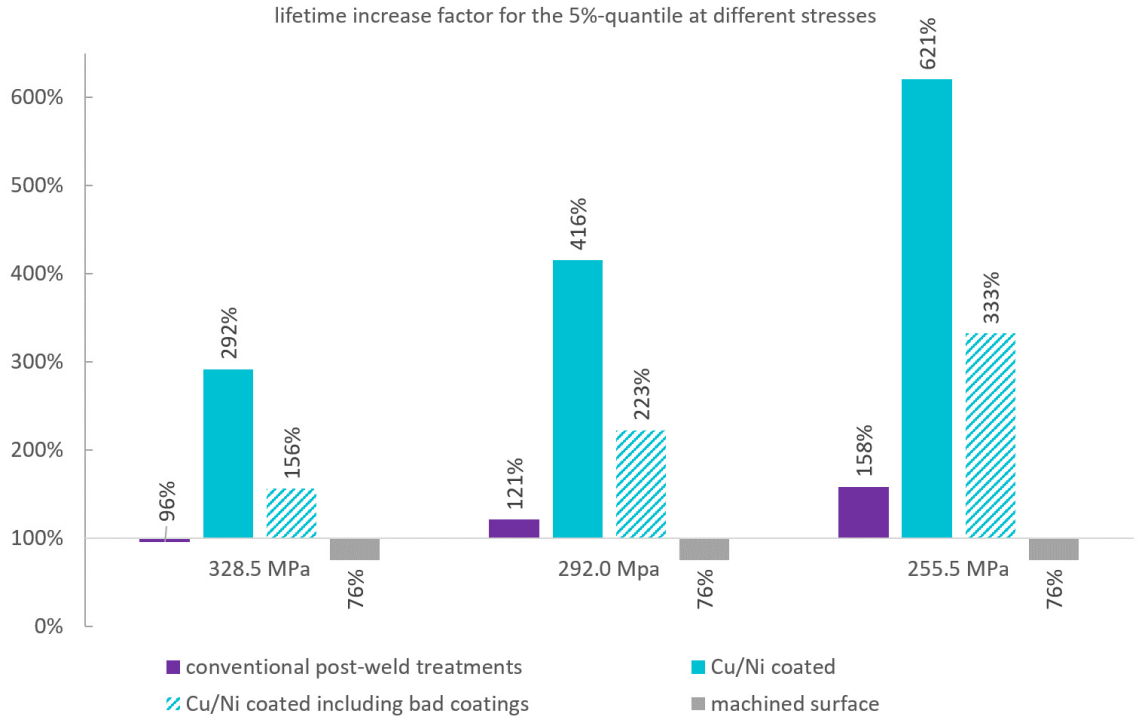

Figure 5.17: Design lifetime increase factor for different stress levels

(f-test) shows that the two samples are significantly different ($p = 0.0117$). This shows a clear distinction between the reference sample and the Cu/Ni NMM coated sample. Including the specimen that are coated with a coating that did not meet the standards presented in chapter 4.3.3, the data still shows a clear improvement ($p = 0.007$) in comparison to the as-welded sample.

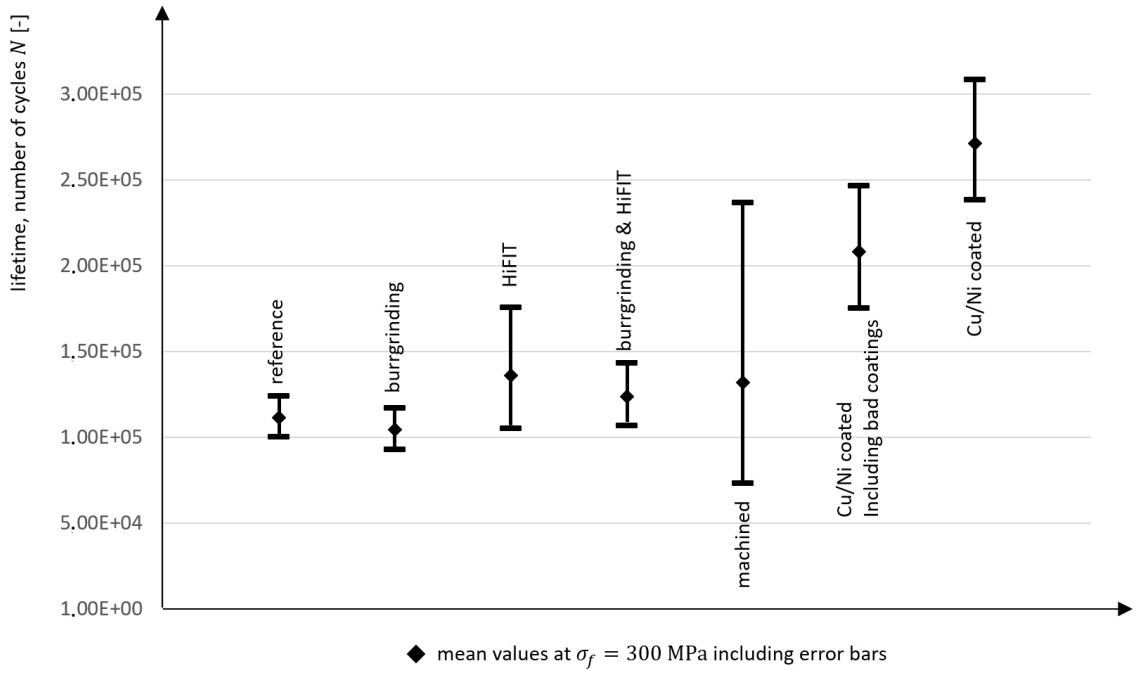

Figure 5.18: Comparison of mean fatigue results including error bars at a fictional load level of 300 MPa

In summary, the fatigue data shows, that the application of Cu/Ni nanolaminate coatings is increasing the mean lifetime of welded specimens by a factor between 2 and 4. The FAT class that best fits the curve for Cu/Ni NMM coated specimen is FAT 190 with $k = 6$, which corresponds to a fatigue design lifetime increase by the factor of 3 to 6. Even so, the data of the sample with the machined surfaces could not be evaluated properly, it becomes clear that the sample preparation, namely the machining of the surface, is not responsible for the increase in lifetime of the Cu/Ni coated specimens. A comparison between conventional post-weld treatments with the Cu/Ni nanolaminate from the fatigue testing data is not expedient. But a comparison against literature and the IIW recommendations shows an advantage of the Cu/Ni nanolaminate coatings with an increase of FAT class by an additional 3 to 4 classes. The fatigue limit was not tested according to the staircase method, but below a threshold of $0.7\sigma_y = 255.5$ MPa the nanolaminate coated specimen did not fail below the set run-out limit, which suggests an increase in the fatigue limit of $\sim 75\%$.

5.3 Study on Additive Manufactured Specimen

In cooperation with the *Chair of Metal Structures* of the *Technical University of Munich*, a small study was conducted on the effect of Cu/Ni nanolaminate on additive manufactured 316L stainless-steel specimens. Fatigue is a major problem in additive manufactured specimen and the samples can be considered as notched due to pores in the material with fatigue failure occurring from pores that are close to the surface of the specimen.

Figure 5.19: Additive manufactured samples provided by the TUM and coated with Cu/Ni NMM

Both as-built and polished ASTM E466 [103] and ASTM E606 [104] specimens are successfully coated by electrodeposition with nanolaminate structures.

Eight polished small specimens have been coated with satisfactory results and have been sent to Munich for fatigue testing. Fatigue tests are performed at 18 Hz. A total number of 15 specimens are tested as reference and only three out of eight nanolaminate specimens could be tested for fatigue in the end. Three specimens have been lost to testing errors and another two due to the coating flaking off during the first load cycle. The reason for the coating flaking off is ascribed to plastic deformations with high strain rates that occur during the first load cycle. The high strain rates are caused by faults in the additive manufacturing process.

Figure 5.20 shows the fatigue results for the polished small specimens and the polished specimens coated with a 6 μm Cu/Ni NMM, with a 1 μm Ni base layer and a 5 μm nanolaminate consisting of 90 bi-layers with a thickness of 15 nm and 35 nm, respectively.

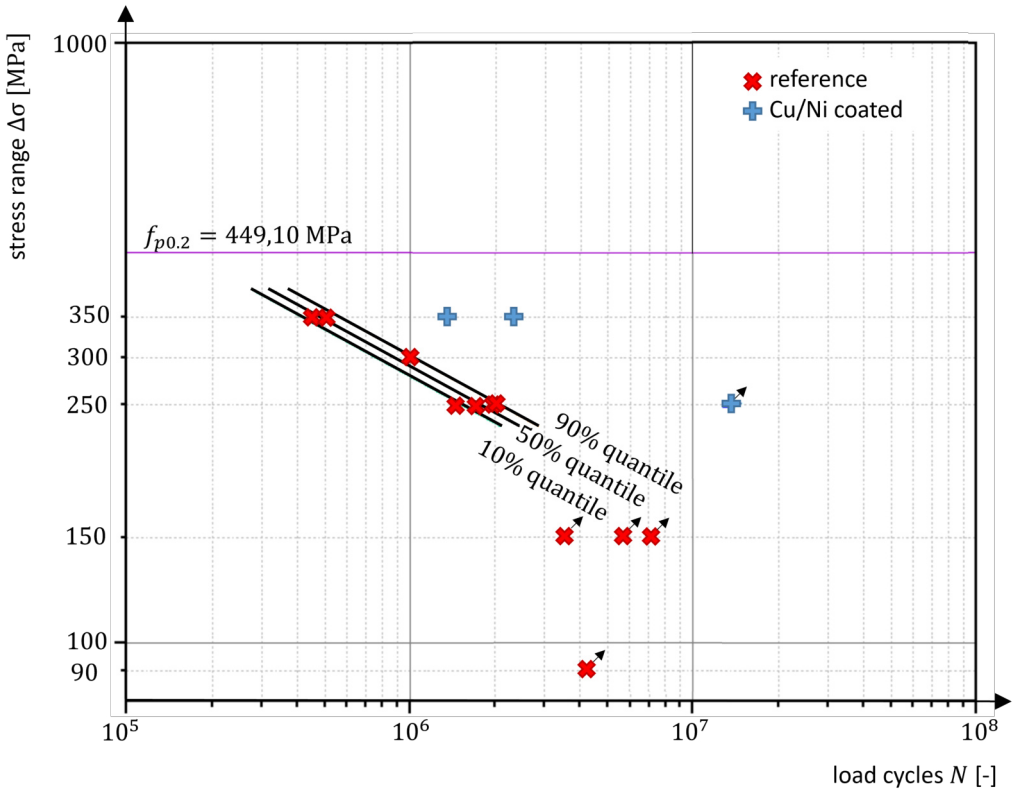

Figure 5.20: Fatigue test data for additive manufactured samples as provided by the TUM

The average lifetime increase at a stress level of $0.78\sigma_y$ is 3.88 and at a load level of $0.57\sigma_y$, the increase was ≥ 7 as the specimen exceeds the set run-out cycle limit of $3.5 \cdot 10^6$ and was finally stopped at $13 \cdot 10^6$ load cycles. While the number of nanolaminate specimen is not sufficient for statistical significant statements about the lifetime improvement, the data makes clear that there is an improvement; that can be attributed to the NMM coating.

5.4 Discussion of Fatigue Results

All three studies show the effectiveness of Cu/Ni NMM coatings as an improvement against fatigue loads, which confirms the findings of both *Stoudt et al.* and *Kaneko et al.* [27, 65]. The lifetime increase is already effective near to the yield strength of the specimen. Lifetime improvements are between 200% and 500%. The smaller lifetime improvements compared to the mentioned studies can be ascribed to the notched specimens that were used, in comparison to the unnotched copper specimens from the previous studies. As already discussed in chapter 2.3, the main reasons for fatigue in unnotched metal specimen is found in Persistent Slip Bands (PSB) formation and crack growth from the intrusions. While notched specimens also experience PSB formation, the crack initiation phase is much shorter because of the higher stress concentrations at the notch. The studies presented above show for the first time that the Cu/Ni nanolaminate coating is also working with notched materials.

The main study shows that the slope of the S-N curve is increased by the NMM coating to $k = 6$ and the fatigue limit increase is estimated to be $\sim 75\%$.

The comparison with conventional post-weld treatment methods, according to the measured data and known standards, shows lifetime increases for NMM coated specimens that go far beyond reported values for post-weld treatment methods.

For the practical application as a post-weld treatment, the main study indicates that a significant increase in lifetime can be reached with the coating of welded joints with Cu/Ni NMM. Additional samples should be tested to further increase the statistical significance.

Chapter 6

Investigation of Failure Mechanisms in Nanolaminate Structures

This chapter aims at giving an understanding of the mechanisms that increase the lifetime of Cu/Ni Nanostructured Metal Multilayer (NMM) coated materials. Section 6.1 characterizes the NMM coating with Scanning Electron Microscopy (SEM), Transmission Electron Microscopy (TEM) and Energy-dispersive X-ray Spectroscopy (EDX) investigations. Section 6.2 investigates cracks in the coating from results of the Focused Ion Beam (FIB) serial cross-sectioning method and TEM analysis of the crack tip. From these observations, hypotheses for the factors that increase the lifetime are discussed in section 6.3. Section 6.4 summarizes the results of this chapter.

6.1 Material Characterization

The nanolaminate lay-up has been imaged with cross-sections, prepared as described in chapter 3.3 and observed with SEM and TEM as well as EDX analysis.

Figure 6.1 a) shows a SEM image of the Cu/Ni coating. On the bottom, the steel substrate can be seen and individual steel grains are visible. On top of the substrate, the Ni base layer can be seen, which has a much finer grain structure than the steel beneath. The NMM lay-up on top of the Ni base layer shows the nanoscale laminate structure. The darker laminae are the Cu layers and the lighter laminae are the Ni layers. The image was taken with the SE detector at 50 pA.

Figure 6.1 b) shows a colorized TEM EDX HAADF bright field image of the Cu/Ni nanolaminate section from the same specimen. A clear and sharp distinction between the different metals can be seen.

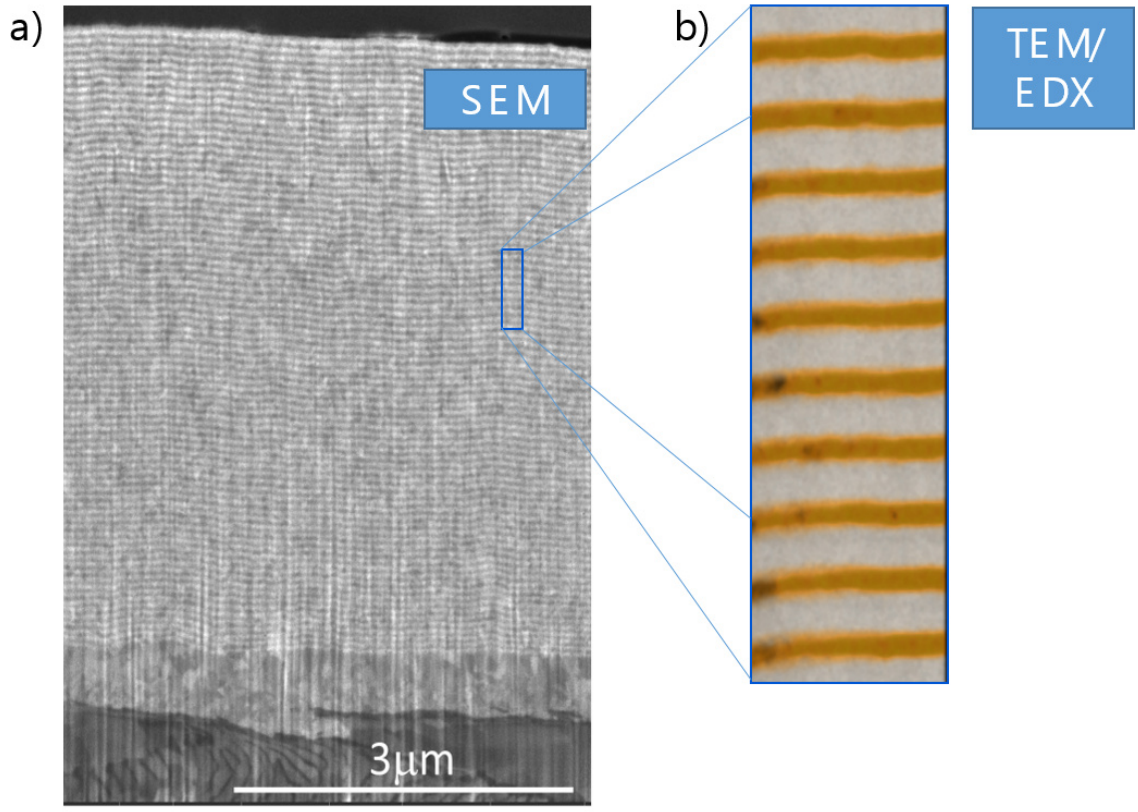

Figure 6.1: SEM and TEM images showing the nanolaminate coating; a) SEM image showing the nanolaminate coating including the NI base layer on the steel substrate; b) close up colorized EDX/TEM image showing the clear distinction between the Cu (orange) and Ni (gray) layers

The influence of the Cu/Ni NMM coating on the fatigue lifetime of steel specimens has been tested, as shown in chapter 5.

The adhesion and scratch resistance of the coating have only been tested qualitatively as part of the quality control of the specimen, as described in chapter 4.3.

Further testing of the material properties has not been performed. Being able to characterize the material properties of Cu/Ni NMM structures is important for future research to generate insights into the failure mechanisms, and by that create the ability to quantitatively assess or simulate the effects of NMM thin film coatings. Further testing methods that were not in the scope of this work are described in chapter 7.

6.2 NMM Failure Mechanisms

The macroscopic crack patterns of the dogbone specimens have been observed with a *Keyence VHX4000 digital microscope*. Alas, no deviations from the expected macroscopic crack propagation behavior, with striations that show areas of crack propagation and monotone fracture zones that occur when the specimen fractures due to overload, have been observed.

However, the microscopic crack pattern in the coating, observed with a TEM lamella that is cut from a fractured specimen, allows an insight into the fracture mechanisms. A crack that is running along the surface of one of the specimens is singled out and a FIB serial cross sectioning method is used to follow the crack to the crack tip; a TEM lamella (cf. chapter 3.4.2) is taken from the crack tip to investigate the crack propagation through the nanolaminate structure.

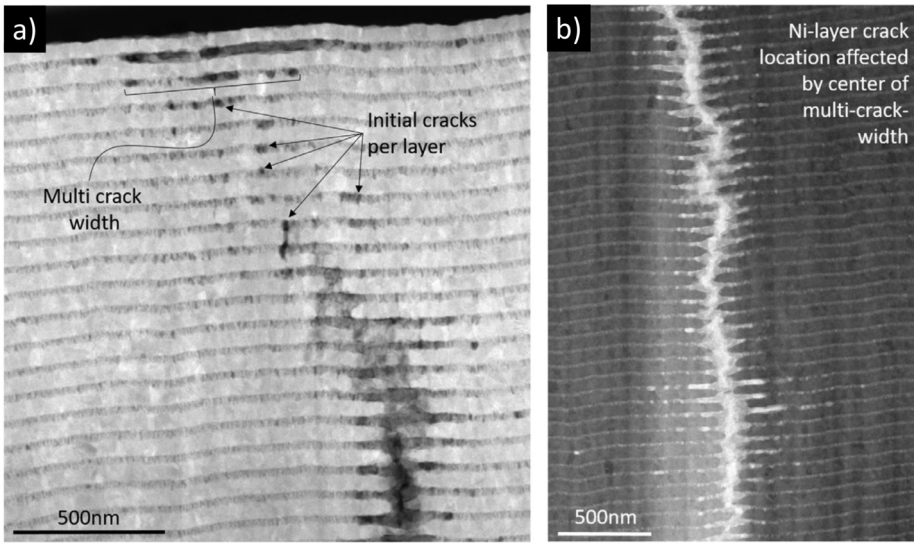

Figure 6.2: TEM images of the crack tip; a) HAADF image of the crack tip closure in the top part of the TEM-lamella with multi-cracks forming in the Cu-layers; b) BF image of the middle part of the lamella showing single cracks in the Ni-layers as well as multi-cracks in the Cu-layers [99]

As can be seen in the TEM image in figure 6.2, the crack is closing towards the surface of the coating. As annotated in figure 6.2, the Cu-layers show initial cracks followed by multi-crack formation, while the Ni layers stay intact. The BF TEM image in figure 6.2 b shows the cracked nanolaminate with retracted Cu layers and jutting Ni layers. As observed, crack propagation through the nanolaminate is controlled by initial cracks in the Cu layers and subsequent multi-cracks forming in the Cu layer (cf. figure 6.2 and figure 6.3).

Since the crack tip shows different stages of the crack propagation in a single image as well as the interaction between substrate and coating, a crack bridging and crack propagation mechanism can be derived and put into a schematic failure behavior as depicted in figure 6.3.

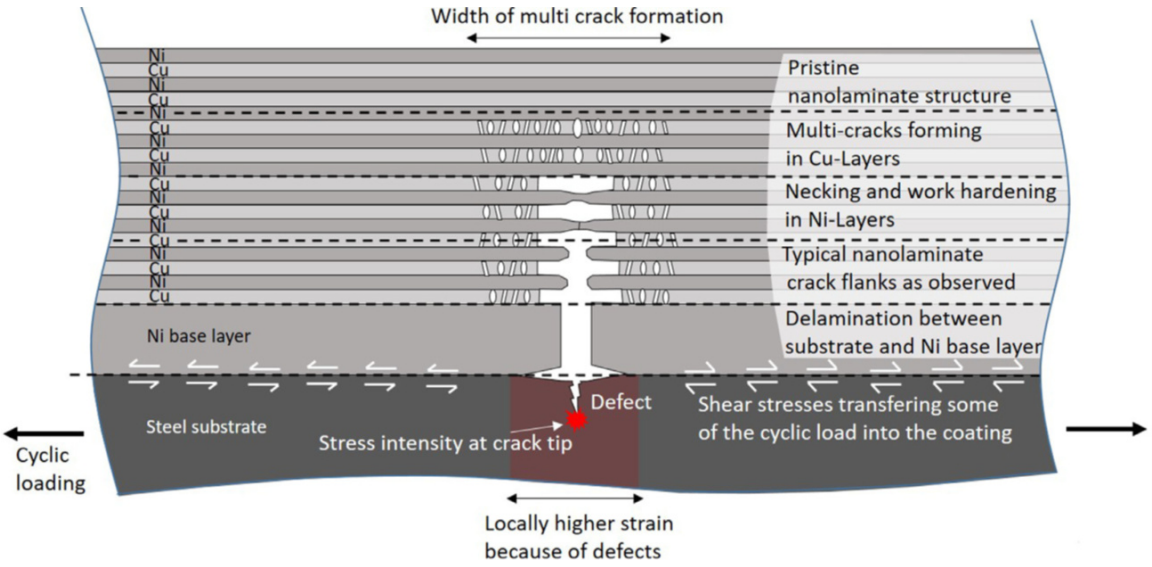

Figure 6.3: Schematic crack bridging behavior and crack propagation behavior of steel with a nanolaminate coating. The crack is growing from the site of an initial defect into the substrate, locally increasing the strain, which results in a crack growth into the nanolaminate towards the surface [99]

The formation of multiple cracks per Cu layer spreading over a certain width rather than a pileup of dislocations leading to a single crack, is presumably caused by the barrier strength and the mismatch of tensile strength of the constituents. The formation of multi-cracks needs more energy than the formation of a single crack. The Ni layers connect the two crack flanks. Each Ni layer ruptures individually with necking and strain hardening. This combination of decoupling the crack propagation into two different mechanisms at the interfaces with a higher energy dissipation and strain hardening behavior is seen as the reason for the superior fatigue resistance.

These mechanisms lead to a unique crack flank pattern with jutting Ni layers and retracted Cu layers, as observed in figure 6.2 b) and schematically shown in figure 6.3. This schematic already includes a macroscopic mode I stress distribution that comes from the cyclic loading and will be explained later. *Wang, Misra and Hoagland* [26] show SEM images with similar crack patterns for freestanding, fatigued Cu/Nb nanolaminate materials without further discussing the crack propagation mechanisms. In figure 6.3, the different crack stages are shown schematically and are annotated on the right-hand side of the figure, from the pristine nanolaminate lay-up, to multi-cracks forming in the Cu layers, necking, and work hardening of separated Ni layers and finally crack opening above an area with higher strain.

Different crack propagation mechanisms are known from the literature and compared to the observations made in this study. *Foecke and Kramer* found that the crack tip is propagating unstably over several multilayers through in situ TEM straining experiments with Cu/Ni NMM in 2003 [52], which does not occur in this study. However, they also found that after Cu and Ni layers fracture the Cu/Ni interface stays intact [52], which is consistent with findings in this study. Further, no shear bands are spreading across the nano multilayers, as described by *Wang et al.* in 2017 [24] and interface crossing is not the governing mechanism, although Cu/Ni nanolaminate have a semi-coherent interface. The crack progression visible in figure 6.2 is not a crack progression from one layer to an adjacent layer due to shear instability as described in [114]. Crack tip blunting is occurring, while delamination and immediate reinitiation in the adjacent layer does not occur, as reported by *Bloyer et al.* in 1999 [115]. *Wang et al.* [116] describe the crack bridging as part of the failure mechanism in Ag/Cu-Zr laminate cantilevers subjected to lateral forces. Crack bridging occurs in the Ag layers with individually rupturing Cu-Zr layer, which is consistent with the crack bridging mechanism observed herein.

The failure mechanisms of NMM semi-coherent multilayers have been theorized to be highly dependent on the bilayer wavelength Λ, Confined Layer Slip (CLS) and interface barriers (cf. chapter 2 or [19]), which fits the multi-crack formation over several layers.

While this crack propagation behavior is in line with common explanations for the increased strength of NMM and the observations are well supported by findings from the literature, it does not clarify why the fatigue life of specimens with Cu/Ni coatings increases.

6.3 Factors for the Lifetime Increase

From the observations in section 6.2 and indications from the literature, three dominant effects are hypothesized to be responsible for the lifetime increase of NMM coated specimens:

- Surface roughness reduction
- Stress redistribution
- Suppression of Persistent Slip Bands (PSB)

The different effects are described in detail in the following sections.

6.3.1 Surface Roughness Reduction

Atomic Force Microscopy (AFM) roughness measurements on nanolaminate coated specimen show that the roughness is decreased by a factor of ~ 10 in comparison between the as-welded specimens and the NMM coated specimens. The measurements are conducted by the *Institute of Materials and X-Ray Physics* of the *Hamburg University of Technology*.

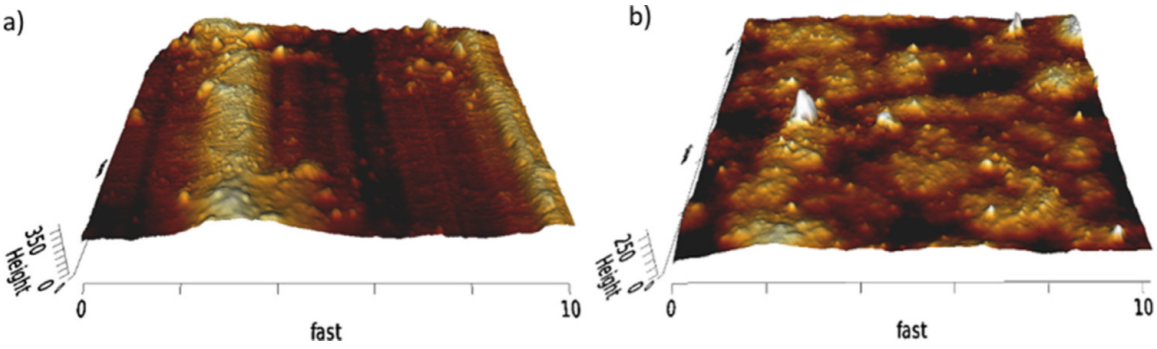

Figure 6.4: 3D-surface topology measured by AFM ; a) uncoated steel specimen at the end of lifetime; b) nanolaminate coated specimen at the end of lifetime [99]

On the one hand, the roughness is reduced by the surface preparation, as described in chapter 3.2. On the other hand, the electrodeposition of Ni has a levelling effect [69]. Figure 6.5 shows the leveling effect of the Ni base layer as well as the levelling effect of the multilayer in a FIB cross-section. The red lines highlight the surface profiles of the steel, the Ni base layer and the final surface. The ground down steel surface is showing sharp shifts, the Ni base layer is still showing the same shifts with a much smoother profile and the final surface is almost completely even.

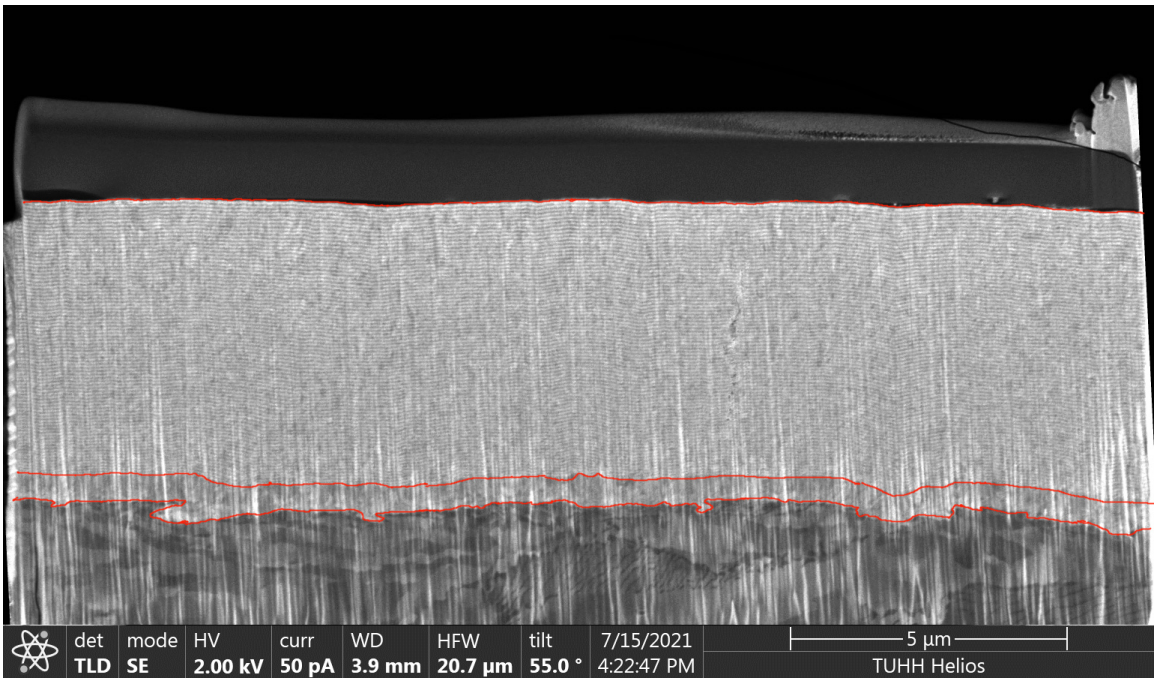

Figure 6.5: SEM image of a FIB cross-section with highlighted surface profiles between the different materials

A reduction in surface roughness has a positive influence on the fatigue resistance properties of metals. While the increase between manufactured and mirror polished surface conditions can be substantial especially for high strength steels, the increase for normal construction steels is around 20% to 40% [4]. This indicates that the lifetime increase between $\sim$ 200% and $\sim$ 500% shown in chapter 5 can only be attributed partly to a surface roughness reduction; other effects have to contribute to the lifetime increase as well.

6.3.2 Stress Redistribution

Adding a high-performance coating to the surface of a low strength material allows for local stress redistributions.

The coating cannot alter the stress state on a macro scale because the coating cross-section area is a few orders of magnitude smaller than the cross-section area of the substrate. Nonetheless, for local stress redistributions at the micro scale, a redistribution of parts of the stresses from the crack tip into the coating will result in a lower stress intensity at the crack tip, which in turn can lead to vastly higher lifetimes. A possible stress redistribution is shown schematically in figure 6.3.

These considerations are only theoretical, though. Direct measurements of these stress redistributions might be possible with in situ tensile testing X-Ray Diffraction (XRD) measurements or with Finite Element Method (FEM) or atomic simulation simulations. For FEM simulations, the material properties need to be understood better and validation will become a problem. Atomic Monte Carlo simulations, on the other hand, can only cover a small fraction of the material and need to be validated experimentally.

This consideration is mostly viable for the macro mode I (opening) fracture component, where the displacements at the surface can be directly linked to normal stresses that are in the plane of the coating. Mode II (in-plane shear) and mode III (out-of-plane shear) that will also occur on the micro scale, will result in deformations that are perpendicular to the coating, for which the coating is not designed. However, deformations like this over multiple grains in the substrate might be able to transform mode II and mode III deformations into in-plane stresses in the coating; a phenomenon that might be described by the PSB suppression.

6.3.3 PSB Suppression

It is well known that intrusions and extrusions are one of the main starting points for crack formation, and the formation of PSB in turn is one of the main factors in the formation of extrusions and intrusions. The Electron Channelling Contrast Imaging (ECCI) measurements of *Kaneko et al.* [65] and the observation from the roughness measurements (cf. [99]) show that intrusions and extrusions do not form in the same way as for uncoated materials. This leads to another suspected factor in the lifetime increase of NMM coated specimen. The suppression of PSB and the formation of intrusions and extrusions will drastically prolong the crack initiation phase.

How this suppression works is not investigated further in the scope of this work, and a numerical understanding of this effect is not existent [117]. ECCI measurements and XRD measurements can be used to determine the influences of residual stresses and the level and depth of PSB suppression, as discussed in chapter 7.

Recent simulated investigations of the interaction between PSB and surface hard coatings, show that the suppression of PSB can indeed increase the fatigue lifetime of materials [117]. The investigation shows that PSBs will induce parallel stresses in the coating and thicker coatings will redistribute these stresses more uniformly. However, the paper found that the brittle failure mechanisms of the coating would favor early crack initiation for higher loads as well as for thicker coatings with a reduction in fatigue life.

While this might seem counterintuitive at first, ceramic high strength coatings have a tendency for brittle failure because of the high Young's modulus and high hardness that will result in high stresses from small deformations. This shows that the high strength and the PSB suppression are not the only prerequisites for the lifetime increase, but that the ductility and the difference in Young's modulus between the coating and the substrate is another factor that needs to be considered. The findings from *Stoudt et al.* also support this and theorize that hard, brittle coatings can lead to a secondary crack initiation that circumvents the PSB suppression [27].

6.4 Summary

The observations and measurements are in good accordance with the literature and build upon the understanding of NMM failure mechanisms, and the way NMM coatings increase the fatigue lifetime.

From the observations and the discussion with the literature, the prerequisites in table 6.1 for lifetime enhancing coatings are derived.

Table 6.1: Prerequisites for the lifetime increase by NMM coatings

- High strength
- Lower Young's modulus
- Ductile behavior
- High cyclic energy absorption
- Residual stresses
- Good adherence and coating quality

These prerequisites are similar to the five properties, *Stoudt et al.* name for coatings to achieve a suppression of fatigue cracks [27], but add the Young's Modulus difference as an additional condition.

Chapter 7

Outlook

This chapter presents ideas as possible incipience for future work that were not followed-up in the scope of this thesis.

In order to make Nanostructured Metal Multilayer (NMM) coatings viable as an economic post-weld treatment method that can be applied to large-scale engineering structures, the scalability, and the electrodeposition process need to be refined. Furthermore, the failure mechanisms and the nanolaminate lay-up need further investigations and testing, as only the fatigue properties have been tested yet and the fatigue data could still be expanded upon.

Figure 7.1: View of the main span of the Köhlbrand Bridge

Ideas for the scalability are presented in section 7.1, exemplarily with a proof of concept project for the Köhlbrand Bridge (shown in figure 7.1).

Section 7.2 provides parameters that could and should be followed up on in the electrodeposition process.

Further mechanical testing methods are presented in section 7.3.1

7.1 Scalability of the Electrodeposition Process for In Situ Use

A prototype for in situ use was developed as part of a science transfer program *Calls for Transfer (C4T)* by the *Hamburg Science and Research Authority*. The prototype was manufactured, but needs further refinement for in situ use at existing structures. The *Hamburg Port Authority* is granting access to the Köhlbrand Bridge (shown in figure 7.1) as part of the 'smart bridge project' [118].

The bridge has problems with fatigue cracks in the orthotropic deck and is due for demolition in 2035. The ribs of the orthotropic plates are discontinued at the cross-beams and welded to the cross-beams from either side. One of the details is shown in figure 7.2.

Figure 7.2: Welding details at the underside of the orthotropic deck that show fatigue damage at the weld toe

For the application, an in situ prototype was developed and built, as shown in figure 7.3.

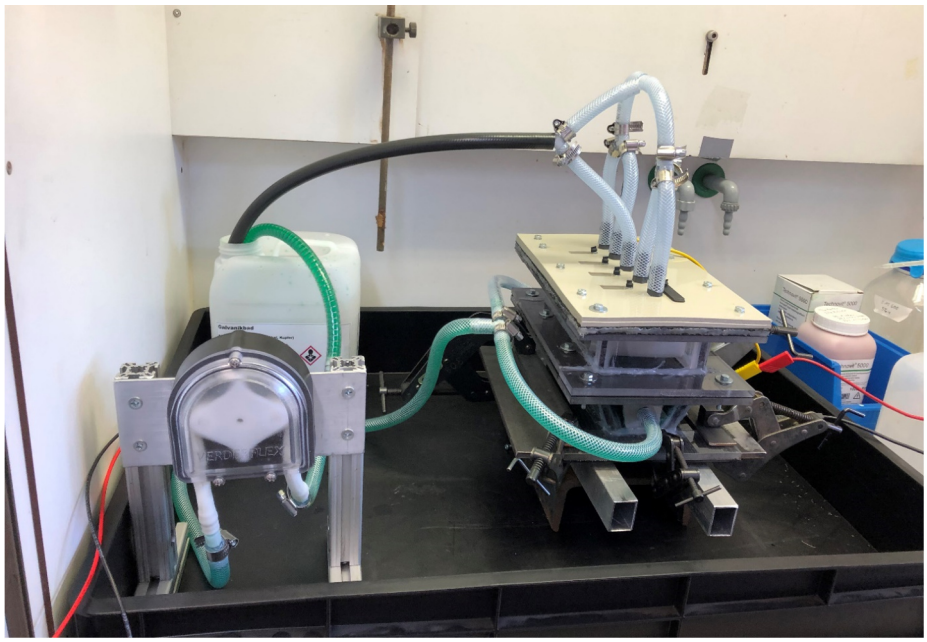

Figure 7.3: In situ prototype set up in the laboratory

There are still issues with the prototype and the proof of concept is still outstanding as documented in the report to the C4T initiative [119].

An alternative to the proposed prototype might be the use of brush plating, either from a single brush (cf. [66]) or multiple brushes with different electrolytes. Especially for rotational symmetric specimen, the latter option could be a suitable alternative. This might be especially interesting for wind turbines and monopiles.

7.2 Improving the Electrodeposition Process

The methods for electroplating at the *Institute for Metal- and Composite Structures* are feasible in the scope of this thesis for the electroplating of specimen as shown in chapters 4. Nonetheless, further improvement of the electrodeposition process is imperative. Almost all process parameters could be further optimized towards better coating results, but especially the sustainability of the process has to be increased for both environmental and economic reasons.

7.2.1 Substitution of Ni

Ni poses severe health risks for workers that come into contact with the metal, especially by inhalation of Ni dust or fumes containing Ni [120]. Therefore, substituting Ni with a different metal would decrease the overall toxicity of the process and would make the work with NMM a lot less laborious concerning safety precautions and personal protective equipment.

The substitute for Ni needs to fulfill the prerequisites listed in table 7.1 for the use in nanolaminate Cu/X patches as presented in this work. A complete new set of metals might also be viable if only substituting Ni will not suffice. These perquisites are derived from the hypotheses on how the Cu/Ni nanolaminate is increasing the lifetime of welded joints, as presented in chapters 6 and 8.

Table 7.1: Prerequisites for the Substitution of Ni

- Less toxic than Ni
- Electrodeposit-able from a single bath electrolyte with Cu
- Achievable metal bond to both Cu and steel by electroplating
- Coherent or semi-coherent interfaces with Cu
- Lower Young's modulus than steel
- Higher strength than Cu

7.2.2 Reusability of the Electrolyte

Since the standing time of complex electrolytes is limited, the time of usage and the waste management of the heavy metal polluted waste waters are an important factor in the sustainability and the costs of the process. This process engineering task has not been tackled yet, but will be essential in the transfer from basic research to application.

The Cu/Ni single bath setup uses two different anodes that replenish the bath with both Ni and Cu ions. The process relies on the chemical stable ratio in Cu and Ni content. Without an active way to control the replenishment process, the bath will change and deteriorate over time.

The base literature [69, 71] is talking about this issue, but the most interesting approaches for the single bath technique are given in [10].

To keep the Cu and Ni ratio constant, only Ni anodes are used in the bath meaning that only Ni will be replenished over time. Trickling a $CuSO_4$ solution into the bath keeps the Cu and Ni ratio constant. Based on bath monitoring, this process could even be improved or automated.

7.2.3 Optimization of Process Parameters

The following sections show possible process parameters that could be changed to further improve the coating quality, since the plating process is time-consuming and there are multiple parameters that affect the coating quality. These parameters should not be adjusted by trial and error, but require extensive parameter studies.

Sample Cleaning and Preparation

In electroplating, problems with adhesion often trace back to problems with grease or oxide films on the surface, which result from insufficient surface cleaning and surface preparation of samples [69, 70, 71, 72]. To increase the quality of plated surfaces, the steps of ultrasonic cleaning as described in section 4.2 could be optimized further and expanded with electrochemical polishing and surface activation steps.

Current Density Adjustments

The optimization of the applied current density for both the Ni and Cu deposition cycles can lead to a better and more homogeneous distribution of the nanolaminate patch across the coated surface. Since the local current density changes due to the different distance of the anode and cathode across the surface as well as local kinks in the surface, the current density is not homogeneous across the surface. Multiphysics simulations of the process with a software like *COMSOL* can deliver insights about the current density distribution inside the bath. Furthermore, a thorough characterization of the electrolytic deposition quality with hull cell tests, as shown in section 4.2 is necessary to gain the upper and lower current density bounds at which the bath can be operated.

Bath Agitation

The hull cell tests indicated that bath agitation is one of the parameters that is important for the coating quality (cf. 4.2). The agitation with the available magnet

stirrer is limited, and the coating quality is inconsistent for the coated specimens, as discussed in chapter 4.3.3. Different methods of agitation enhancement are possible. The simplest solution is the use of a larger magnet stirrer or a second magnet stirrer to increase the agitation. The use of circulation pumps can both agitate and replenish the electrolyte at the same time. This method can be used in addition to the magnet stirring. The flow and agitation of the electrolyte can be directed purposefully and is easier to predict than the agitation of a magnet stirrer. The last option is to agitate the bath by moving the cathode in the bath. This is not as easy to establish because the cathode needs to stay connected to the electrodeposition circuit. However, this method does not only agitate the bath but also varies the distance between anode and cathode constantly, which can further improve the coating quality.

7.3 Material Characterization

The first fatigue tests show a lifetime increase for coated NMM specimens, and the Scanning Electron Microscopy (SEM), Transmission Electron Microscopy (TEM), and Atomic Force Microscopy (AFM) investigations give indications on how and why the fatigue lifetime of NMM coated materials improve.

To characterize the coating further, additional material parameters should be tested.

Other unlisted material parameters that do not influence the fatigue life should also be tested. For example, heat resistance can be tested with annealing, and corrosion resistance with aging tests.

7.3.1 Extended Fatigue Testing

Additional samples should be tested to increase the statistical significance.

For sample preparation, the grinding of the mill scale should be replaced with a surface preparation in accordance with industry standards like [121]. Sandblasting, for example, is one of the main choices to prepare the surface for deoxidation, degreasing and electroplating. This requires new fatigue tests with the adjusted surface treatment, to see if there is a difference between the sandblasted and ground samples.

Since the fatigue-testing data shows an improvement in lifetime for welded joints, as discussed in 5, it is of interest if NMM coatings are also feasible for the renovation of structures. Therefore, pre-fatigued or pre-damaged samples should be coated with Cu/Ni NMM fatigue tested to see if those specimens still experience a lifetime improvement.

Two different methods for testing this are possible:

- Loading fatigue specimens to a fraction of the estimated number of load cycles, then coating the specimens with a Cu/Ni NMM coating and then continue the fatigue testing. Because of the high scatter in fatigue data, numerous specimens will be needed to get conclusive results.
- Samples with a predefined notch can be produced in accordance to ASTM E647 [122] or in scaled down versions by cutting into the sample even down to a few microns with Focused Ion Beam (FIB) cutting. It is a hypotheses that there is an initial notch size which can be equalized by coating the sample with a Cu/Ni NMM.

Additionally, pre-damaging already coated specimens should provide an insight in how a damaged coating influences the lifetime. Even though the wear resistance of NMM is high, initial damage should be incorporated into testing.

Tests according to ASTM E647 [122] can also be used to see if the crack growth rate is influenced by applying NMM coatings. This might be interesting, even though the discussion in chapter 6 suggests that only the crack initiation phase is influenced by the Cu/Ni NMM coating.

7.3.2 Additional Mechanical Testing

The fatigue testing yields only indirect information on the mechanical properties of the Cu/Ni NMM coating.

To gain a more in-depth understanding of the coatings and the lifetime improving mechanisms, mechanical testing of a freestanding NMM thin film is needed. The additional mechanical testing is also necessary as a way to gain necessary information for simulations. Both for material modelling and for the validation of calculations. Especially parameters like yield strength f_y, fracture strength f_u, and Young's modulus E are still unknown for the electroplated coatings presented in this thesis.

Nanoindentation testing is most commonly used for the characterization of thin films. While this allows good comparison to the literature, important material properties, like yield strength, fracture strength and Young's modulus cannot be ascertained (cf. chapter 2.1).

Multiple ways of thin film testing have been developed that go beyond the nanoindentation testing, including (but not limited to) micro-pillar testing, micro-cantilever

testing and micro-tensile testing, as well as bulge testing [123]. Especially, tensile testing that can be used in situ with SEM (cf. [124]) or TEM (cf. [125]) could result in new findings about NMM failure mechanisms. However, extremely small-scale tensile specimen are known to behave differently from bulk materials [125].

Bulge testing allows for bulk thin film tests and can yield all the aforementioned material parameters. Figure 7.4 shows the bulge test setup at the *Institute for Metal and Composite Structures*.

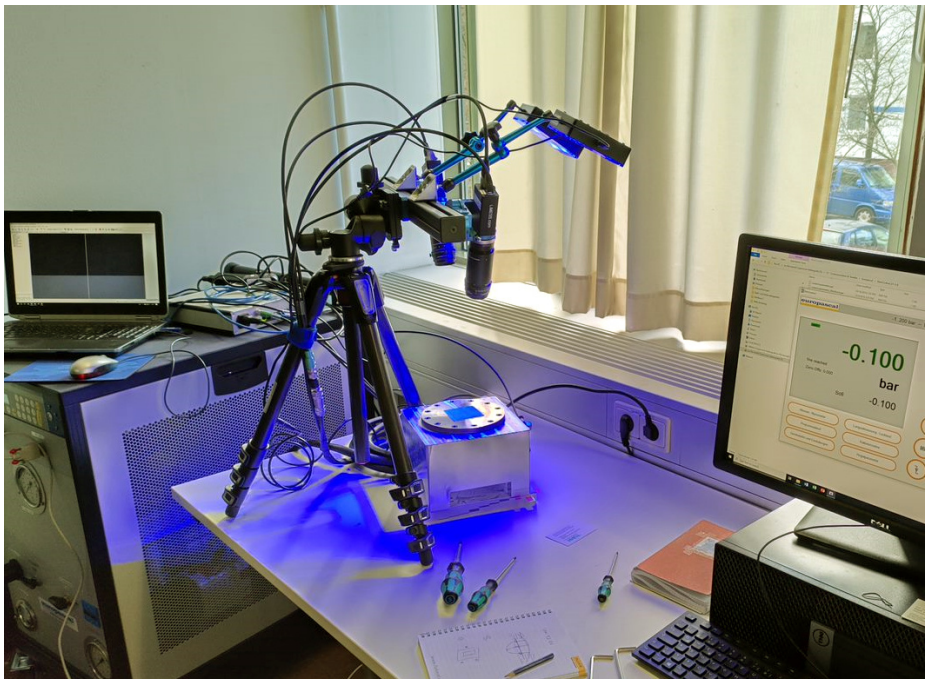

Figure 7.4: Bulge test setup with a *Limess Q400* 3D digital image correlation for displacement measurement and direct strain measurement of the bulged thin film

7.3.3 Additional Investigation Methods

The following investigation methods seem promising, but could not be utilized in the scope of this work:

The Electron Channelling Contrast Imaging (ECCI) technique can be used to confirm the results, *Kaneko et al.* found [65] for the Persistent Slip Bands (PSB) suppression of NMM coated Cu fatigue specimens, by looking for PSB suppression in NMM coated steel specimens. This could further validate the hypotheses from chapter 6.3.

First X-Ray Diffraction (XRD) measurements conducted in cooperation with the *Karlsruhe Institute of Technology* research group *Institute for Applied Materials – Mechanics of Materials and Interfaces* showed promising results and residual stresses in the NMM that will need further investigation.

7.3.4 Additional Simulated Investigations

With a more profound understanding of the material properties, simulations of the NMM failure mechanisms, stress redistribution as a result of NMM coatings, and macro crack propagation through NMM coated substrates become viable. It has to be noted that three vastly different simulation methods are necessary to calculate the different effects. These simulations and calculations could provide a quantitative understanding of the different lifetime increasing factors that contribute to the lifetime increase of NMM coated specimens.

The observed failure mechanisms in the nanolaminate thin film, discussed in chapter 6.2, show an intricate behavior that is strongly dependent on the nanolaminate lay-up. Further optimization of this lay-up without extended parameter studies is only possible by simulating the nanostructured material on an atomic level, with the help of molecular dynamic simulations (cf. [40]). While these simulations do provide insights without extensive prior knowledge about the materials, they are hard to validate and require expert knowledge about the simulation process.

To assess the stress redistribution that could change the stress intensity at the crack tip (cf. chapter 6.3), Finite Element Method (FEM) simulations could provide insights on how much the stress redistribution attributes to the lifetime increase. These simulations are relatively easy to set up, but will need good knowledge about the material parameters and interface behavior, which would need extensive mechanical testing.

Even though, the main effect of the lifetime improvement is attributed to the crack initiation phase. Measuring or simulating the crack propagation is a well-known practice and can prove that the lifetime improvement is not happening in the crack propagation phase or if the crack propagation rate is reduced by NMM coatings, as already mentioned above. The simulation of crack propagation with Extended Finite Element Method (XFEM) is a well-known practice and was established in [126]. More recent investigations also included bi-material interfaces [127] and coated materials [128]. However, the simulation of the crack propagation requires detailed knowledge of the material properties, which requires mechanical testing of the NMM material properties.

7.4 Joining of Nanolaminate Structures

Nanostructured metal multilayers are meta-stable systems that rely on the interface between the different metals as diffusion barriers, making the traditional joining methods for metals impractical. Welding will melt the metals and destroy the nanostructured lay-up, creating an alloy rather than a nanostructured material (cf. [44]). Glue, rivets and similar methods will create a weak link in the NMM lay-up.

A first joining method was established for vapor-deposition in 2017 that relies on overlapping thinned-out Cu/Nb multilayers over a gap [129]. Nanoindentation tests showed a consistent hardness over the joined area [129]. Annealing tests strongly suggested that the thinned-out areas are experiencing a melting point depression [47].

An alternative method for joining metal multilayers was theorized. With the use of lasers, additives and reverse-plating, the electrodeposition can be altered in a way that allows the filling of a gap with a nanostructured lay-up to produce a joint that has no discontinuities in the layers. For a detailed description of the process, refer to the documentation in the filed patent [130]. The process is yet untested and needs a lot of work to find the necessary parameters for joining.

Chapter 8

Summary

This thesis introduced Cu/Ni Nanostructured Metal Multilayer (NMM) as a post-weld treatment method. Methods for the production of butt-welded tension specimen, for the electroplating of these specimens and the necessary investigations of these specimens have been developed.

Fatigue testing shows, for the first time, that Cu/Ni NMM increases the lifetime of notched specimens in comparison to a reference sample. The Cu/Ni coated sample of fatigue specimens is compared against reference samples consisting of as-welded specimens, machined specimens and specimens treated with conventional post-weld treatment methods. The results from the different reference samples fit in well with existing literature; the S-N curves of the different reference samples are almost congruent with the corresponding FAT classes given by engineering design standards. The S-N curves for the Cu/Ni nanolaminate coated sample show a significant lifetime increase for butt-welded tension-tension dogbone specimen. The lifetime increase between 200% and 500% is unmatched by other post-weld treatment methods. A FAT class of 190 with a slope of $k = 6$ is proposed for the design of butt-welds that are coated with Cu/Ni NMM. In comparison to other post-weld treatments, Cu/Ni NMM coatings increase the lifetime up to the yield strength of the substrate. The data suggests a fatigue limit increase of $\sim 75\%$.

Among other investigations, Scanning Electron Microscopy (SEM), Transmission Electron Microscopy (TEM), Energy-dispersive X-ray Spectroscopy (EDX) and Focused Ion Beam (FIB) serial cross-sectioning methods are used to observe the nanolaminate lay-up in the pristine and in fractured condition. These investigations expand the understanding of NMM failure mechanisms, and the observations fit in well with existing literature. Observations of the fracture mechanisms with TEM investigation of crack tips in the Cu/Ni NMM coating lead to three key mechanisms on how the NMM

coating increases the lifetime of the specimen, namely the reduction of surface roughness, the stress redistribution and the suppression of Persistent Slip Bands (PSB). From qualitative considerations and a discussion with the literature, it is hypothesized that PSB suppression is the main reason for the lifetime increase. Furthermore, prerequisites for coatings that are supposed to increase the lifetime of materials could be derived. The coating needs a good quality and adherence to the substrate. The coating material needs to have a ductile behavior and high cyclic energy absorption. In comparison to the substrate material, the coating needs to have a higher strength and lower Young's modulus. These hypotheses can be used for future research design and the optimization of fatigue life of NMM structures.

Before Cu/Ni NMM coatings can be deployed as a post-weld treatment method on a large scale, further research is necessary in different areas. Further fatigue testing is necessary to accredit the results of this thesis. The electrodeposition process needs to be scaled up to be utilized for actual structural members, and refined to consistently deliver coatings of good quality. The hypotheses raised in this study should be further investigated in order to gain a more profound understanding of the lifetime increasing influences of NMM coatings. With a better understanding and further fatigue testing, the lifetime increase of Cu/Ni NMM coatings can be optimized further.

All in all, the effectiveness of Cu/Ni NMM coatings as a post-weld treatment has been shown with the results from fatigue testing and the understanding of NMM failure mechanisms and factors for the lifetime increase of NMM coated materials has been extended by i.a. SEM, TEM and EDX investigations.

Bibliography

[1] European Commission. Directorate-General for Internal Market, Industry, Entrepreneurship and SMEs, "Discussion paper: State of infrastructure maintenance", 2019.

[2] FIEC - European Cronstruction Industry Federation, "FIEC input to the future european strategy for a sustainable and smart mobility", 2020.

[3] M. V. Biezma and F. Schanack, "Collapse of steel bridges", *Journal of Performance of Constructed Facilities*, vol. 21, no. 5, pp. 398–405, 2007.

[4] J. Schijve, *Fatigue of Structures and Materials*. Dordrecht: Springer Netherlands, 2009.

[5] Wiss, Janney, Elstner Associates Inc, "I-40 Hernando de Soto bridge fracture investigation: Final report", 2021.

[6] J. Rymsza, "Causes of the collapse of the Polcevera Viaduct in Genoa, Italy", *Applied Sciences*, vol. 11, no. 17, p. 8098, 2021.

[7] N. Rania, I. Coppola, F. Martorana, and L. Migliorini, "The collapse of the Morandi Bridge in Genoa on 14 august 2018: A collective traumatic event and its emotional impact linked to the place and loss of a symbol", *Sustainability*, vol. 11, no. 23, p. 6822, 2019.

[8] B. Pakenham, A. Ermakova, and A. Mehmanparast, "A review of life extension strategies for offshore wind farms using techno-economic assessments", *Energies*, vol. 14, no. 7, p. 1936, 2021.

[9] European Commission Joint Research Centre, K. Gkoumas, M. Balen, M. Grosso, F. Pekár, F. L. Marques Dos Santos, G. Haq, A. Ortega Hortelano, and A. Tsakalidis, *Research and innovation in bridge maintenance, inspection and monitoring: A European perspective based on the Transport Research and Innovation Monitoring and Information System (TRIMIS)*. Publications Office, 2019.

[10] M. Aliofkhazraei, F. C. Walsh, G. Zangari, H. Köçkar, M. Alper, C. Rizal, L. Magagnin, V. Protsenko, R. Arunachalam, A. Rezvanian, A. Moein, S. Assareh, and M. H. Allahyarzadeh, "Development of electrodeposited multilayer coatings: A review of fabrication, microstructure, properties and applications", *Applied Surface Science Advances*, vol. 6, p. 100141, 2021.

[11] A. Sáenz-Trevizo and A. M. Hodge, "Nanomaterials by design: a review of nanoscale metallic multilayers", *Nanotechnology*, vol. 31, no. 29, p. 292002, 2020.

[12] I. Freestone, N. Meeks, M. Sax, and C. Higgitt, "The Lycurgus Cup — a roman nanotechnology", *Gold Bulletin*, vol. 40, no. 4, pp. 270–277, 2007.

[13] M. Reibold, P. Paufler, A. A. Levin, W. Kochmann, N. Pätzke, and D. C. Meyer, "Discovery of nanotubes in ancient damascus steel", 2009.

[14] H. K. D. H. Bhadeshia, "The first bulk nanostructured metal", *Science and technology of advanced materials*, vol. 14, no. 1, p. 014202, 2013.

[15] Woodhead, ed., *Nanostructure Control of Materials*. Elsevier, 2006.

[16] W. Deubner, "Versuche über die Reflexion von Röntgenstrahlen an einem künstlich hergestellten Schichtenkörper. (Mit 5 Figuren)", *Annalen der Physik*, vol. 397, no. 2, pp. 261–280, 1930.

[17] B. Y. Jin and J. B. Ketterson, "Artificial metallic superlattices", *Advances in Physics*, vol. 38, no. 3, pp. 189–366, 1989.

[18] I. J. Beyerlein, A. Caro, M. J. Demkowicz, N. A. Mara, A. Misra, and B. P. Uberuaga, "Radiation damage tolerant nanomaterials", *Materials Today*, vol. 16, no. 11, pp. 443–449, 2013.

[19] A. Misra, M. J. Demkowicz, X. Zhang, and R. G. Hoagland, "The radiation damage tolerance of ultra-high strength nanolayered composites", *JOM*, vol. 59, no. 9, pp. 62–65, 2007.

[20] C. Lomasney, L. Collinson, and T. Burnett, "Developments in nanolaminated materials to enhance the performance and longevity of metal components in offshore applications", in *All Days*, OTC, 05042015.

[21] J. Leppäniemi, P. Sippola, M. Broas, J. Aromaa, H. Lipsanen, and J. Koskinen, "Corrosion protection of steel with multilayer coatings: Improving the sealing properties of physical vapor deposition CrN coatings with Al_2O_3/TiO_2 atomic layer deposition nanolaminates", *Thin Solid Films*, vol. 627, pp. 59–68, 2017.

[22] L. Elias and A. Chitharanjan Hegde, "Electrodeposition of laminar coatings of Ni-W alloy and their corrosion behaviour", *Surface and Coatings Technology*, vol. 283, pp. 61–69, 2015.

[23] M. Verdier, M. Niewczas, J. D. Embury, M. Hawley, M. Nastasi, and H. Kung, "Plastic behaviour of Cu/Ni multilayers", *MRS Online Proceedings Library*, vol. 522, no. 1, pp. 77–82, 1998.

[24] J. Wang, Q. Zhou, S. Shao, and A. Misra, "Strength and plasticity of nanolaminated materials", *Materials Research Letters*, vol. 5, no. 1, pp. 1–19, 2017.

[25] B. M. Clemens, H. Kung, and S. A. Barnett, "Structure and strength of multilayers", *MRS Bulletin*, vol. 24, no. 2, pp. 20–26, 1999.

[26] Y. C. Wang, A. Misra, and R. G. Hoagland, "Fatigue properties of nanoscale Cu/Nb multilayers", *Scripta Materialia*, vol. 54, no. 9, pp. 1593–1598, 2006.

[27] M. Stoudt, R. Ricker, and R. Cammarata, "The influence of a multilayered metallic coating on fatigue crack nucleation", *International Journal of Fatigue*, vol. 23, pp. 215–223, 2001.

[28] G. Was and T. Foecke, "Deformation and fracture in microlaminates", *Thin Solid Films*, vol. 286, no. 1–2, pp. 1–31, 1996.

[29] M. Nasim, Y. Li, M. Wen, and C. Wen, "A review of high-strength nanolaminates and evaluation of their properties", *Material Science and Technology*, vol. 50, no. 1, pp. 215–244, 2020.

[30] A. Misra, M. Verdier, Y. C. Lu, H. Kung, T. E. Mitchell, M. Nastasi, and J. D. Embury, "Structure and mechanical properties of Cu-X(X=Nb,Cr,Ni) nanolayered composites", *Scripta Materialia*, vol. 39, no. 4–5, pp. 555–560, 1998.

[31] A. Misra, "Mechanical behavior of metallic nanolaminates", in *Nanostructure Control of Materials* (Woodhead, ed.), pp. 146–176, Elsevier, 2006.

[32] P. M. Anderson and C. Li, "Hall-Petch relations for multilayered materials", *Nanostructured Materials*, vol. 5, no. 3, pp. 349–362, 1995.

[33] W. M. C. Yang, T. Tsakalakos, and J. E. Hilliard, "Enhanced elastic modulus in composition-modulated gold-nickel and copper-palladium foils", *Journal of Applied Physics*, vol. 48, no. 3, pp. 876–879, 1977.

[34] J. Wang, R. G. Hoagland, and A. Misra, "Mechanics of nanoscale metallic multilayers: From atomic-scale to micro-scale", *Scripta Materialia*, vol. 60, no. 12, pp. 1067–1072, 2009.

[35] J. S. Carpenter, A. Misra, and P. M. Anderson, "Achieving maximum hardness in semi-coherent multilayer thin films with unequal layer thickness", *Acta Materialia*, vol. 60, no. 6–7, pp. 2625–2636, 2012.

[36] E. R. Kreidler and P. M. Anderson, "Orowan-based deformation model for layered metallic materials", *MRS Online Proceedings Library*, vol. 434, 1996.

[37] A. Misra, J. P. Hirth, and H. Kung, "Single-dislocation-based strengthening mechanisms in nanoscale metallic multilayers", *Philosophical Magazine A*, vol. 82, no. 16, pp. 2935–2951, 2002.

[38] V. A. Lubarda, "Dislocation burgers vector and the Peach–Koehler force: a review", *Journal of Materials Research and Technology*, vol. 8, no. 1, pp. 1550–1565, 2019.

[39] A. Misra, J. P. Hirth, and R. G. Hoagland, "Length-scale-dependent deformation mechanisms in incoherent metallic multilayered composites", *Acta Materialia*, vol. 53, no. 18, pp. 4817–4824, 2005.

[40] A. Misra, M. J. Demkowicz, J. Wang, and R. G. Hoagland, "The multiscale modeling of plastic deformation in metallic nanolayered composites", *JOM*, vol. 60, no. 4, pp. 39–42, 2008.

[41] W.-R. Jian, S. Xu, Y. Su, and I. J. Beyerlein, "Role of layer thickness and dislocation distribution in confined layer slip in nanolaminated Nb", *International Journal of Plasticity*, vol. 152, p. 103239, 2022.

[42] I. N. Mastorakos, A. Bellou, D. F. Bahr, and H. M. Zbib, "Size-dependent strength in nanolaminate metallic systems", *Journal of Materials Research*, vol. 26, no. 10, pp. 1179–1187, 2011.

[43] R. G. Hoagland, R. J. Kurtz, and C. H. Henager, "Slip resistance of interfaces and the strength of metallic multilayer composites", *Scripta Materialia*, vol. 50, no. 6, pp. 775–779, 2004.

[44] C. D. Appleget, J. S. Riano, and A. M. Hodge, "An overview of nano multilayers as model systems for developing nanoscale microstructures", *Materials (Basel, Switzerland)*, vol. 15, no. 1, 2022.

[45] G. Kaptay, J. Janczak-Rusch, and L. P. H. Jeurgens, "Melting point depression and fast diffusion in nanostructured brazing fillers confined between barrier nanolayers", *Journal of Materials Engineering and Performance*, vol. 25, no. 8, pp. 3275–3284, 2016.

[46] M. Czagány, D. Varanasi, A. Sycheva, D. Janovszky, D. Koncz-Horváth, F. Kristaly, P. Baumli, and G. Kaptay, "Synthesis, characterisation and thermal behaviour of Cu-based nano-multilayer", *Journal of Materials Science*, vol. 56, no. 13, pp. 7823–7839, 2021.

[47] J. Brunow, M. Ritter, T. Krekeler, M. Ramezani, and M. Rutner, "Thermal stability of a nanolayered metal joint", *Scripta Materialia*, vol. 194, p. 113687, 2021.

[48] S. Zheng, I. J. Beyerlein, J. S. Carpenter, K. Kang, J. Wang, W. Han, and N. A. Mara, "High-strength and thermally stable bulk nanolayered composites due to twin-induced interfaces", *Nature Communications*, vol. 4, no. 1, p. 1696, 2013.

[49] E. Kulej, B. Kucharska, G. Pyka, and M. Gwoździk, "Characterization of the surface topography and nano-hardness of Cu/Ni multilayer structures", *Open Physics*, vol. 9, no. 6, 2011.

[50] X. Y. Zhu, X. J. Liu, R. L. Zong, F. Zeng, and F. Pan, "Microstructure and mechanical properties of nanoscale Cu/Ni multilayers", *Materials Science and Engineering: A*, vol. 527, no. 4–5, pp. 1243–1248, 2010.

[51] Z. Liu, M. A. Monclús, L. W. Yang, M. Castillo-Rodríguez, J. M. Molina-Aldareguía, and J. LLorca, "Tensile deformation and fracture mechanisms of Cu/Nb nanolaminates studied by in situ TEM mechanical tests", *Extreme Mechanics Letters*, vol. 25, pp. 60–65, 2018.

[52] T. J. Foecke and D. E. Kramer, "In situ TEM observations of fracture in nanolaminated metallic thin films", *International Journal of Fatigue*, vol. 119, no. 4–2, pp. 351–357, 2003.

[53] L. R. Brandt, E. Salvati, C. Papadaki, H. Zhang, S. Ying, E. Le Bourhis, I. Dolbnya, T. Sui, and A. M. Korsunsky, "Probing the deformation and fracture properties of Cu/W nano-multilayers by in situ SEM and synchrotron XRD strain microscopy", *Surface and Coatings Technology*, vol. 320, pp. 158–167, 2017.

[54] J. S. Carpenter, A. Misra, M. D. Uchic, and P. M. Anderson, "Strain rate sensitivity and activation volume of Cu/Ni metallic multilayer thin films measured via micropillar compression", *Applied Physics Letters*, vol. 101, no. 5, p. 051901, 2012.

[55] A. S. Budiman, R. Sahay, H. P. Anwar Ali, S. K. Tippabhotla, I. Radchenko, and N. Raghavan, "Interface-mediated plasticity and fracture in nanoscale Cu/Nb multilayers as revealed by in situ clamped microbeam bending", *Materials Science and Engineering: A*, vol. 803, p. 140705, 2021.

[56] D. Tench and J. White, "Enhanced tensile strength for electrodeposited nickel-copper multilayer composites", *Metallurgical and Materials Transactions A*, vol. 15, no. 11, pp. 2039–2040, 1984.

[57] J. M. Wheeler and A. G. Gunner, "Analysis of failure modes under nano-impact fatigue of coatings via high-speed sampling", *Surface and Coatings Technology*, vol. 232, pp. 264–268, 2013.

[58] M. Berdova, T. Ylitalo, I. Kassamakov, J. Heino, P. T. Törmä, L. Kilpi, H. Ronkainen, J. Koskinen, E. Hæggström, and S. Franssila, "Mechanical assessment of suspended ALD thin films by bulge and shaft-loading techniques", *Acta Materialia*, vol. 66, pp. 370–377, 2014.

[59] R. L. Schoeppner, G. Mohanty, M. N. Polyakov, L. Petho, X. Maeder, and J. Michler, "An exploratory study on strengthening and thermal stability of magnetron sputtered w nanoparticles at the interface of Cu/Ni multilayer films", *Materials & Design*, vol. 195, p. 108907, 2020.

[60] C. Gang, W. ChuanJie, and Z. Peng, "The role of interface in uniaxial tensile process of nano-scale bilayer Cu/Ni", *Computational Materials Science*, vol. 131, pp. 21–27, 2017.

[61] B. Zhang, Y. Kou, Y. Y. Xia, and X. Zhang, "Modulation of strength and plasticity of multiscale Ni/Cu laminated composites", *Materials Science and Engineering: A*, vol. 636, pp. 216–220, 2015.

[62] D. M. Tench and J. T. White, "Tensile properties of nanostructured Ni-Cu multilayered materials prepared by electrodeposition", *Journal of The Electrochemical Society*, vol. 138, no. 12, pp. 3757–3758, 1991.

[63] S. Menezes and D. P. Anderson, "Wavelength-property correlation in electrodeposited ultrastructured Cu-Ni multilayers", *Journal of The Electrochemical Society*, vol. 137, no. 2, pp. 440–444, 1990.

[64] Y. Sun, Y. Chen, N. Tsuji, and S. Guan, "Microstructural evolution and mechanical properties of nanostructured Cu/Ni multilayer fabricated by accumulative roll bonding", *Journal of Alloys and Compounds*, vol. 819, p. 152956, 2020.

[65] Y. Kaneko, Y. Nishijima, T. Sanda, and S. Hashimoto, "Fatigue life enhancement by surface coating of Ni/Cu multilayered films", in *PRICM 6* (Y. W. Chang, ed.), Materials science forum, (Stafa-Zurich), pp. 2393–2398, Trans Tech Publ, 2007.

[66] Y. C. Qian, J. Tan, H. J. Yang, and Z. X. Hu, "Brush plated multilayered Cu/Ni coating from a single electrolyte and its fretting wear behaviors", *Advanced Materials Research*, vol. 97-101, pp. 1467–1470, 2010.

[67] X. Zhang, D. Liu, X. Li, H. Dong, and Y. Xi, "The effect of modulation ratio of Cu/Ni multilayer films on the fretting damage behaviour of Ti-811 titanium alloy", *Materials*, vol. 10, no. 6, 2017.

[68] J. Brunow and M. Rutner, "Das Nanolaminatpflaster – Schweißnahtnachbehandlung für bisher unerreichte Lebensdauerverlängerung", *Stahlbau*, vol. 90, no. 9, pp. 691–700, 2021.

[69] N. Kanani, *Galvanotechnik: Grundlagen, Verfahren und Praxis einer Schlüsseltechnologie*. München: Hanser, 3., aktualisierte auflage ed., 2020.

[70] M. Schlesinger and M. Paunović, eds., *Modern Electroplating*. Electrochemical Society Series, New York, NY: John Wiley & Sons, 5., auflage ed., 2011.

[71] T. W. Jelinek, *Praktische Galvanotechnik: Ein Lehr- und Handbuch*. Lehrbuchreihe Galvanotechnik, Bad Saulgau: Leuze, 7., aktualisierte ed., 2013.

[72] Y. D. Gamburg and G. Zangari, *Theory and practice of metal electrodeposition*. New York, NY and Heidelberg: Springer, 2011.

[73] N. Kanani, *Electroplating: Basic principles, processes and practice*. Kidlington: Elsevier, reprinted 2006 ed., 2004.

[74] G.-F. Wang, L.-D. Shen, L.-M. Dou, and Z.-D. Liu, "Research on preparation of multilayers by the multiple jet electrodeposition", *International Journal of Electrochemichal Science*, vol. 2014, no. 9, pp. 220–226, 2013.

[75] K. Wasa, ed., *Handbook of sputter deposition technology: Fundamentals and applications for functional thin films, nanomaterials, and MEMS*. Amsterdam: Elsevier, 2nd ed., 2012.

[76] J. Sarkar, *Sputtering Materials for VLSI and Thin Film Devices*. Norwich: William Andrew, 2014.

[77] J. Ni, J. Li, J. Jian, J. He, H. Chen, X. Leng, and X. Liu, "Recent studies on the fabrication of multilayer films by magnetron sputtering and their irradiation behaviors", *Coatings*, vol. 11, no. 12, p. 1468, 2021.

[78] I. G. McDonald, W. M. Moehlenkamp, D. Arola, and J. Wang, "Residual stresses in Cu/Ni multilayer thin films measured using the Sin2Phi method", *Experimental Mechanics*, vol. 59, no. 1, pp. 111–120, 2019.

[79] Y. Saito, H. Utsunomiya, N. Tsuji, and T. Sakai, "Novel ultra-high straining process for bulk materials – development of the accumulative roll-bonding (ARB) process", *Acta Materialia*, vol. 47, no. 2, pp. 579–583, 1999.

[80] J. S. Carpenter, T. Nizolek, R. J. McCabe, M. Knezevic, S. J. Zheng, B. P. Eftink, J. E. Scott, S. C. Vogel, T. M. Pollock, N. A. Mara, and I. J. Beyerlein, "Bulk texture evolution of nanolamellar Zr–Nb composites processed via accumulative roll bonding", *Acta Materialia*, vol. 92, pp. 97–108, 2015.

[81] J. S. Carpenter, S. C. Vogel, J. E. LeDonne, D. L. Hammon, I. J. Beyerlein, and N. A. Mara, "Bulk texture evolution of Cu–Nb nanolamellar composites during accumulative roll bonding", *Acta Materialia*, vol. 60, no. 4, pp. 1576–1586, 2012.

[82] P. Paris and F. Erdogan, "A critical analysis of crack propagation laws", *Journal of Basic Engineering*, vol. 85, no. 4, pp. 528–533, 1963.

[83] D. Radaj, C. M. Sonsino, and W. Fricke, *Fatigue assessment of welded joints by local approaches*. Woodhead Publishing in materials, Cambridge and Boca Raton and Boston: Woodhead Publ and CRC, 2nd ed., 2006.

[84] DIN EN 1993-1-9:2010-12, "Eurocode 3: Bemessung und Konstruktion von Stahlbauten - Teil 1-9: Ermüdung", 2010.

[85] A. F. Hobbacher, *Recommendations for Fatigue Design of Welded Joints and Components*, vol. IIW-2259-15. Cham: Springer International Publishing, 2nd ed., 2016.

[86] P. Lukáš and L. Kunz, "Role of persistent slip bands in fatigue", *Philosophical Magazine*, vol. 84, no. 3–5, pp. 317–330, 2004.

[87] J. A. Ewing and J. C. W. Humfrey, "The fracture of metals under repeated alternations of stress", *Philosophical Transactions of the Royal Society of London. Series A, Containing Papers of a Mathematical or Physical Character*, vol. 200, no. 321–330, pp. 241–250, 1903.

[88] J. Polák, V. Mazánová, M. Heczko, R. Petráš, I. Kuběna, L. Casalena, and J. Man, "The role of extrusions and intrusions in fatigue crack initiation", *Engineering Fracture Mechanics*, vol. 185, pp. 46–60, 2017.

[89] V. Chmelko, M. Margetin, and M. Harakal', "Notch effect of welded joint", *MATEC Web of Conferences*, vol. 165, p. 21003, 2018.

[90] B. Schork, U. Zerbst, Y. Kiyak, M. Kaffenberger, M. Madia, and M. Oechsner, "Effect of the parameters of weld toe geometry on the FAT class as obtained by means of fracture mechanics-based simulations", *Welding in the World*, vol. 64, no. 6, pp. 925–936, 2020.

[91] K. J. Kirkhope, R. Bell, L. Caron, R. I. Basu, and K.-T. Ma, "Weld detail fatigue life improvement techniques. part 1: review", *Marine Structures*, vol. 12, no. 6, pp. 447–474, 1999.

[92] G. B. Marquis and Z. Barsoum, *IIW Recommendations for the HFMI Treatment: For Improving the Fatigue Strength of Welded Joints*. IIW Collection, Singapore and s.l.: Springer Singapore, 2016.

[93] P. J. Haagensen and S. J. Maddox, "IIW recommendations on methods for improving the fatigue strength of welded joints: Iiw-2142-10",

[94] DASt Richtlinie 026, *Ermüdungsbemessung bei Anwendung höherfrequenter Hämmerverfahren*, vol. 026 of *DASt-Richtlinien*. Düsseldorf: Stahlbau, 2019.

[95] U. Kuhlmann, ed., *Stahlbau-Kalender 2021: Brücken, Neue Eurocode-Generation*, vol. 23. Jahrgang of *Wiley Online Library*. Berlin: Wilhelm Ernst & Sohn, 2021.

[96] S. Breunig, L.-M. Gölz, U. Kuhlmann, P. Weidner, and T. Ummenhofer, "DASt–Richtlinie zum höherfrequenten Hämmern", in *Stahlbau-Kalender 2021* (U. Kuhlmann, ed.), Wiley Online Library, pp. 435–470, Berlin: Wilhelm Ernst & Sohn, 2021.

[97] R. Aldén, Z. Barsoum, T. Vouristo, and M. Al-Emrani, "Robustness of the HFMI techniques and the effect of weld quality on the fatigue life improvement of welded joints", *Welding in the World*, vol. 64, no. 11, pp. 1947–1956, 2020.

[98] L. Suominen, M. Khurshid, and J. Parantainen, "Residual stresses in welded components following post-weld treatment methods", *Procedia Engineering*, vol. 66, pp. 181–191, 2013.

[99] J. Brunow, S. Gries, T. Krekeler, and M. Rutner, "Material mechanisms of Cu/Ni nanolaminate coatings resulting in lifetime extensions of welded joints", *Scripta Materialia*, vol. 212, p. 114501, 2022.

[100] H. C. Yildirim and G. B. Marquis, "Fatigue strength improvement factors for high strength steel welded joints treated by high frequency mechanical impact", *International Journal of Fatigue*, vol. 44, pp. 168–176, 2012.

[101] DIN 50125:2016-12, "Prüfung metallischer Werkstoffe- Zugproben", 2016.

[102] DIN 50100:2016-12, "Schwingfestigkeitsversuch - Durchführung und Auswertung von zyklischen Versuchen mit konstanter Lastamplitude für metallische Werkstoffproben und Bauteile", 2016.

[103] E08 Committee, "Standard practice for conducting force controlled constant amplitude axial fatigue tests of metallic materials", 2021.

[104] E08 Committee, "Standard test method for strain-controlled fatigue testing", 2021.

[105] DIN EN ISO 6520-1:2007-11, "Schweißen und verwandte Prozesse – Einteilung von geometrischen Unregelmäßigkeiten an metallischen Werkstoffen: Teil 1: Schmelzschweißen", 2007-11.

[106] DVS Merkblatt 2403, "Empfehlungen für die Durchführung, Auswertung und Dokumentation von Schwingfestigkeitsversuchen an Schweißverbindungen", *Schweißen und Schneiden*, vol. 2020, no. 9, p. 587, 2020.

[107] DIN EN ISO 6892-1:2020-06, "Metallische Werkstoffe – Zugversuch – Teil 1: Prüfverfahren bei Raumtemperatur", 2020-06.

[108] QATM, ed., *Expert Guide Materialographie / Metallographie: Leitfaden für den Praktiker und Einsteiger: Tipps & Tricks: Vermeidung von Artefakten: von der Probenentnahme bis zum fertigen Schliff*. Mammelzen: QATM Akademie, 1st ed., 2020.

[109] C. Bonhôte and D. Landolt, "Microstructure of NiCu multilayers electrodeposited from a citrate electrolyte", *Electrochimica Acta*, vol. 42, no. 15, pp. 2407–2417, 1997.

[110] DIN 50957-1:2016-02, "Prüfung galvanischer Bäder – Galvanisierungsprüfung: Teil 1: Standard-Hull-Zelle", 2016.

[111] Y. V. Ivshin, F. N. Shaikhutdinova, and V. A. Sysoev, "Electrodeposition of copper on mild steel: Peculiarities of the process", *Surface Engineering and Applied Electrochemistry*, vol. 54, no. 5, pp. 452–458, 2018.

[112] D. R. Gabe, "The role of hydrogen in metal electrodeposition processes", *Journal of Applied Electrochemistry*, vol. 27, no. 8, pp. 908–915, 1997.

[113] M. Braun and X. Wang, "A review of fatigue test data on weld toe grinding and weld profiling", *International Journal of Fatigue*, vol. 145, p. 106073, 2021.

[114] I. Radchenko, H. P. Anwarali, S. K. Tippabhotla, and A. S. Budiman, "Effects of interface shear strength during failure of semicoherent metal–metal nanolaminates: An example of accumulative roll-bonded Cu/Nb", *Acta Materialia*, vol. 156, pp. 125–135, 2018.

[115] D. R. Bloyer, R. O. Ritchie, and K. T. Venkateswara Rao, "Fatigue-crack propagation behavior of ductile/brittle laminated composites", *Metallurgical and Materials Transactions A*, vol. 30, no. 3, pp. 633–642, 1999.

[116] Y. Q. Wang, R. Fritz, D. Kiener, J. Y. Zhang, G. Liu, O. Kolednik, R. Pippan, and J. Sun, "Fracture behavior and deformation mechanisms in nanolaminated crystalline/amorphous micro-cantilevers", *Acta Materialia*, vol. 180, pp. 73–83, 2019.

[117] M. S. Dodaran, J. Wang, N. Shamsaei, and S. Shao, "Investigating the interaction between persistent slip bands and surface hard coatings via crystal plasticity simulations", *Crystals*, vol. 10, no. 11, p. 1012, 2020.

[118] M. Grabe, C. Ullerich, M. Wenner, and M. Herbrand, "smartBridge Hamburg – prototypische Pilotierung eines digitalen Zwillings", *Bautechnik*, vol. 97, no. 2, pp. 118–125, 2020.

[119] N. Spalek, M. Rutner, and J. Brunow, "Entwicklung eines Prototypen zur Nanolaminatbeschichtung: C4T – Forschungsbericht", Technische Universität Hamburg, *unpublished document*, 2022.

[120] G. Genchi, A. Carocci, G. Lauria, M. S. Sinicropi, and A. Catalano, "Nickel: Human health and environmental toxicology", *International Journal of Environmental Research and Public Health*, vol. 17, no. 3, 2020.

[121] DIN EN ISO 8501-1:2007-12, "Vorbereitung von Stahloberflächen vor dem Auftragen von Beschichtungsstoffen – Visuelle Beurteilung der Oberflächenreinheit – Teil 1: Rostgrade und Oberflächenvorbereitungsgrade von unbeschichteten

Stahloberflächen und Stahloberflächen nach ganzflächigem Entfernen vorhandener Beschichtungen", 2007.

[122] ASTM E647:2016-12, "Test method for measurement of fatigue crack growth rates", 2016.

[123] O. Kraft, "Thin films: Mechanical testing", in *Encyclopedia of Materials: Science and Technology* (K.H.J. Buschow, R. W. Cahn, M.C. Flemings, B. Ilschner, E.J. Kramer, S. Mahajan, and P. Veyssière, eds.), pp. 9257–9261, Elsevier, 2001.

[124] Z. Fu, L. Jiang, J. L. Wardini, B. E. MacDonald, H. Wen, W. Xiong, D. Zhang, Y. Zhou, T. J. Rupert, W. Chen, and E. J. Lavernia, "A high-entropy alloy with hierarchical nanoprecipitates and ultrahigh strength", *Science advances*, vol. 4, no. 10, p. eaat8712, 2018.

[125] D. Kiener and A. M. Minor, "Source truncation and exhaustion: insights from quantitative in situ TEM tensile testing", *Nano letters*, vol. 11, no. 9, pp. 3816–3820, 2011.

[126] M. Stolarska, D. L. Chopp, N. Moës, and T. Belytschko, "Modelling crack growth by level sets in the extended finite element method", *International Journal for Numerical Methods in Engineering*, vol. 51, no. 8, pp. 943–960, 2001.

[127] K. Nasri, M. Abbadi, M. Zenasni, M. Ghammouri, and Z. Azari, "Double crack growth analysis in the presence of a bi-material interface using XFEM and FEM modelling", *Engineering Fracture Mechanics*, vol. 132, pp. 189–199, 2014.

[128] K. Nasri and M. Zenasni, "Fatigue crack growth simulation in coated materials using X-FEM", *Comptes Rendus Mécanique*, vol. 345, no. 4, pp. 271–280, 2017.

[129] M. G. Ramezani, M. J. Demkowicz, G. Feng, and M. P. Rutner, "Joining of physical vapor-deposited metal nano-layered composites", *Scripta Materialia*, vol. 139, pp. 114–118, 2017.

[130] M. P. Rutner and J. Brunow, "Verfahren zum Fügen von Nanolaminaten mittels galvanischer Metallabscheidung: DE202010133582", *European Patent Office*, 2022.

Appendix A

List of Fatigue Specimens

The following table lists all dogbone specimens that have been tested for the fatigue evaluation in chapter 5.

Sample Name	Group	Date	Comment	R	$\Delta F/F_{yset}$	ΔF_{set} [kN]	$\Delta\sigma_{set}$ [N/mm²]	N_{cr}	Failure
A1	monoton	29.07.2021		0	1	73,74	368,7	1	b
A2	monoton	29.07.2021		0	1	74,9	374,5	1	b
A3	monoton	29.07.2021		0	1	74,03	370,2	1	b
A4	coated	22.09.2021		0	0,9	65,7	328,5	98034	r
A5	coated	14.03.2022		0	0,9	65,7	328,5	175920	w
A6	burrgrinding	26.11.2021		0	0,75	54,75	273,8	524955	b
A7	burrgrinding	09.09.2021		0	0,75	54,75	273,8	184242	b
A8	machined			0	0,95	69,35	346,8	73845	r
A9	machined			0	0,9	65,7	328,5	43018	r
A10	burrgrinding	25.11.2021		0	0,85	62,05	310,3	106462	b
A11	coated		untested						
A12	reference	19.06.2021		0	0,95	69,35	346,8	128529	w
B1	reference	01.11.2021		0	0,95	69,35	346,8	24989	r
B2	reference	01.11.2021		0	0,9	65,7	328,5	28229	r
B3	reference	01.11.2021		0	0,85	62,05	310,3	67223	b
B4	coated		Westhagemann						
B5	HiFIT	17.09.2021		0	0,55	40,15	200,8	248500	r
B6	HiFIT	23.11.2021		0	0,65	47,45	237,3	169719	r
B7	burrgrinding	28.11.2021		0	0,65	47,45	237,3	276766	r
B8	reference	23.08.2021		0	0,85	62,05	310,3	171249	w
B9	reference	02.11.2021		0	0,8	58,4	292	124869	w
B10	burrgrinding	09.09.2021		0	0,95	69,35	346,8	53593	r
B11	nanolaminate	02.05.2022	deviant lay-up Z1	0	0,9	65,7	328,5	236245	w
B12	reference	06.09.2021		0	0,9	65,7	328,5	128454	w
C1	reference	02.11.2021		0	0,75	54,75	273,8	40940	w
C2	reference	03.11.2021		0	0,7	51,1	255,5	205470	w
C3	coated	21.09.2021		0	0,85	62,05	310,3	81332	w
C4	machined	21.01.2022	stopped?	0	0,9	65,7	328,5	15992	w
C5	HiFIT	17.11.2021		0	0,95	69,35	346,8	46305	w
C6	HiFIT	15.09.2021		0	0,65	47,45	237,3	109397	r
C7	burrgrinding	20.09.2021		0	0,65	47,45	237,3	193404	w
C8	reference	06.09.2021		0	0,8	58,4	292	91672	w
C9	reference	22.06.2022	pre stressed at 75 kN	0	0,75	54,75	273,8	222105	w
C10	burrgrinding	13.12.2021		0	0,75	54,75	273,8	140826	b
C11	machined	08.06.2022		0	0,7	51,1	255,5	111446	w
C12	reference	24.08.2021		0	0,75	54,75	273,8	148438	b
D1	reference	04.11.2021		0	0,65	47,45	237,3	155551	w
D2	reference	04.11.2021		0	0,6	43,8	219	237338	w
D3	reference	05.11.2021		0	0,55	40,15	200,8	1546309	r
D4	machined	08.06.2022		0	0,5	36,5	182,5	1025846	r
D5	HiFIT	19.11.2021		0	0,75	54,75	273,8	118821	w
D6	HiFIT	14.09.2021		0	0,75	54,75	273,8	176078	w
D7	burrgrinding	24.11.2021		0	0,95	69,35	346,8	95340	b
D8	reference	02.09.2021		0	0,3	21,9	109,5	3722983	o
D9	reference	09.11.2021		0	0,5	36,5	182,5	228067	w
D10	burrgrinding	09.09.2021		0	0,85	62,05	310,3	62339	r
D11	machined	08.06.2022		0	0,5	36,5	182,5	409103	r
D12	reference	25.08.2021		0	0,65	47,45	237,3	164433	w
E1	reference	15.11.2021		0	0,4	29,2	146	4140125	o
E2	reference	01.12.2021		0	0,95	69,35	346,8	34980	w
E3	reference	02.12.2021		0	0,9	65,7	328,5	62332	b
E4	machined	08.06.2022		0	0,75	54,75	273,8	133198	b
E5	HiFIT	24.11.2021		0	0,55	40,15	200,8	306248	b
E6	HiFIT	07.09.2021		0	0,85	62,05	310,3	300181	w

Sample Name	Group	Date	Comment	R	$\Delta F/F_{yset}$	ΔF_{set} [kN]	$\Delta\sigma_{set}$ [N/mm²]	N_{cr}	Failure
E7	burrgrinding	10.12.2021		0	0,85	62,05	310,3	94439	w
E8	reference	21.09.2021		0	0,6	43,8	219	231225	w
E9	reference	02.12.2021		0	0,85	62,05	310,3	62364	w
E10	burrgrinding	20.09.2021		0	0,55	40,15	200,8	2750000	o
E11	coated	30.09.2021		0	0,8	58,4	292	104439	w
E12	reference	26.08.2021		0	0,55	40,15	200,8	765195	w
F1	reference	09.12.2021		0	0,75	54,75	273,8	173753	b
F2	reference	03.12.2021		0	0,7	51,1	255,5	123118	w
F3	reference	04.12.2021		0	0,55	40,15	200,8	301080	w
F4	coated	23.09.2021		0	0,85	62,05	310,3	96312	w
F5	HiFIT	18.11.2021		0	0,85	62,05	310,3	146538	w
F6	HiFIT	07.09.2022		0	0,95	69,35	346,8	80974	w
F7	burrgrinding	09.12.2021		0	0,95	69,35	346,8	65040	w
F8	reference	22.09.2021		0	0,5	36,5	182,5	294216	w
F9	reference	09.12.2021		0	0,9	65,7	328,5	40994	w
F10	burrgrinding	29.11.2021		0	0,55	40,15	200,8	528581	w
F11	machined	08.06.2022		0	0,85	62,05	310,3	69107	w
F12	reference	30.08.2021		0	0,4	29,2	146	866913	w
G1	reference	15.07.2022		0	0,9	65,7	328,5	183374	w
G2	VAM	N/A	unclear load situation	0	0,9	65,7	328,5	307000	w
G3	nanolaminate	09.05.2022		0	0,7	51,1	255,5	694254	w
G4	nanolaminate	06.05.2022	delaminations during clamping	0	0,9	65,7	328,5	115039	w
G5	nanolaminate	28.06.2022		0	0,75	54,75	273,8	701967	w
G6	corrosion								
G7	machined	24.08.2022		0	0,8	58,4	292	493551	w
G8	machined	17.06.2022		0	0,7	51,1	255,5	2737710	o
G9	VAM	N/A	unclear load situation	0	0,9	65,7	328,5	219000	w
G10	prestressed	13.06.2022	pre stressed at 75 kN	0	0,7	51,1	255,5	2680764	o
G11	reference	01.07.2022		0	0,75	54,75	273,8	326780	w
G12	VAM	N/A	unclear load situation	0	0,9	65,7	328,5	175000	w
G13	VAM	N/A	unclear load situation	0	0,9	65,7	328,5	303788	w
G14	VAM	N/A	unclear load situation	0	0,9	65,7	328,5	296000	w
G15	VAM	N/A	unclear load situation	0	0,9	65,7	328,5	252000	w
G16	VAM	N/A	unclear load situation	0	0,9	65,7	328,5	268000	w
G17	nanolaminate	29.06.2022		0	0,85	62,05	310,3	207895	w
G18	nanolaminate	02.08.2022		0	0,8	58,4	292	254643	w
G19	corrosion	07.09.2022		0	0,7	51,1	255,5	203834	w
G20	corrosion								
G21	corrosion								
G22	reference	04.08.2022		0	0,85	62,05	310,3	115287	w
G23	corrosion								
G24	reference	12.08.2022		0	0,7	51,1	255,5	177883	w
G25	VAM	N/A	unclear load situation	0	0,9	65,7	328,5	92696	w
G26	machined	25.08.2022		0	0,85	62,05	310,3	301883	w
G27	VAM	N/A	unclear load situation	0	0,9	65,7	328,5	139627	w
G28	VAM	N/A	unclear load situation	0	0,9	65,7	328,5	128950	w
G29	VAM	N/A	unclear load situation	0	0,9	65,7	328,5	124037	w
G30	corrosion	12.09.2022		0	0,5	36,5	182,5	456461	w
G31	monoton	18.02.2022							
G32	prestressed	08.06.2022	pre stressed at 75 kN	0	0,6	43,8	219	3355157	o
G33	nanolaminate	13.05.2022	delaminations during clamping	0	0,7	51,1	255,5	568145	w
G34	machined	10.08.2022		0	0,9	65,7	328,5	238067	w
G35	corrosion								
G36	reference	04.07.2022		0	0,8	58,4	292	59612	w

Sample Name	Group	Date	Comment	R	$\Delta F/F_{yset}$	ΔF_{set} [kN]	$\Delta\sigma_{set}$ [N/mm²]	N_{cr}	Failure
G37	nanolaminate	25.05.2022	pre stressed at 75 kN	0	0,6	43,8	219	2500000	o
G38	nanolaminate	04.08.2022		0	0,65	47,45	237,3	2500000	o
G39	corrosion								
G40	corrosion								
G41	nanolaminate	02.06.2022	pre stressed at 75 kN	0	0,6	43,8	219	4262779	o
G42	nanolaminate	31.05.2022	deviant lay-up	0	0,8	58,4	292	836932	c
G43	nanolaminate	27.07.2022		0	0,8	58,4	292	324080	b
11	reference	21.12.2021		0	0,7	51,1	255,5	115374	w
12	reference	22.12.2021		0	0,8	58,4	292	176879	w
13	reference	23.12.2021		0	0,7	51,1	255,5	557253	w
14	reference	15.01.2022		0	0,6	43,8	219	2844707	o
H17	monoton	N/A	old parameters	0	1	73,4	338,2	1	